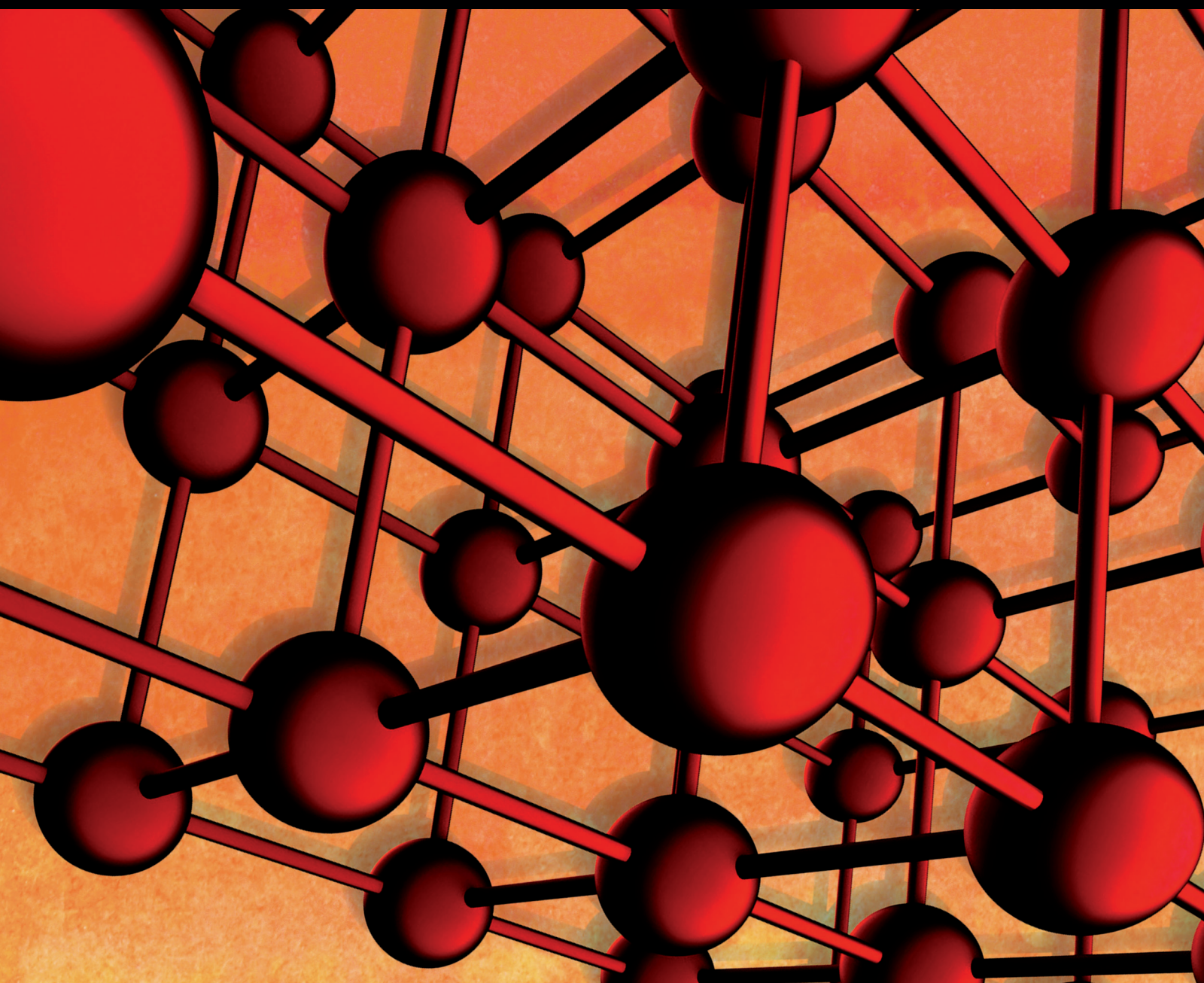


Advances in Materials Science and Engineering

Production, Characterization, and Applications of Porous Materials

Guest Editors: Nikolaos Michailidis, Alexander Tsouknidas, Louis-Philippe Lefebvre, Thomas Hipke, and Naoyuki Kanetake





Production, Characterization, and Applications of Porous Materials

Advances in Materials Science and Engineering

Production, Characterization, and Applications of Porous Materials

Guest Editors: Nikolaos Michailidis, Alexander Tsouknidas,
Louis-Philippe Lefebvre, Thomas Hipke,
and Naoyuki Kanetake



Copyright © 2014 Hindawi Publishing Corporation. All rights reserved.

This is a special issue published in “Advances in Materials Science and Engineering.” All articles are open access articles distributed under the Creative Commons Attribution License, which permits unrestricted use, distribution, and reproduction in any medium, provided the original work is properly cited.

Editorial Board

K. G. Anthymidis, Greece
Robert S. Averbach, USA
Amit Bandyopadhyay, USA
Zoe Barber, UK
Yucel Birol, Turkey
Susmita Bose, USA
Steve Bull, UK
Peter Chang, Canada
Daolun Chen, Canada
Manish U. Chhowalla, USA
S. Chinnappanadar, India
Martin Crimp, USA
Jie Dai, Singapore
Chapal K. Das, India
João P. Davim, Portugal
Seshu B. Desu, USA
Yong Ding, USA
Sergi Gallego, Spain
John W. Gillespie, USA
Hiroki Habazaki, Japan
Richard Hennig, USA
Dachamir Hotza, Brazil
Chun-Hway Hsueh, Taiwan
Shyh-Chin Huang, Taiwan
Rui Huang, USA
Wei Huang, China
Jacques Huot, Canada
William A. Jesser, USA
Jaehwan Kim, Korea

Sridhar Komarneni, USA
Prashant Kumta, USA
Jui-Yang Lai, Taiwan
Pavel Lejcek, Czech Republic
Markku Leskela, Finland
Bin Li, China
Hai Lin, China
Yuanhua Lin, China
Zhimin Liu, China
Tao Liu, China
Jun Liu, China
Ying Liu, USA
Meilin Liu, Georgia
Yuan Liu, China
Gang Liu, China
Maria A. Loi, The Netherlands
Hai Lu, China
Peter Majewski, Australia
Shuichi Miyazaki, Japan
Paul Munroe, Australia
Ali Nazari, Iran
Luigi Nicolais, Italy
Tsutomu Ohzuku, Japan
Xiaoqing Pan, USA
Ganapathiraman Ramanath, USA
Raju V. Ramanujan, Singapore
Manijeh Razeghi, USA
Mohd Sapuan Salit, Malaysia
Jainagesh A. Sekhar, USA

Jiangbo Sha, China
Liyuan Sheng, China
You Song, China
Aloysius Soon, Korea
Charles C. Sorrell, Australia
Steven L. Suib, USA
Sam-Shajing Sun, USA
Weihua Tang, China
Achim Trampert, Germany
Vladimir Tsukruk, USA
Krystyn Van Vliet, USA
Rui Vilar, Portugal
Min Wang, China
Jörg M. K. Wiezorek, USA
Wei Wu, USA
Gongnan Xie, China
Aiguo Xu, China
Jianqiao Ye, UK
Yadong Yin, USA
Ming-Xing Zhang, Australia
Jian Zhang, Singapore
Kai Zhang, China
Kai Zhang, China
Rui Zhang, China
Tao Zhang, China
Bin Zhang, China
Jun Zhang, China
Yufeng Zhang, China
Jing Zhang, China

Contents

Production, Characterization, and Applications of Porous Materials, Nikolaos Michailidis, Alexander Tsouknidas, Louis-Philippe Lefebvre, Thomas Hipke, and Naoyuki Kanetake
Volume 2014, Article ID 263129, 2 pages

Zeolite Y: Synthesis, Modification, and Properties—A Case Revisited, Wolfgang Lutz
Volume 2014, Article ID 724248, 20 pages

The Anisotropy of Replicated Aluminum Foams, Eugeny L. Furman, Arcady B. Finkelstein, and Maxim L. Cherny
Volume 2014, Article ID 230767, 6 pages

Geometric Models for Isotropic Random Porous Media: A Review, Helmut Hermann and Antje Elsner
Volume 2014, Article ID 562874, 16 pages

Mesostructural Design and Manufacturing of Open-Pore Metal Foams by Investment Casting, Alexander Martin Matz, Bettina Stefanie Mocker, Daniel Wyn Müller, Norbert Jost, and Gunther Eggeler
Volume 2014, Article ID 421729, 9 pages

The Role of Foaming Agent and Processing Route in Mechanical Performance of Fabricated Aluminum Foams, Alexandra Byakova, Iegor Kartuzov, Svyatoslav Gnyloskurenko, and Takashi Nakamura
Volume 2014, Article ID 607429, 9 pages

Free-Form Rapid Prototyped Porous PDMS Scaffolds Incorporating Growth Factors Promote Chondrogenesis, Andrés Díaz Lantada, Hernán Alarcón Iniesta, Beatriz Pareja Sánchez, and Josefa Predestinación García-Ruíz
Volume 2014, Article ID 612976, 10 pages

Antibacterial Characteristics of Lotus-Type Porous Copper, Jin-Soo Lee, Yun-Soo Lee, Mok-Soon Kim, Soong-Keun Hyun, Chang-Ho Kang, Jae-Seong So, and Eui-Han Yoon
Volume 2013, Article ID 608350, 4 pages

Editorial

Production, Characterization, and Applications of Porous Materials

Nikolaos Michailidis,¹ Alexander Tsouknidas,² Louis-Philippe Lefebvre,³ Thomas Hipke,⁴ and Naoyuki Kanetake⁵

¹ *Physical Metallurgy Laboratory, Mechanical Engineering Department, Aristotle University of Thessaloniki, P.O. Box 490, 54124 Thessaloniki, Greece*

² *Department of Mechanical Engineering, Frederick University, 1036 Nicosia, Cyprus*

³ *National Research Council Canada, 75 de Mortagne, Boucherville, QC, Canada H1Y 2V9*

⁴ *Department of Light Weight Design, Metal Foam Centre, Fraunhofer Institute for Machine Tools and Forming Technologies, 09126 Chemnitz, Germany*

⁵ *Department of Materials Science and Engineering, Graduate School of Engineering, Nagoya University, Furo-cho, Chikusa-ku, Nagoya 464-8603, Japan*

Correspondence should be addressed to Nikolaos Michailidis; nmichail@eng.auth.gr

Received 6 July 2014; Accepted 6 July 2014; Published 12 August 2014

Copyright © 2014 Nikolaos Michailidis et al. This is an open access article distributed under the Creative Commons Attribution License, which permits unrestricted use, distribution, and reproduction in any medium, provided the original work is properly cited.

1. Introduction

Lightening a structure through the use of holes is a rather ancient concept that naturally led to the development of the new porous structures we are seeing today. A pore within a solid, or cell, can be defined as a spatial confinement of air. The shape and size of the cell have significant influence on the response of the material to external stimuli. The ability to describe the behavior of these materials has enabled engineers to tailor the macromechanical properties of porous materials to specific requirements. This has considerably promoted the applicability of such structures, which are playing an increasingly important role in several high impact sectors (aerospace, automotive, medical devices, etc.). This can be attributed to their unique combination of properties such as high specific mechanical properties, permeability, specific surface area, and biomimetic properties. Recent advances in material synthesis have helped in adapting the properties of porous structures to specific applications. The technical challenge to comprehend and predict the response of these materials when subjected to load has attracted the interest of engineers and materials scientists. However, porous materials exhibit other characteristics of enormous practical importance and thus the capacity to systematically and effectively

describe their performance in a specific environment, is of great importance to multiple scientific fields.

The macromechanical response of a noncontinuous medium under load is nonetheless a multidisciplinary phenomenon of simultaneously occurring mechanical and physical processes. The continuous modifications of the structures during deformation add further complexity to predicting their elastic and plastic behavior.

Finite element techniques have helped to ease this and related modeling techniques are now considered as ubiquitous in describing the behavior of porous materials. Advanced mesh generating techniques combined with a recent increase in computational efficiency of processing software have facilitated the adaptation of such methodologies to stochastic geometries as ceramic and metallic foams [1].

2. Current Trends

Recent developments in the field of porous materials have helped the commercialization of new porous materials. Cost efficient production processes enabled their acceptance in several industrial sectors.

Open and closed cell structures with a stochastic macroporosity are currently produced with space holder based

techniques, gas expansion methods (through the addition of a decomposing foaming agent) or even chemical reaction techniques [2, 3]. These approaches do, however, allow the control of pore size and distribution, to an adequate extent.

Additive manufacturing techniques permit the integration of oriented patterns of pores in a controlled manner. Layer based fabrication techniques have gained tremendous importance in the production of a variety of materials with designed porosity (i.e., metallic, polymer, and composites). A significant limitation of most commercially available printing devices is, however, associated with high material and maintenance costs. Open source rapid prototyping has recently emerged as a cost efficient alternative and may help spreading the use of these technologies, even for composite materials [4].

Several techniques have also been introduced for the production of micro- and mesoporous media, such as carbonization methods, imprinting of nanopores in spin-on dielectric thin films, and hard template methods.

3. Emerging Applications

The continuing efforts to explore the interdisciplinary phenomena governing porous materials are dictated by a rapid growth of technology driven sectors such as medicine, pharmaceuticals, and energy, as recent breakthroughs in meso- and macroporous structures have fostered unprecedented opportunities for new applications [5, 6]. Materials with mesoporosities ranging of 2–50 nm have been used in drug delivery systems whereas macroporous bioactive ceramics loaded with stem cells and molecules are presently investigated to increase tissue regeneration in large osseous defects [5, 7]. Metallic-organic frameworks, employed as catalysts or energy conversion and storage devices, molecular sieves and markers, optics and photonics, inverse opals, and so forth, are also among the numerous novel applications of porous materials being developed.

4. Epilogue

Our sincere hope and wish is that the recent development presented in this issue will contribute to the development of this multidisciplinary discipline and provide tools to better understand the properties and characteristics of these materials.

Nikolaos Michailidis
Alexander Tsouknidas
Louis-Philippe Lefebvre
Thomas Hipke
Naoyuki Kanetake

References

- [1] N. Michailidis, E. Smyrniaios, G. Maliaris, F. Stergioudi, and A. Tsouknidas, “Mechanical response and FEM modeling of porous Al under static and dynamic loads,” *Advanced Engineering Materials*, vol. 16, pp. 289–294, 2013.
- [2] N. Michailidis and F. Stergioudi, “Establishment of process parameters for producing Al-foam by dissolution and powder sintering method,” *Materials and Design*, vol. 32, no. 3, pp. 1559–1564, 2011.
- [3] N. Kanetake and M. Kobashi, “Innovative processing of porous and cellular materials by chemical reaction,” *Scripta Materialia*, vol. 54, no. 4, pp. 521–525, 2006.
- [4] A. Tsouknidas, “Friction induced wear of rapid prototyping generated materials: a review,” *Advances in Tribology*, vol. 2011, Article ID 746270, 7 pages, 2011.
- [5] E. Baril, L. P. Lefebvre, and S. A. Hacking, “Direct visualization and quantification of bone growth into porous titanium implants using micro computed tomography,” *Journal of Materials Science: Materials in Medicine*, vol. 22, no. 5, pp. 1321–1332, 2011.
- [6] R. Neugebauer and T. Hipke, “Dynamisches Verhalten geschäumter bauteile,” *Materialwissenschaft und Werkstofftechnik*, vol. 31, no. 6, pp. 515–518, 2000.
- [7] N. Michailidis, F. Stergioudi, K. Viglaki, and M. Chatziniokolaidou, “Production of novel ceramic porous surfaces tailored for bone tissue engineering,” *CIRP Annals—Manufacturing Technology*, vol. 63, no. 1, pp. 557–560, 2014.

Review Article

Zeolite Y: Synthesis, Modification, and Properties—A Case Revisited

Wolfgang Lutz

Brandenburgische Technische Universität Cottbus, Volmerstraße 13, 12489 Berlin, Germany

Correspondence should be addressed to Wolfgang Lutz; lutz@btu-lc.fta-berlin.de

Received 9 October 2013; Revised 21 January 2014; Accepted 23 January 2014; Published 22 May 2014

Academic Editor: Louis-Philippe Lefebvre

Copyright © 2014 Wolfgang Lutz. This is an open access article distributed under the Creative Commons Attribution License, which permits unrestricted use, distribution, and reproduction in any medium, provided the original work is properly cited.

Y zeolites dealuminated by steaming were introduced as fluid-cracking catalysts in the year 1970. Extensive research has been done to develop suitable dealumination techniques, to investigate crystal structure, and to characterize catalytic behaviour. However, the origin of the secondary pore system formed in the zeolite structure during dealumination process remained completely obscure over a period of four decades. Open questions concerned also the existence of extraframework siliceous admixture in addition to extraframework aluminium species which can dramatically change the catalytic properties of these zeolites. This paper gives a review on the synthesis of DAY materials and provides some answers to several open questions.

1. Introduction

Commercial synthesis of Y zeolite was claimed by Breck in 1964 [1] after the first industrial manufacturing of A and X types by Milton [2, 3]. Zeolite NaY appears to be topologically analogous with the type X aluminosilicate framework. The cubic unit cell of all these aluminosilicates contains 192 (Si,Al) O_4 tetrahedrons. Breck suggested that the change of X to Y modification occurs at a silicon to aluminium ratio of 1.5 [4]. Zeolites with Si/Al values lower and higher than this critical point characterize X and Y composition, respectively. Because of the instability of Al-rich samples in acids or water at elevated temperatures [5], Rüscher et al. [6] proposed a new definition based on a typical chemical behaviour of the samples—the dealumination by steam treatment [7]. Above Si/Al ratio of 2.2, Y samples may be dealuminated in steam without collapse of its framework. The reason for that arises from long silicate chains with 132 remaining silicate units while 60 aluminate units can be removed.

The new X/Y definition explains the reason why only high-silica modifications of zeolite Y have been used as cracking catalysts [8, 9]. Since zeolite Y can be directly synthesized with maximal Si/Al values of about 3 [10], all catalytically relevant materials must be prepared by postsynthetic removal of framework aluminium. Zhdanov et al. [11] provided an

overview about different techniques of zeolite dealumination such as acid extraction [12], isomorphous Al/Si substitution [13], and thermochemical treatment of NH_4Y [7]. Heating of NH_4Y in dry or wet air brings different dealumination effects and structural features to dealuminated Y samples (DAY) [14]. In each case, framework aluminium will be transformed thereby into extraframework aluminous species (EFAL) [15].

Ambs and Flank [16] explained the thermal stability of DAY over 1273 K as a result of the removal of sodium ions which destabilize the framework due to their mineralizing effect. Peri [17] gave preference to the formation of novel Si–O–Si bonds as a result of dehydroxylation of intermediately formed hydroxyl nests. Kerr et al. [18] explained rising stability of DAY by effect of healing of the Al defects with migrating H_4SiO_4 molecules.

Increasing thermal stability of DAY was one of the reasons why the thermochemical process has been commercially established in a high extent. After discovery of structural fundamentals of steamed zeolites, researchers put more attention on their catalytic behaviors. Thereby, the formation of a secondary pore system in DAY has been found. According to [19], this process was assumed to enhance the molecular transport of starting materials and final products during catalytic conversion. But, in spite of the framework repairing, a significant decrease of the sorption capacity

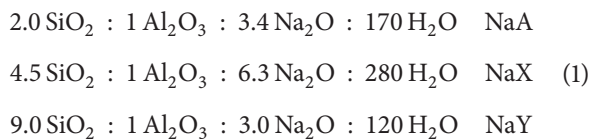
was observed [7]. The nature of this phenomenon is still unclear and problems of mesopores formation and types of mesopores, as well as partial amorphization of the zeolite framework remain open.

Since a direct relationship between the structure of NaY and the specific dealumination behavior of NH_4Y undoubtedly exists, revisiting the problems of synthesis, ion-exchange, and dealumination behaviors of zeolite Y seems to be advisable.

2. Results and Discussion

2.1. Synthesis of Zeolite NaY. Fundamentals of the synthesis of aluminum-rich zeolites of A, X, and Y types were reported by Kerr [20, 21], Breck and Flanigan [22], Zhdanov [23], and McNicol [24]. These and several other authors discussed mainly the crystallization process of zeolites from their primary aluminosilicate gels. Using Molybdate method [25], Fahlke and colleagues [26, 27] investigated in details the mechanism of gel formation and following rearrangement. This method determines the length of silicate chains between aluminate units in dependence on gel maturation. Indeed, prolonged silicate units define the process of gel aging. For measurement, the $\equiv\text{Al}-\text{O}-\text{SiO}_{(n)}-\text{Al}\equiv$ with $n = 1-\infty$ zeolite framework is hydrolyzed in mineral acid and added to molybdic acid. The degradation rate (the measure of the length of silicate chains) is optically followed by formation of the yellowish silica Molybdate complex. This technique characterizes perfectly the Al-rich A and X zeolites, but it fails in the case of Y crystals because the infinite long silicate chains of latters are practically insoluble in acid.

Properties of DAY samples—crystallinity, silicon to aluminium ratio, secondary pore volume, and extraframework species—depend directly on the state of the parent NaY crystals and even on the starting gel. Typical composition of synthesis batches of aluminosilicate zeolites are



with final Si/Al ratios of 1, 1–1.2, and 2.2–3.0, respectively [22]. Basic materials are aqueous solutions of sodium aluminate and sodium silicate for NaA and NaX, silica gel or silica sol for NaY, and, as expected, sodium hydroxide and water. The reaction composition diagram according to Breck [4] or Kostinko [28] shown in Figure 1 demonstrates that the fields of gel compositions from those A, X, or Y zeolites are formed.

As can be seen from Figure 1, the variation of gel composition of X and Y zeolites is significantly smaller than that of zeolite A.

By mixing of raw materials, aluminosilicate gels occur in all zeolite synthesis batches. For example, when pure solutions of aluminate and silicate are mixed, spontaneously silicon-rich hydrogels precipitate. Some of the monomeric aluminate ions are linked to the oligomeric silica molecules. The residual aluminate ions remain at first in the solution. But the gel reorganizes its structure by dissolution and renewed

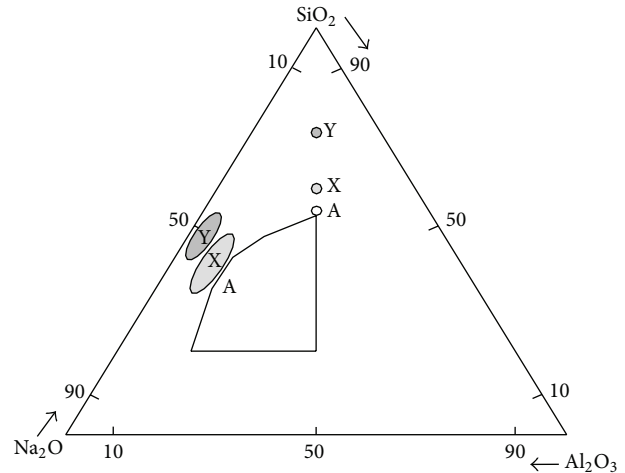


FIGURE 1: Reaction composition diagram of aluminosilicate zeolites A, X, and Y (fields-possible gel composition; points-final zeolite composition) [4].

precipitation up to the equilibrium state. Over an aging period of ten to twenty hours, the gel consumes more and more aluminate in such a way that finally the solids contain silicon and aluminium in equivalent amounts in zeolites A and X batches. The three-dimensional gel structure is stable at ambient temperature in its mother liquid because all alkaline soluble $\equiv\text{Si}-\text{O}-\text{Si}\equiv$ bonds were changed already into chemically stable $\equiv\text{Si}-\text{O}-(\text{Al}^{(-)})\equiv$ bonds. The negative charges of the fourfold coordinated Al atoms protect the gel against further attacks of the likewise negatively charged hydroxyl ions. On the other hand, the negative charges promote the attack of protons for spontaneous degradation of the framework as in the case of Molybdate measurements.

Wieker and Fahlke [27] detected 10% of monomeric $\equiv(\text{Al}^{(-)})-\text{O}-\text{Si}-\text{O}-(\text{Al}^{(-)})\equiv$ silicate building units, in addition to polymeric silicate, in NaY synthesis batches. The NaY gel composition differs thus from that of A and X. Due to these monomeric species, the crystallization of NaY starts with fragments of NaX composition (Si/Al ratio of about 1) at 363–373 K. The crystallization is favored if the batch is seeded by NaX nanocrystals, exactly by the way exploited in industrial zeolite manufacturing. Actually so-called seed-solutions which contains silicate ions in the form of oligomeric chains (length of 10–30 silicon atoms) terminated by aluminate units are used in order to prevent, as much as possible, the formation of Al-rich areas inside the NaY crystals.

With the increasing of time, the crystallization turns gradually into the actual NaY zeolite composition with a Si/Al ratio over 2.2. Then, due to the overproportional consumption of aluminate at the beginning of the process, the crystallization drops off owing to the total consume of aluminate ions being primary building units in the faujasite structure. This is the reason why the crystal surface becomes finally rich in silicon and no secondary crystal growth above $3 \mu\text{m}$ is observed [29, 30]. Frequently, the NaY zeolites are crystallized in polycrystalline particles with smaller actual size [31].

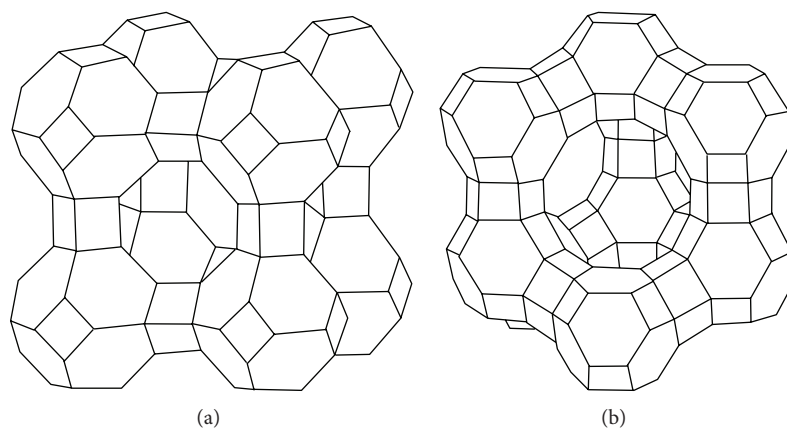


FIGURE 2: Zeolite A (a) and faujasite-type zeolites X and Y (b) formed by sodalite cages.

The synthesis of large faujasite type crystals with diameters $>100\ \mu\text{m}$ was reported by Ferchiche et al. [32, 33] and Berger et al. [29] only for samples with Si/Al ratios below 1.8. It seems very likely that such samples consist of the mixture of both X and Y types [6].

The Si to Al gradients in NaY starting from 1 inside the nuclei and increasing to ∞ at the surface of the zeolite crystals are responsible for several further specific phenomena observed in steamed DAY zeolites. The NaY crystals with Si/Al ratios over 2.2 are unfortunately too small for a characterization of their gradient by physicochemical methods such as ESCA or EDX. Additionally, they tend to collapse during measurements. Therefore, a complex characterization of DAY samples including tests of hydrothermal stability, state of crystallinity, characterization of extraframework species, and pore structure is necessary to describe the actual state of NaY and consecutive products.

2.2. Sodium/Ammonium Ion Exchange of Zeolite NaY. The unit cell of zeolite NaA contains 24 atoms and that of the faujasite-type zeolites NaX and NaY contains 192 SiO_4 and AlO_4 tetrahedrons [34]. They form sodalite cages which are linked to oxygen double 4 rings and 6 rings in NaA, NaX, and NaY, respectively, as seen from Figure 2. In NaA and low-silica NaX frameworks with Si/Al = 1, the SiO_4 and AlO_4 tetrahedrons are arranged in rigorous alternation according to the Loewenstein rule [35].

Cavities with pore diameters of 1.14 nm in NaA and 1.3 nm in NaX, NaY arise. The diameters of pore entrance are equal to 0.42 nm and 0.74 nm, respectively [4].

Due to the negatively charged $\text{AlO}_4^{(-)}$ tetrahedrons, zeolites contain $\text{Na}^{(+)}$ ions in different amounts in their synthesis form –12 in NaA, 96–88 in NaX, 56–53 in NaY (values of X and Y based on the definition of Rüscher et al. in [6]). Different cations may be exchanged for sodium ions, totally or to a high degree, to adjust the entrance pore diameter and specific sorption behaviour of zeolites. Barrer and colleagues published fundamental aspects about this method of zeolite modification, for example, in [36, 37].

Because zeolite NaY is used preferentially in dealuminated state for catalytic processes, the introduction of ammonium ions into this framework is of specific interest. Ammonium ions are decomposed by heating in H^+ and outgoing NH_3 gases thus forming HY modification which is active in the framework dealumination by steaming.

At the laboratory scale, the ammonium ions can be exchanged for sodium ions in 0.1 M solution of ammonium nitrate or sulphate at liquid/solid ratio higher than 10. For an effective and careful exchange, the procedure should be repeated. In this way, 80% of sodium ions are removed from the framework of zeolite Y. Thus, one-fifth of the framework remains inactive in dealumination, for example, by steaming as it will be seen below. The use of a higher concentrated salt solution or/and treatment of the zeolite at 353 K was not successful [38]. But there is a possibility to increase the active framework part if a stepwise way is used: firstly the partially ammonium exchanged sample is heated at 523–543 K then the ion exchange procedure is repeated once more. Intermediately produced protons displace the residual sodium ions from their position inside the sodalite cages and double-six rings which are removed in the second ammonium exchange from the large cavities. Partial dealumination of the framework already takes place at each treatment step.

2.3. Dealumination. Dealumination is a method of chemical and structural modification of zeolites. But not each synthetic zeolite framework preserves structural arrangement and stability after removing some Al atoms. Thus, NaA and NaX zeolites are completely collapsed after any dealumination procedure. NaY zeolite with Si/Al < 2.2 also loses, at least partially, its crystallinity [39]. But only with this treatment, Y aluminosilicates with definite Si to Al ratios that guarantee their specific properties such as thermal stability, hydrophobicity, or catalytic activity can be directly prepared.

The simplest dealumination method consists of the treatment of samples in inorganic or organic acid [12] where decationation takes place. Under action of the introduced protons, $\equiv\text{Si}-\text{O}-(\text{Al}^{(-)})\equiv$ bonds became hydrolyzed and changed firstly into more stable $\equiv\text{Si}-\text{O}-\text{H}$ units plus $\text{H}-\text{O}-\text{Al}\equiv$ splitted

structure. At the second step, all the other bindings with Al ions are broken off. Utilizing the natural clinoptilolite, firstly, Barrer and Makki [40] were successful in the treatment of the zeolite with 1 M hydrochloric acid at 373 K. The aluminium content decreased down to 40% without a significant loss of crystallinity of samples. Aluminium atoms removed from the framework were found as EFAI species in the solution. The disadvantage of this method for zeolite NaY lies in remaining structural defects involving formation of hydroxyl groups inside the silicon framework [41].

A more sensitive extraction process includes a treatment of the zeolite with complex agent of ethylene-diamine-tetra-acetic acid (EDTA). By use of this method Kerr [12] removed the half of the framework aluminium atoms in NaY zeolite without a greater amorphization of the crystals but with a high density of structural defects. One can get more intact structures if zeolite NaY is treated in a vapor of silicon-tetra-chloride as it was shown by Beyer and coworkers [13, 42, 43]. In the resulting structure, Al atoms are replaced by silicon atoms at elevated temperature. But rigid control over this exothermic process and technological demand on the resistance against the aggressive medium appears to be too complex so that industrial production was restricted only to the semi-industrial scale. Therefore, the calcination of NH_4Y zeolites in steam [7] has been established worldwide as technical dealumination process.

2.3.1. Thermochemical Treatment of NH_4NaY in Steam. Generally, dealumination of NH_4NaY in steam has not been changed since the introduction of this procedure by McDaniel and Maher in 1971 [15]. Samples are treated in an open furnace or rotary kiln through which steam of 1 bar water pressure is going. Steam is generated by evaporation of liquid water with one bar of water pressure or saturation of gas with water vapor of lower partial pressure. The actual concentration of water molecules inside the oven reaction zone depends on heating and is reduced with increasing temperature of sample treatment. The extent of dealumination is limited by the degree of ammonium exchange of the starting material and depends on the temperature and partial pressure of steam [44, 45].

Salman and colleagues [46] have investigated the dealumination of zeolite $(\text{NH}_4)_{39}(\text{Na})_{10}[(\text{AlO}_2)_{49}(\text{SiO}_2)_{143}]$ with a Si/Al ratio of 2.9 over a wide field of variable parameters. Figure 3 shows increasing removal of framework Al with rising the temperature and period of treatment.

Small and slightly higher dealumination with Si/Al values of 3.2 and 3.5 was found at 573 K and 673 K, respectively. The evolution of Si/Al at 773 K and 873 K indicates a typical saturation behaviour towards values of 4.4 and 5.4. Saturation effects have also been reported earlier by Wang et al. [39], Engelhardt et al. [44], and Lohse et al. [47]. Due to a limitation of sodium/ammonium exchange in the used one-step strategy, 20% of the $\text{Na}^+/\text{AlO}_4^-$ charge complexes remained stable under steam. The equilibrium Si/Al ratios obtained in [46] correspond to 36% (773 K), 49% (873 K), and 64% (973 K) of the total content of Al atoms removed from the framework. Further removal could be increased by a renewed ammonium exchange followed by a second steaming

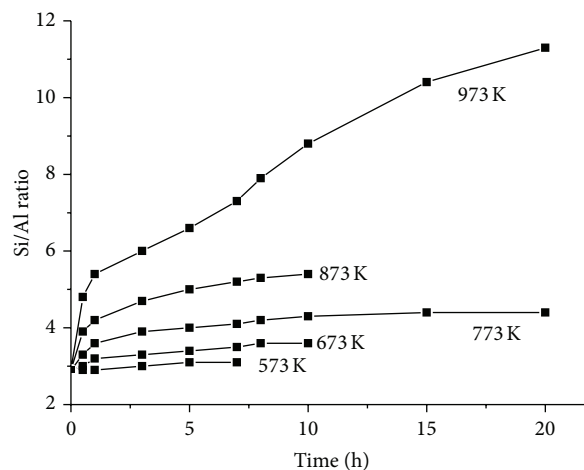


FIGURE 3: Si/Al ratio of DAY zeolites in dependence on steaming temperature and time [46].

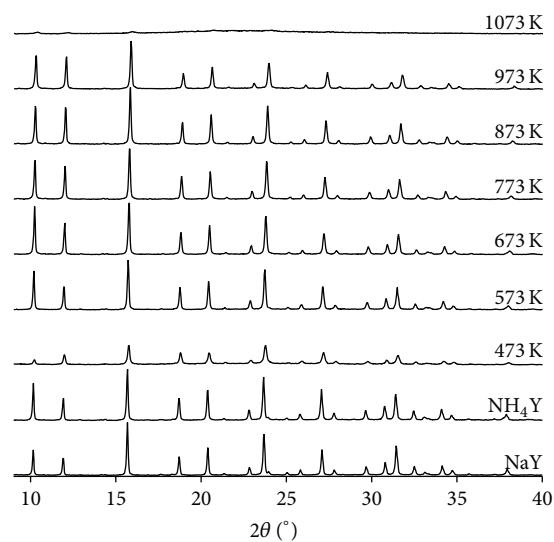


FIGURE 4: Selected XRD patterns of DAY zeolites steamed 3 hours in dependence on temperature [46].

process. Following this two-step strategy, the Si/Al ratio of DAY steamed at 873 K for 5 hours changed from 5.4 to 10.3, with a twofold increase of the dealumination effect without significant sample amorphization [38].

Significantly higher values of Si/Al ratio (up to 11) have been obtained directly for steaming at 973 K. However, this result was accompanied by a partial or strong amorphization of the final product. The sample became completely amorphous at 1073 K because of a thermal collapse at the beginning of steaming. At the lowest temperature investigated (473 K), drastic framework damage has occurred, too. In this case, a sour hydrolysis of the framework owing to the high concentration of water molecules in the reaction zone took place.

X-ray diffraction (XRD) patterns in Figure 4 indicate a moderate decrease in signal intensity for NH_4NaY and DAY

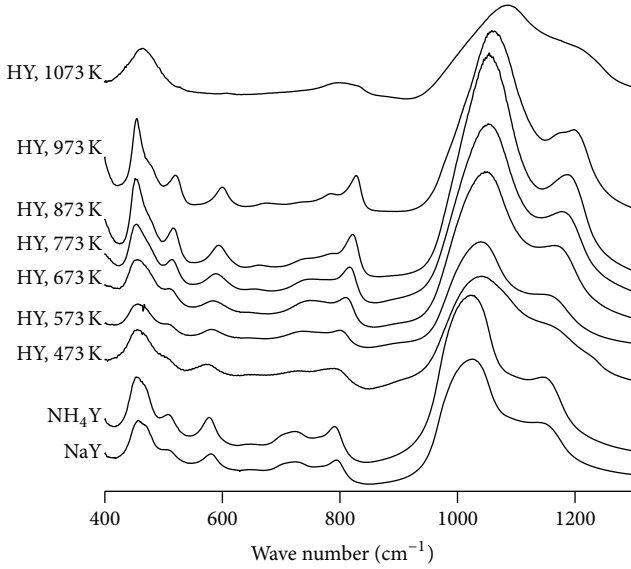


FIGURE 5: IR spectra of parent NaY zeolite and DAY samples steamed for 3 hours in dependence of temperature.

samples. This observation will be discussed below, along with the results on the formation of extraframework species.

Removal of Al atoms results in the shrinking of the total zeolite framework because of the different –Al–O– and –Si–O– bond lengths of 191 pm and 169 pm [48], respectively. The lattice constant a_0 decreases from 2.463 nm in NaY to 2.438 nm in DAY treated at 973 K for 1h. This sample shows the highest dealumination state, without a significant structural amorphization.

IR spectra of DAY samples obtained by Salman et al. [46] are given in Figure 5 and support the data of XRD measurements. The framework sensitive double-ring vibration band w_{DR} [49] shifts from 574 cm^{-1} to 610 cm^{-1} with increasing steaming temperature up to 973 K. The signal completely disappeared in the sample dealuminated at 1073 K.

Apart from w_{DR} signal, systematic changes in the shape of spectra, particularly bending, symmetrical and asymmetrical stretching vibration of the TO_4 building units at $450\text{--}550\text{ cm}^{-1}$, $700\text{--}900\text{ cm}^{-1}$, and $900\text{--}1200\text{ cm}^{-1}$, have been additionally observed. Optimal conditions of steaming appear to be at 873 K as evident from the shape and intensities of characteristic peaks in the dealuminated framework seen in Figure 5. The framework became more regular in respect to the former Si/Al gradient resulting from NaY synthesis.

At lower temperature, the shape of peaks becomes broader indicating a higher nonuniform distribution of the Si/Al ratio in the framework and a relative stronger contribution of the extraframework species formed. But, as we will see below, lower steaming temperatures lead to a reduced mesopore formation.

One can suggest that all spectra in Figure 5 are superimposed by extraframework species of aluminosilicate and silica gel [50] formed by some corrosion of the framework. The aluminosilicate may be extracted together with the extraframework aluminium by acid treatment [51]. It is

known that highly dealuminated and acid leached DAY, frequently called US-EX (ultrastable extracted zeolite Y), shows very sharp vibration bands because of homogenisation of the pure SiO_2 framework [52].

In samples treated at 473 K, w_{DR} signal does not shift from its characteristic place. In this case, due to the low thermal activation no dealumination occurs inside the framework but the dissolution of the zeolite takes place.

2.3.2. Determination of the Si/Al Ratio of DAY Samples. The tuning of framework properties of DAY zeolites requires an exact determination of the Si/Al ratio. Dealumination effect can be proved by chemical analysis of the acid solution and washing water in the samples prepared through acid leaching [12] and Al/Si substitution [13], respectively. However, such approach requires certainty that all extraframework aluminium is completely washed out in the samples. Therefore, investigation of the solid state by physicochemical methods like XRD, IR, and NMR seems to be the better way. These methods are even indispensable for characterization of steamed DAY samples because these zeolites still contain the whole amount of EFAl and chemical analysis data appear as contradictory.

Breck [4] has presented the relationship between the unit cell constant, a_0 , and Al atom density per unit cell for hydrated NaX and NaY zeolites on basis of 37 synthesized samples. Rüscher and colleagues [53] extended this mode upon series of DAY samples prepared by steaming as well as Al/Si substitution. They additionally proposed a thorough study of evolution of the IR double-ring vibration w_{DR} for determination of Si/Al ratios inside the zeolite framework and compared these calculation methods [50] with empirical equations of Fichtner-Schmittler et al. [52] using the infrared asymmetrical TOT valence vibration ($T = \text{Si, Al}$) and ^{29}Si MAS NMR data obtained by Engelhardt and Michel [54].

XRD_{Rüscher}

$$x = 5.348 a_0 - 12.898 \quad (2)$$

(with $\text{Si/Al} = (1 - x)/x$ and $x = \text{Al molar fraction}$ by use of the cell parameter a_0).

IR_{Rüscher}

$$x = 3.857 - 0.00619 w_{DR} \text{ (cm}^{-1}\text{)} \quad (3)$$

(with $\text{Si/Al} = (1 - x)/x$ and $x = \text{Al molar fraction}$ by use of w_{DR}).

IR_{Fichtner}

$$x = 4.766 - 0.00439 w_{TOT} \text{ (cm}^{-1}\text{)} \quad (4)$$

(with $\text{Si/Al} = (1 - x)/x$ and $x = \text{Al molar fraction}$ by use of w_{TOT}).

NMR_{Engelhardt}

$$\frac{\text{Si}}{\text{Al}} = \frac{\sum_n I_n}{(I_4 + 0.75 I_3 + 0.5 I_2 + 0.25 I_1)} \quad (5)$$

($I_n = \text{intensity of } Q^4/n\text{Al signals in } ^{29}\text{Si MAS NMR spectra, } n = 0\text{--}4, \text{ without consideration of the signals of the nonzeolitic admixtures}$).

TABLE 1: Si/Al values of zeolites NaY, HY, and DAY dealuminated for 5 h in steam.

Sample	Temperature K	Si/Al ratio			
		a_0 (2)	w_{DR} (3)	w_{TOT} (4)	NMR (5)
NaY	—	2.8	2.8	2.8	2.9
HY	543	2.8	2.9	2.8	2.8
DAY	773	3.8	4.0	7.9	8.2
DAY	873	4.4	5.0	8.9	8.7
DAY	973	5.2	6.7	10.8	11.8

In analogy to the results of Breck [4], Fichtner and coworker [52] have shown the correlation between unit cell parameters, skeletal stretching vibrations, and molar fraction of aluminium ($x = (1 + \text{Si}/\text{Al})^{-1}$) for a series of X and Y zeolites and found an ideal solid solution behaviour for these materials. The lattice constant a_0 as well as the infrared modes w_{TOT} and w_{DR} vary linearly on molar aluminium fraction which provides a rather easy method for calculating the Si/Al ratio of DAY samples independently on their synthetic type. However, differences in the level of Si/Al values have been reported in dependence on applied relations of (2) to (5). Significantly higher Si/Al values seen in Table 1 were calculated according to w_{TOT} and the NMR [50, 55].

The Si/Al ratios obtained with XRD data should characterize the actual state of the framework. These values were assumed to be not affected by extraframework species in the samples. Within each series of steaming temperature, the infrared mode w_{DR} closely coincides with the a_0 value because the double-ring vibration that characterizes only the pure faujasite framework [52]. In contrast, higher values have been calculated using NMR as well as w_{TOT} data. Results from both methods seemed to be influenced by admixtures of DAY samples. To clarify this phenomenon, a detailed phase analysis of framework and extraframework products in DAY specimens should be performed.

2.3.3. Extraframework Species in Steamed Y Zeolites. First observation of extraframework aluminium was published for natural zeolites after their acid treatment [40, 56]. Dealuminated samples obtained thereby [12] or by Al/Si substitution in SiCl_4 vapor [13] are usually free of EFAl if samples have been intensively washed out. Residues may be analyzed by ^{27}Al MAS NMR measurements [54] since the signal of Al atoms tetrahedrally coordinated in the zeolite framework and the signal characteristics of $\text{Al}^{(3+)}$ cations and AlCl_3 salt differ from each other by their spectral positions. The chemical shift of the former is situated at 60 ppm, whereas that of the latter lies at about 0 ppm. Extraframework silicon (EFSi) which can be detected by ^{29}Si MAS NMR measurements appears only in the case of partial amorphization of samples after their chemical treatment.

More complicated situation appears during calcination and steaming of NH_4NaY zeolites since all EFAl remains in the solid state [57, 58]. Baran et al. [59] considered that tetrahedrally coordinated Al is not transformed into exchangeable $\text{Al}^{(3+)}$ cations. Breck and Skeels [60, 61] suggested the formation of precipitated $\text{Al}(\text{OH})_3$ which can be

extracted by leaching with solutions of sodium chloride or potassium fluoride. The remaining defects (hydroxyl nests) of the zeolite framework can be identified by measurement of the infrared stretching vibration of isolated $\equiv\text{Si}-\text{OH}$ hydroxyl groups at 3745 cm^{-1} [11].

Different studies on EFAl have reported their possible location on the surface of crystal and/or mesopores [62, 63], revealed their role in the catalytic behavior [64] and, in particular, analyzed their nature by means of ^{27}Al MAS NMR spectroscopic measurements [65]. EFAl has been characterized as closely related to aluminium-oxo-hydroxo cations of polymeric arrangement described first by Bertram et al. [51] with the help of Ferron method [66]. Their chemical behavior in organic and mineral acids was intensively investigated by Scherzer [67]. An increase of the catalytic selectivity of DAY after extraction of the extraframework aluminium has been reported by Rhodes and Rudham [68]. Disadvantages after treatment in acid consist in the risk of further dealumination of the zeolite with remaining $\text{Al}^{(3+)}$ cations which could act as Lewis active sites in catalysis [69].

In some papers, EFAl has been described as not isolated but incorporated with EFSi and called therefore as silica-alumina species [70–72]. Strong interaction between both types of extraframework species was quantitatively analyzed with X-ray photoelectron spectroscopy [73]. Using specific Molybdate measurements [74], the silica-alumina was later characterized in samples of low-temperature steaming as Al aluminosilicate [75]. Therefore, Siantar et al. [76] and Lutz et al. [77] have performed detailed analysis of EFSi species. The dealumination behavior of NH_4NaY samples in the steam was demonstrated using two commercial and three laboratory NaY zeolite samples. Figures 6 and 7 show ^{27}Al and ^{29}Si MAS NMR spectra of initial and dealuminated zeolites.

Independent of the origin of zeolite samples, extraframework species appeared to be of the same type. The aluminium spectra in Figure 6 show a signal for tetrahedrally coordinated framework Al at 60 ppm [50] (NaY). After dealumination, additional two broader signals for extraframework species near 0 ppm and 30 ppm have been ascribed to octahedrally and pentahedrally coordinated Al, respectively. The signal at 0 ppm characterizes the polymeric oxo-hydroxo-aluminium cations [51] whereas the broad shoulder centered at 30 ppm is assigned to the distorted extraframework octahedra and/or aluminium tetrahedra of the framework [78, 79].

After deconvolution (II), the ^{29}Si MAS NMR spectra of NaY samples (I) in Figure 7 show the five signals typical for the faujasite framework with Si(nAl) building units ($n = 0-4$)

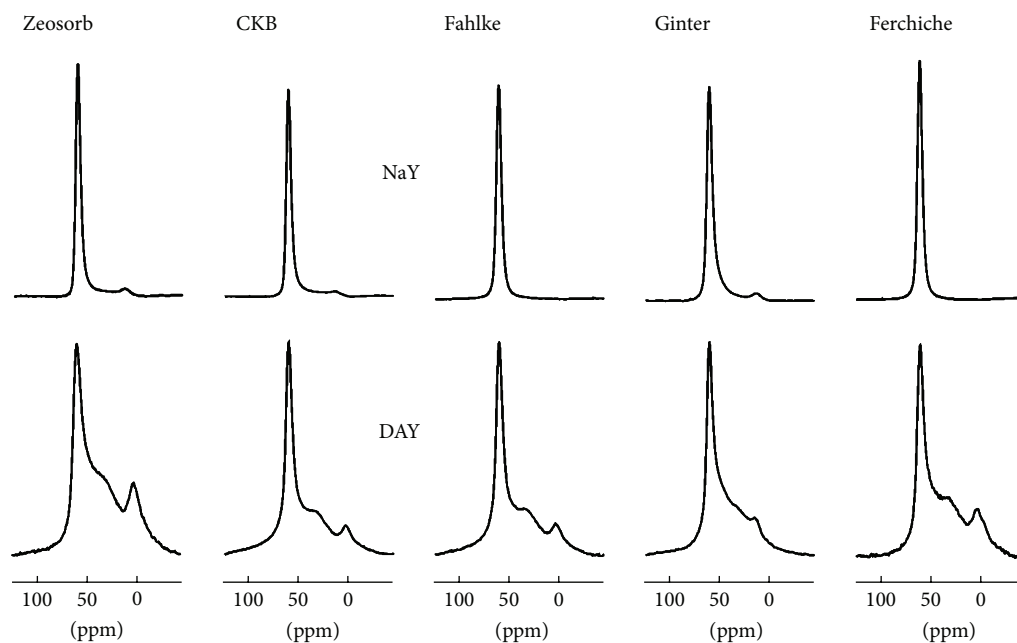


FIGURE 6: ^{27}Al MAS NMR spectra of commercially and laboratory synthesized zeolites before (NaY) and after dealumination for 7 hours at 873 K (DAY) (recipes of laboratory synthesized samples according to Fahlke et al. [26], Ginter et al. [80], and Ferchiche et al. [33]) [50].

at chemical shifts between -84 ppm and -108 ppm [77]. Simulation of the ^{29}Si MAS NMR spectra was performed by the use of a set of single lines with Gaussian line shape. This calculation reveals the lack of siliceous extraframework species (III) in the spectra of parent zeolites. But steaming results in a drastic change in shape and intensity of the NMR signals (I). All peak positions are shifted to higher ppm values. The decrease of the Si(4-2Al) and increase of the Si(1-0Al) structure units confirm the removal of framework aluminium. The significant shoulders between -80 and -90 as well as 112 ppm indicate an internal change of the framework structure and the presence of siliceous extraframework species (III). Contributions of aluminosilicate and silica gel are marked with the symbols *a* and *s*. In earlier investigations, these additional signals have been attributed to in-homogeneously dealuminated high-alumina and high-silica regions inside a disturbed zeolite framework [81, 82].

Content of extraframework species in steamed DAY samples [77] amounted to 0.6–4.9% for the aluminosilicate (*a*) and 4.3–14.7% for silica gel (*s*). It has been shown [83, 84] that the intensity of the peaks assigned to *a* and *s* at low-temperature steaming could be reduced by successive chemical dissolution in hydrochloric acid and solution of potassium hydroxide. Acid treatment caused the decomposition of the Al aluminosilicate with formation of silica gel. Alkaline treatment revealed a light loss of the silica gel admixture. In high-temperature samples, for example, at 873 K, the Al aluminosilicate decomposes into silica gel and clay. In such a case not the aluminosilicate *a* but the silica gel *s* is determined in a higher portion.

The occurrence of extraframework silica-gel *s* is the reason why Si/Al ratios calculated in DAY samples with w_{TOT}

mode (4) and NMR data (5) (see *italics* in Table 1) appear to be principally too high. Both IR and NMR signals are strongly superimposed by contributions of those characteristic of Si(0Al) and Si(1Al) species [85–87].

The strong deviation of Si/Al ratios determined with asymmetrical TOT infrared vibration band results from the great difference between the wave numbers of the zeolite and the silica gel. Wave numbers between 1080 and 1120 cm^{-1} have been observed for silica gels in dependence on their framework state [88]. The higher the portion of Q^4 building Si(OSi) $_4$ units, the higher the energy for the activation of their framework. For “pure” DAY samples, w_{TOT} values from 1024 to 1040 cm^{-1} should be measured. But, owing to the superposition of the nonresolved signals of both zeolite and silica gel, the actually measured values of DAY vary between 1047 and 1061 cm^{-1} [87].

The Si/Al ratios calculated with ^{29}Si MAS NMR are too high since the $\text{Q}^3(\text{Si}(\text{OSi})_3\text{OH})$ and $\text{Q}^2(\text{Si}(\text{OSi})_2(\text{OH})_2)$ signals of the extraframework silica gel superimpose with those assigned to Si(0Al) and Si(1Al) in the zeolite [85, 87]. In order to get real values, deconvolution of the spectra becomes the essential step of the zeolite analysis with NMR technique [77]. Therefore, more realistic Si/Al ratios should be obtained using the XRD lattice constant a_0 or the infrared w_{DR} mode according to (2) and (3), respectively.

2.3.4. Origin of Siliceous Extraframework Species. Zeolite NaY is stable in dry or wet air up to 923 K. After this temperature, the crystalline framework transforms into the amorphous state. Clay (Al_2O_3) and silica (SiO_2) are formed. Then, with the rising temperature, carnegiite and nepheline occur above 1123 K [4, 10]. In water or steam of autogenous

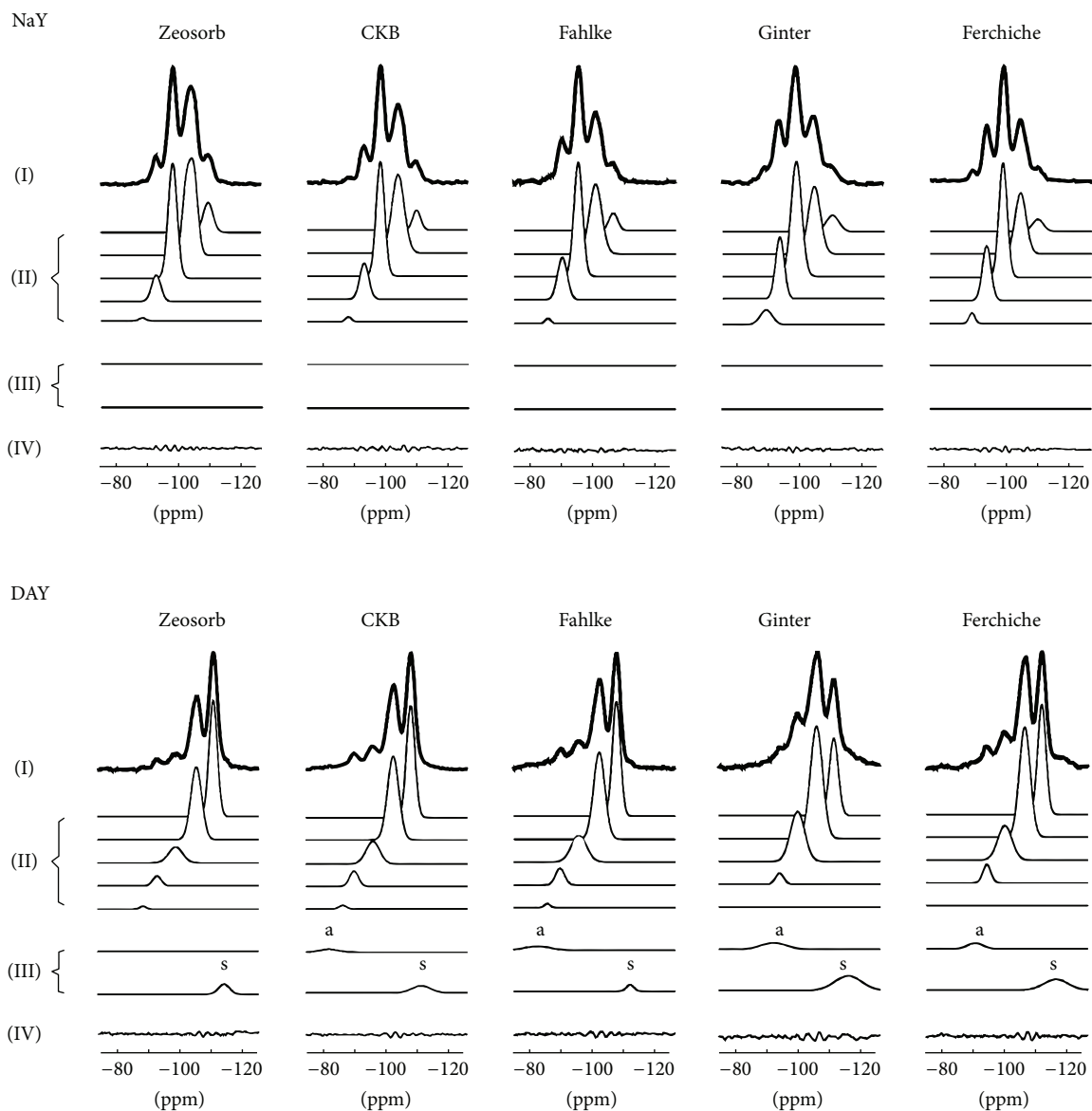


FIGURE 7: ^{29}Si MAS NMR spectra of commercially and laboratory synthesized zeolites before (NaY) and after dealumination for 7 hours at 873 K (DAY) [50].

pressure, NaY is stable up to 513 K [83]. It will be decomposed into an amorphous phase followed by transformation into hydroxysodalite or zeolite P [89, 90]. The containing sodium ions act as mineralizer. Buhl et al. [91] demonstrated their influence on the hydrothermal stability of faujasite type zeolites 13X (Si/Al = 1.2) and LSX (Si/Al = 1.0).

The proton modification of zeolite Y is of interest concerning the application of faujasites as DAY catalyst. According to Rüscher et al. [6] zeolite HY (Si/Al > 2.2) becomes dealuminated above 573 K under the formation of extraframework species. Infinite $\equiv\text{Si}-\text{O}-\text{Si}\equiv$ chains inside the framework prevent the zeolite decomposition and only a small part of the structure is transformed into aluminium hydroxide/-oxide, aluminium aluminosilicate, and silica gel. But in the case of lower Si/Al ratios and finite $\equiv\text{Si}-\text{O}-\text{Si}\equiv$

chains, the structure is hydrolyzed partially or completely. In this sequence, zeolite HX with Si/Al = 1.0–1.2 is particularly instable. In contrary, silicon rich faujasites with Si/Al over 100 manufactured by Al/Si substitution [13] or steaming and acid leaching [92] are instable during steam treatment [93, 94].

Two chemical processes run simultaneously in the same crystal of Y zeolite since the Al–Si gradients between aluminium-rich nuclei and silicon-rich surface of the zeolite appear in this material [89, 95], independent of the origin of NaY or steaming conditions. Consequently, the center of the crystal is transformed into X-ray amorphous aluminosilicate and then, with rising temperature, to clay and silica while the pure silica gel tends to form on the surface.

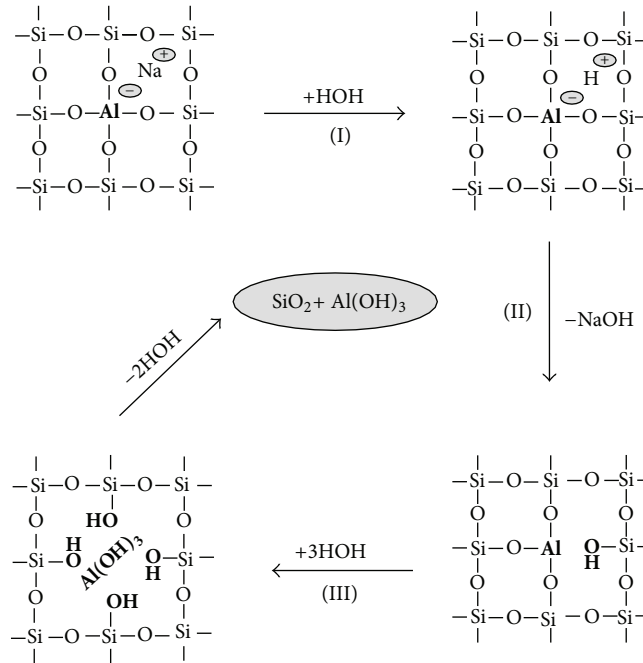
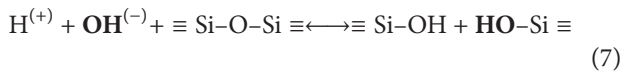
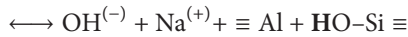
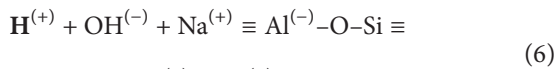


FIGURE 8: Stepwise decomposition of a low-silica zeolite framework by water [96].

Water molecules attack the zeolite framework according to the chemical reactions



with the rising temperatures. Thereby, the protons of the water molecules attack the $\equiv\text{Si-O-(Al}^{(-)})\equiv$ bonds over the whole framework whereas the hydroxide ions attack especially the terminal $\equiv\text{Si-OH}$ groups of the surface. Figures 8 and 9 give a schematic impression of both processes [96] where water acts like a catalyst [74].

In addition to the steaming procedure, a treatment in liquid water is helpful for the understanding of the hydrothermal chemistry of faujasite type zeolites. Dimitrijevic et al. [97] investigated the behavior of NaY and HY with Si/Al 2.7 in water of autogenous pressure between 403 K and 473 K. Figure 10 shows the sorption capacity of both samples after the hydrothermal process. The uptake of water in NaY remains unchanged, but that of HY decreases significantly above 423 K. The proton form is drastically damaged under treatment. The reason for this different behavior consists in the alkaline reaction of NaY in aqueous medium suppressing thus the attack of protons formed by water dissociation.

In addition to extraframework silica and alumina, traces of kaolinite occurred. The formation of a new crystalline phase below 473 K was detected for the first time. It is due to the incomplete sodium/ammonium ion exchange of the progenitor of the HNaY modification which was obtained by careful heating at 523 K.

Surprisingly, the silicon-rich DAY samples obtained by Al/Si substitution are found to be stronger attacked by liquid water as compared with the low-silica samples generated by steaming. Figure 11 shows the corresponding behavior of hydrothermally treated DAY in dependence on the module ($\text{SiO}_2/\text{Al}_2\text{O}_3$ ratio).

At one hand, appearance of EFAl brings a stabilizing effect to the zeolite framework [98] and a more regular structure in the steamed DAY samples. Some observations indicated that the structure of these zeolites heals during dealumination [99, 100]. Orthosilicic acid (H_4SiO_4) migrates from the crystal surface into free framework vacancies generated due to removal of aluminium atoms. Migration of H_4SiO_4 takes place too, if silica gel obtained by precipitation is hydrothermally treated in analogy to the preparation procedure of DAY zeolites [88]. All defects—sorption centers for gases or liquids—are repaired by reorganization of the framework. Because the framework becomes more regular with rising of time and temperature the silica gel loses its sorption behavior. The asymmetrical TOT (T = Si) valence vibration in infrared spectra shifts into the region of wave numbers characteristic of pyrogenic silica at $1100\text{--}1120\text{ cm}^{-1}$.

An important observation gives another explanation for the different behavior of low-silica and high-silica DAY samples. The degradation of silicon-rich surfaces according to (7) proceeds fast. But if the surface of such a sample is aluminated again [75], stabilization of the structure takes place [101]. The stabilizing effect of the surface layer consisting of sodium aluminosilicate may be associated with the elimination of the terminal silanol $\equiv\text{Si-OH}$ groups and a blocking of the energy-rich $\equiv\text{Si-O-Si}\equiv$ bonds near the crystal surface, where water molecules attack the framework. Contrary to the polymeric silica in the dealuminated framework, this aluminium-rich

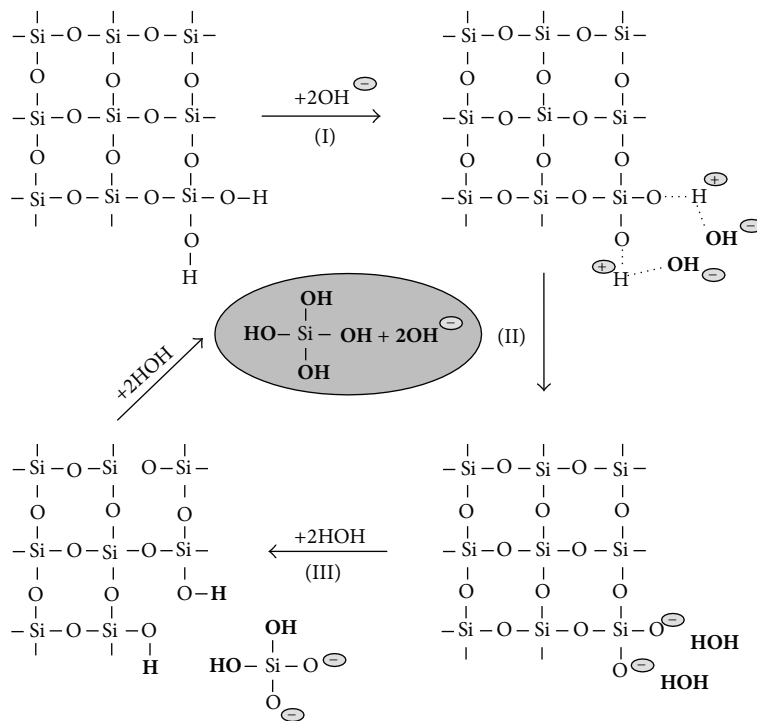


FIGURE 9: Stepwise decomposition of a high-silica zeolite framework by water [96].

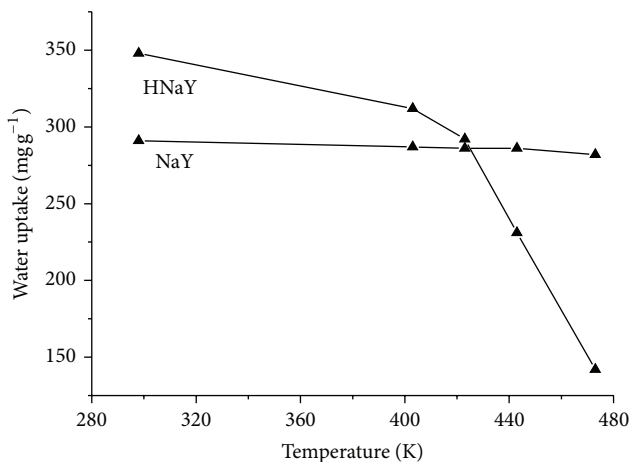


FIGURE 10: Water sorption uptake of zeolites NaY and HNaY after hydrothermal treatment in water of autogenous pressure for 72 hours in dependence on temperature [97].

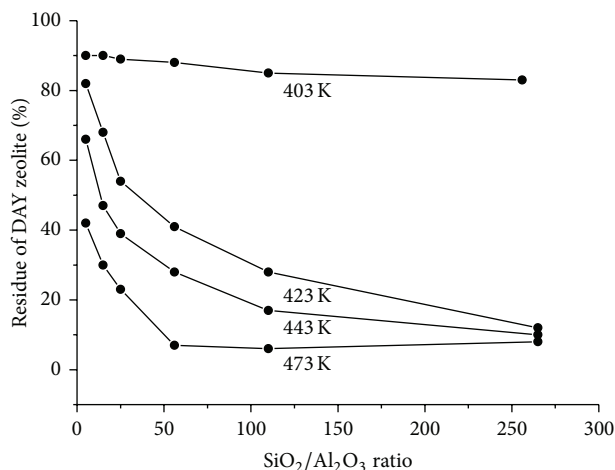


FIGURE 11: Residue of DAY zeolites after hydrothermal treatment in liquid water in dependence on module and temperature [96].

layer contains only monomeric and dimeric silicate units which are detected by Molybdate measurement. Using such an approach, high-silica zeolites may be stabilized against a hydrothermal or alkaline attack [93]. Lutz et al. [102] reported in detail on the external introduction of extraframework sodium aluminosilicate species through an alkaline and combined acid/alkaline pathways using sodium aluminate as well as aluminium-oxo-hydroxo cations [103] or (Al, SiO_x) species into faujasite type zeolite [104]. Alumination in solutions of sodium or potassium aluminate was reported also for other

high-silica zeolites such as silicalite [105], MCM-41 [106], and zeolite Beta [107].

The sodium aluminosilicate surface layer can be functionalized as wafer for catalytically active ingredient. The obtained adsorber/catalyst composites were successfully tested in the conversion of several organics and applied for waste water purification.

2.3.5. *Adsorber/Catalyst Composites.* Active ingredients in adsorber/catalyst composites on the basis of high-silica DAY zeolites are exclusively localized on the crystal surface while

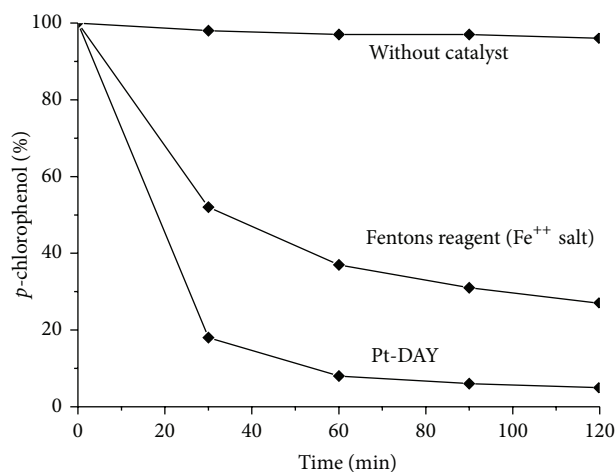


FIGURE 12: Degradation of 1 g per L p-chloro-phenol in water by adding of 4 g H₂O₂ on 10 g of Fenton's reagent, respectively, zeolite Pt-DAY loaded with 5 mg/g platinum [109].

the bulk remains free for adsorption. Thus, high conversion of acetone on an H-DAY composite with Si/Al = 150 or such one of *n*-butane on a Ni-DAY or Pt-DAY analogues has been found [108]. But the specific application of the composites remains in the purification of waste waters. Pollutants such as halogenated hydrocarbons must be removed up to a few nanogram. At the first step of cleaning, the pollution will be separated from liquid phase by adsorption and at the second step it is decomposed by chemical reaction, for example, by oxidation with hydrogen peroxide. Because of the degradation of the toxic agent any regeneration of the composite is not provided.

The decomposition of p-chloro-phenol in water on Pt-DAY was tested comparing to Fenton's reagent (FeSO₄) [109]. The zeolite was loaded by 5 mg, 12 mg, 23 mg, and 47 mg of Pt per g composite. The best effect was obtained with 5 mg/g because of an optimized activation of the admixed hydrogen peroxide. Figure 12 shows the significant advantage of the new composite compared with the classical FeSO₄ using a one-step strategy. In a semitechnical plant, pureness degree lower than 1 ppm has been achieved. Details of preparation and application of adsorber/catalyst composites are discussed in a series of patents [110–114].

2.3.6. Reinsertion of Extraframework Aluminium into Framework Positions. The catalytic activity of zeolites is determined mainly by their framework aluminium. The aluminium content may be varied directly in the synthetic process (zeolite ZSM-5) or, as has been reported here, by subsequent framework dealumination (zeolite Y). The subsequent insertion of external aluminium into zeolites frameworks has been highly discussed from the beginning of eighties. In this case, aluminium chloride [105], clay [115], and alkali aluminate [116] have been suggested as aluminium sources.

For steamed DAY samples, Breck and Skeels [117] have proposed a reinsertion of the extraframework aluminium back into the faujasite framework by treatment of samples

in alkaline solution. Liu and colleagues [118] confirmed this approach by interpretation of ²⁹Si MAS NMR spectra and termed this process as "fine tuning of performance of zeolitic catalysts." Hamdan et al. [119] saw in the "secondary synthesis," a method of achieving an optimal number of Brønsted acid sites responsible for the crack activity for hydrocarbons within the zeolite framework. But reexamination of the process by Engelhardt and Lohse [120] did not confirm this hypothesis. Their doubts concerned especially the interpretation of measured ²⁹Si MAS NMR spectra. Nevertheless, a series of NMR studies supported the reinsertion concept of Klinowski et al. [121–128]. The signals of Si(nAl) building units shift to a higher values by framework dealumination. While the peaks of the Si(4Al) and Si(3Al) units in Figure 13 decrease in intensity, and the signals assigned to Si(1Al) and Si(0Al) increase.

Lutz et al. reexamined the concept proposed by Liu et al. [118] using steamed DAY samples with varying Si/Al ratio [129], different conditions of alkaline leaching [130], and acid leached samples before the alkaline treatment in KOH solution [84]. The authors reported the drastic decrease of the Si(0Al) and the increase of the Si(1Al–4Al) peaks which indicates actually an Al enrichment inside the zeolites framework. However, this phenomenon was also observed when the extraframework aluminium was eliminated by acid extraction [84, 131] (see Figure 13). Since in alkaline treated DAY samples, the newly formed alkali aluminosilicates contribute especially to the Si(3Al) and Si(4Al) signals; the decrease of the Si(0Al) signal should be ascribed to a yet unknown phenomenon.

Bezmann [132], using the Liu approach, studied the mass balance after KOH treated Y samples and found 5% of the silicon and 2% of the aluminium in the filtrate of the batch. Furthermore, the crystallinity of sample decreased to 80%. Lutz et al. [133] provided a detailed mass balance with a similar tendency. The treatment of aluminosilicates and, particularly, metastable zeolites in alkaline solution gives rise to the change in their crystal structure [10]. The effect of increasing solubility of zeolites framework with increasing Si/Al ratio and the formation of Al-rich gels during alkaline treatment of zeolites have already been reported by Zhdanov and Egorova [134] and Stach et al. [135].

Aouali et al. [136] observed desilication and partial decomposition of highly dealuminated zeolite Y framework resulting in Al enrichment. This is the reason why the amorphization of DAY samples increases by treatment in alkaline solution with the rising of Si/Al ratio seen in badly resolved ²⁹Si MAS NMR spectra [129]. Thereby, 39% silicon of the framework with Si/Al = 23 was migrated into newly formed extraframework aluminosilicate or into alkaline solution.

Dessau et al. [137] observed a strong corrosion of the large crystals of silicalite by a treatment in alkaline solution. Groen et al. [138] and Verbroekend and Pérez-Ramirez [139] generated thus controlled mesoporosity in zeolites. Lutz et al. [140] have treated this zeolite on a frit, separating the formed aluminosilicate in the filtrate. Mirodatos and Barthemeuf [141] assumed the participation of extraframework silicon in the formation of the aluminosilicate.

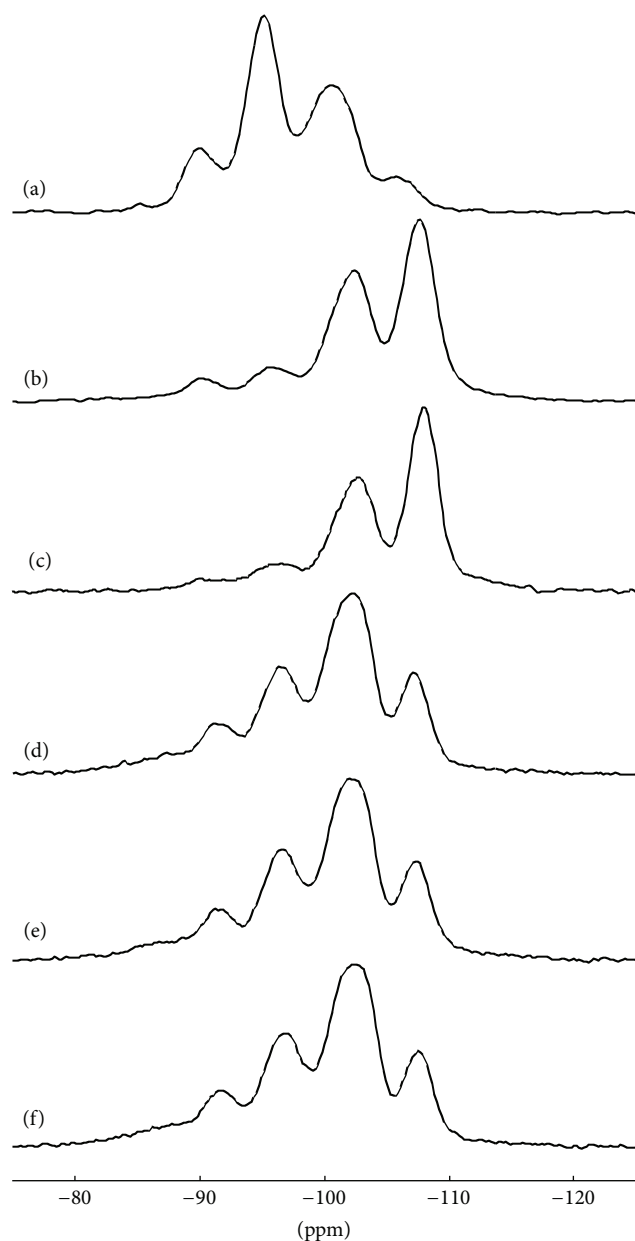


FIGURE 13: ^{29}Si MAS NMR spectra of zeolites NaY (a), steamed DAY (b), acid leached DAY (c), alkaline leached DAY (d), and alkaline leached DAY after acid extraction of the extraframework aluminium with moderate (e) and intensive stirring (f) [130].

In a detailed study on the alkaline reactivity of extraframework species Lutz et al. [87] have shown that EFSi—silica gel at the crystal surface and, in dependence on the steaming conditions, aluminosilicate or clay and silica in the nuclei—contributes to the sample transformation only at a low extent. The aluminosilicate admixture is protected against the attack of sodium or potassium hydroxide by its negative charge and silica gel formed at steaming temperature of 773 K or more is lowly soluble. The observed newly formed sodium or potassium aluminosilicate is generated exclusively from $\text{Al}^{(3+)}$ cations and silicon removed

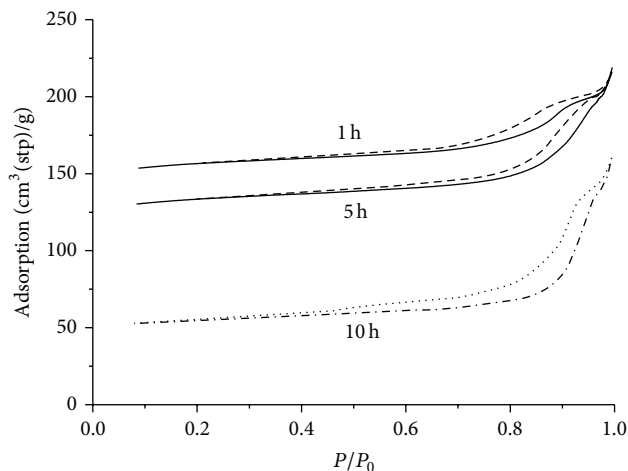


FIGURE 14: Nitrogen isotherms measured at 77 K on DAY steamed at 973 K and 1 bar water pressure in dependence on time [148].

from the dealuminated framework. This means that the “re-insertion” of extraframework aluminium consists in a desilication of the zeolites framework and a formation of additional X-ray amorphous alkali aluminosilicate.

Because of the exchange of protons against alkali metal cations, the Brønsted activity, for example, in conversion of *n*-pentane [142], breaks totally down by use of DAY samples prepared according to “re-insertion” concept given by Liu et al. [118].

2.3.7. Secondary Pore Volume in Steamed Y Zeolites. Much work has been done to characterize the transition of bulk micropores of DAY zeolites into a secondary pore volume [143–147]. Formed mesopores were attributed to reorganization of the framework after removal of aluminium followed by generation of structural defects. The healing of the framework by migrating of orthosilicic acid (H_4SiO_4) into defect positions was discussed too [99, 100, 148]. Formation and healing can be followed by infrared analysis of the formed internal hydroxyl groups [149].

First investigations of the interaction of DAY samples with gases and vapors related to their catalytic behaviors have been performed [150–152] and followed later by systematic studies of their sorption capacity [143]. After the characterization of sorption centers by hydrocarbons, the investigation of the pore structure using nitrogen at 77 K came into the focus of interest. A typical sign of the mesopores in DAY is the hysteresis between the adsorption and desorption loop of the nitrogen isotherm above a relative pressure at p/p_s over 0.5. Nitrogen liquefies in the secondary pore volume and needs, therefore, more energy for evaporation than adsorbed nitrogen molecules. Figure 14 shows typical nitrogen isotherms with such a hysteresis loop.

Using nitrogen uptake techniques, Lutz and colleagues [148] detected a formation of various bulk mesopores in dependence on the conditions of steaming. Framework defects tend to be occupied by migrating H_4SiO_4 , especially at temperatures of 573 K and 673 K. Corresponding diffusion

of orthosilicic acid was described in detail by Iler [74, 153]. Insertion goes down at temperatures above 873 K since the dehydroxylation of the hydroxyl nests accompanied by a rearrangement of the framework and the reduced concentration of offered water takes place.

Mesopores were unquestionably assumed to be the result of pure dealumination of the microporous bulk. Using texture analysis and 3D-TEM measurements, Jansen et al. [154] visualized large mesopores of 0.2–0.4 nm not only within the nuclei but also near to the surface of the DAY crystals. Similar morphology was observed also by Lynch et al., who reported on a secondary pore system without direct connection to the exterior of the crystals [155].

The origin of the closed nuclei and open surface mesopores must be attributed to the inhomogeneous silicon/aluminium contribution over the Y zeolite crystallites [31, 156, 157]. The semiempirical approaches, which describe the Si/Al ratio of faujasite-type zeolites by use of ^{29}Si MAS NMR [158] or X-ray data [159], did not take into account possible effect of such Si/Al gradients [81, 160]. Due to the fine size of the crystallites, a direct proof of the gradient presence is difficult, for example, using EDX analysis. But a hydrothermal instability of the aluminum-rich nuclei and the silicon-rich surface of DAY crystals can be deduced from investigation of faujasite-type zeolites with analogous composition [6].

Kortunov et al. [161] reported on molecular transport in DAY samples. The diffusion measurements have been performed by use of PFG NMR technique with 1,3,5-triisopropylbenzene and *n*-octane as probe molecules. The critical diameters are, respectively, larger and smaller than the inlet of the zeolite micropores. It was found that *n*-octane molecules entered the whole crystal whereas 1,3,5-triisopropylbenzene could not enter the microporous bulk and thus the nuclei mesopores. The idea that the secondary pore system improves the molecular transport of starting materials and products in catalytic conversion processes [19, 55] must be corrected.

One should furthermore assume that DAY samples used by Kortunov contained no or only small amounts of bulk mesopores because of healing of the microporous bulk at 773 K. It seems likely that stronger dealuminated DAY samples steamed, for example, at 973 K, contain such amount of bulk mesopores that traffic of large molecules through the mesoporous network becomes possible [162–164].

Based on current results, one can propose, complementary to the review on mesoporosity in [165, 166], a model containing three types of mesopores with closed mesopores in the crystal nuclei, open mesopores at the crystal surface, and bulk mesopores within microporous bulk. This model is shown schematically in Figure 15.

Generally speaking, even a fourth type of mesopores may occur in the steamed zeolite as a result of nonuniform packing of crystallites with different size in the polycrystalline DAY material. The variation in average crystallite size has been found for a series after dealumination at 773 K, 873 K, and 973 K [55]. It was shown here and in [41] that the average diameter determined by XRD measurements using the Scherrer equation does not vary significantly at 773 K

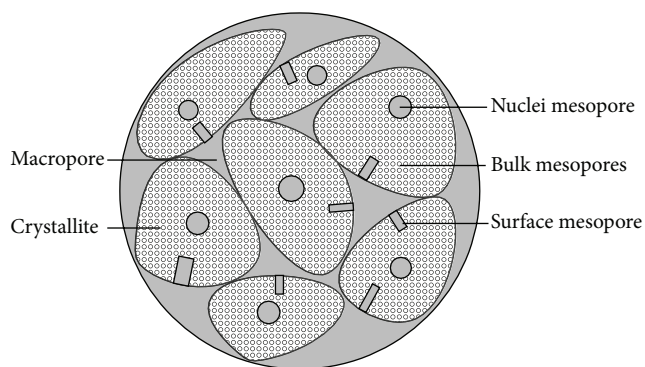


FIGURE 15: Types of mesopores in steamed DAY crystals [31].

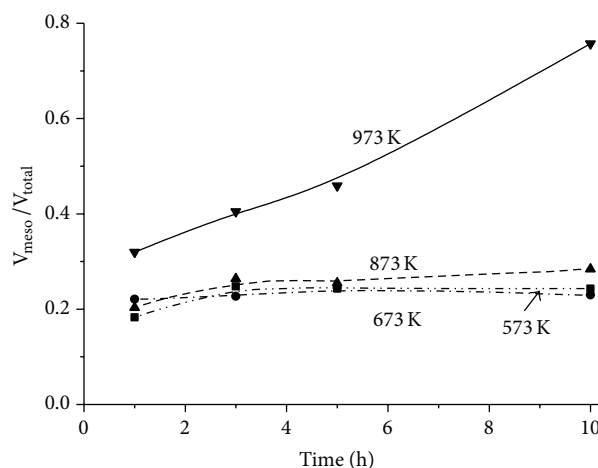


FIGURE 16: Relative mesopore volume ($V_{\text{meso}}/V_{\text{total}}$) of DAY samples in dependence on temperature and steaming time [148].

and 873 K but decreases from 100 nm to 85 nm after 5 hours of steaming at 973 K in sample with zeolite particles of 1000 nm in size. If crystallites become smaller in this way, their package density increases. Therefore, macropores of the intracrystalline space may shrink into larger mesopores which can be detectable by nitrogen measurements at 77 K. However, this assumption cannot be proved actually.

Formation of the secondary pore system leads to a pronounced loss of crystallinity, sorption capacity, and catalytic activity of the zeolite materials. It would be helpful to reduce the mesoporous volume. The first possibility lies in the moderate steaming of samples to guarantee the healing of the framework defects in the microporous bulk (hydroxyl nests) [148]. Performing a gentle and homogeneous dealumination with KY zeolite of higher framework cell which possesses rather equilibrium distribution of ammonium ions inside the structure could provide another solution of this problem. And a third way is associated with minimizing the Si/Al gradient by seeding of NaY synthesis batches with seed solution [156, 167] instead of an insertion of nanoseeds of X zeolite [26].

For an investigation of moderate steaming, commercial NaY zeolite with a Si/Al ratio of 2.7 was exchanged with

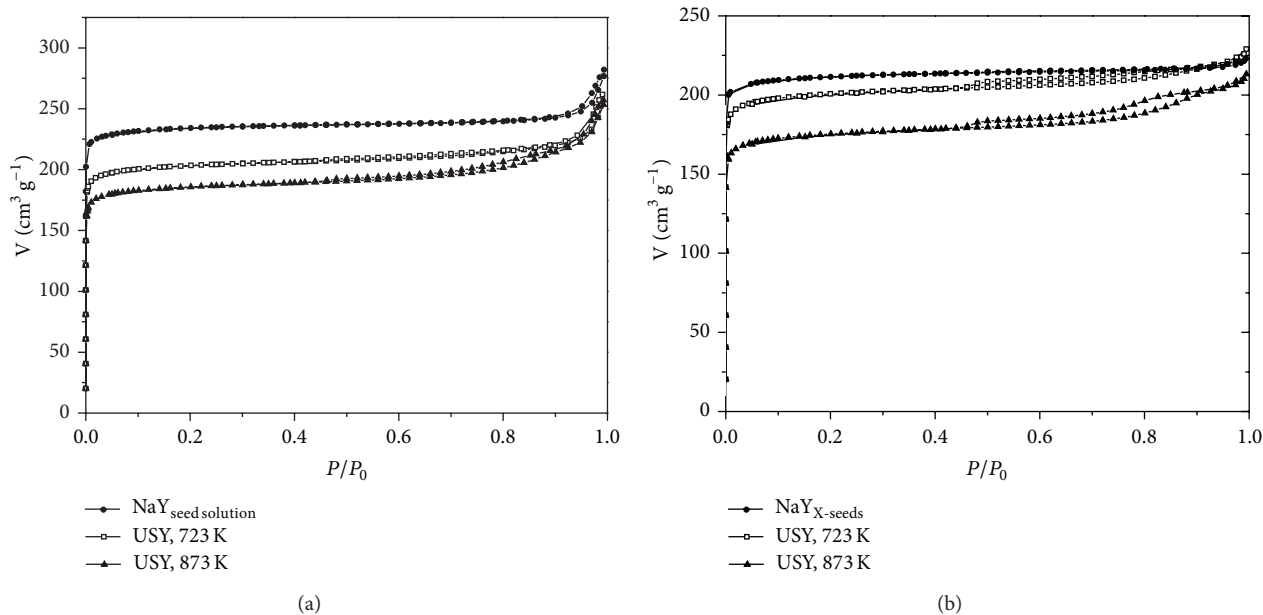


FIGURE 17: Nitrogen isotherms of the initial $\text{NaY}_{\text{seed-solution}}$ (a) and $\text{NaY}_{\text{X-seeds}}$ (b) zeolites and the corresponding DAY samples steamed for 7 hours at 723 K and 873 K, respectively [169].

ammonium ions up to 81%. The formation and healing of the bulk mesopores in dependence on temperature were detected by the presentation of the relative change of the pore volume $V_{\text{meso}}/V_{\text{total}}$ during the steaming time [148]. Figure 16 shows that the contribution of mesopores to the total volume is constant at 573 K and 673 K. Only the mesopore surface S_a changes slightly with the time. It seems likely that V_{meso} is dominated by the volume of the closed nuclei mesopores while the mesopore surface S_{meso} characterizes mainly the open surface mesopores.

As we know, a silicon-rich surface acts as source of orthosilicic acid [74, 153] in silica gel as well as in the steamed DAY samples. Incorporation of H_4SiO_4 into the defects inside bulk framework runs better at low temperature of 573 K–673 K because water is available under these conditions in a sufficient amount for healing procedure. With temperature rise, the portion of bulk mesopores grows slightly at 873 K and significantly at 973 K. At these temperatures nonhealed bulk mesopores contribute mainly to the total mesopore/macropore volume. But healing cannot compensate the framework collapse because of the strong thermal activation of the framework and the drastically reduced concentration of water in the reaction zone.

Synthesis of the ammonium form of zeolite Y from a KY modification followed the idea to get a homogeneous dealumination with a reduced mesopore formation. Owing to a bigger size of potassium ions, the framework of Y zeolite is expanded from 2.468 nm (NaY) to 2.473 nm (KY) and the exchange process should run easier. However, exchange of ammonium for potassium ions succeeded surprisingly only to 80%, similar to NaY zeolite. But steaming of KY zeolite at 873 K where a certain healing of bulk mesopores still takes

place demonstrated an unexpected result [168]. The micropore volume of K-DAY was reduced stronger than that of Na-DAY. It appears that residual $\text{Na}^{(+)}$ ions, localized mainly in the aluminum-rich center of crystals, stabilize the sensitive $\equiv\text{Si}-\text{O}-(\text{Al}^{(-)})$ bonds stronger than $\text{K}^{(+)}$ ions. The latter was more homogeneously distributed over the framework while protons resulting from ammonium complex show a tendency to occupy positions within the nuclei. Due to a repeated ion exchange and steaming procedure, the mesopore volume did not change significantly for both samples but the Si/Al ratio increased gradually from 2.4 (parent NaY and KY) to 4.7 (first steaming) and to 8.4 for both (second steaming).

Modification of the seeding procedure in NaY synthesis looks more attractive in order to decrease the amount mesopores inside the zeolite nuclei [169]. $\text{NaY}_{\text{seed-solution}}$ and $\text{NaY}_{\text{X-seeds}}$ samples of same chemical composition were dealuminated in their ammonium form at 723 K and 873 K. Dealumination changed the framework ratios to 3.3 and 4.2, respectively.

The mesoporous area A_{meso} of both series determined by nitrogen adsorption at 77 K differs significantly. Values of $\text{DAY}_{\text{seed-solution}}$ were smaller than those of $\text{DAY}_{\text{X-seeds}}$. This observation gives the hint to the absence of nuclei mesopores in $\text{DAY}_{\text{seed-solution}}$. The corresponding nitrogen isotherms in Figure 17 show no hysteresis loop at both temperatures investigated. The weak hysteresis for $\text{DAY}_{\text{seed-solution}}$ prepared at 873 K is only responsible for emptying the surface mesopores which inevitably appear during steaming.

The occurrence of nuclei mesopores can be reduced by starting the crystallization of NaY with oligomeric aluminosilicate that hinders the appearance of a strong Si/Al gradient typical of seeding procedures with NaX nanocrystals.

3. Conclusion

The fine-tuning of the Si/Al ratio in zeolite Y framework is achieved by a subsequent steam treatment of NH_4NaY samples at temperatures between 573 K and 973 K in dependence on time. At lower and higher temperatures, decomposition occurs due to acid hydrolysis in steam or the thermal collapse of the framework, respectively. But a certain degree of the decomposition is observed in all other steamed DAY products too. This effect results from a corrosion of the Al-rich nuclei and the Si-rich surface of crystallites which are both hydrothermally instable. The Si/Al gradient inside the framework resulting from the specific synthesis of the parent NaY zeolite can be diminished if the synthesis batch is seeded by a so-called seed solution rather than with NaX nanocrystals.

Due to the framework corrosion, inner and outer mesopores occur in addition to bulk mesopores which appear after removal of framework aluminium. Concentration of inner and outer mesopores can only be reduced decreasing the Si/Al framework gradient. In contrast, bulk mesopores are healed by the migration of orthosilicic acid (H_4SiO_4) into vacancies of the framework at steaming temperatures of 573 K and 673 K, especially. All observed nuclei mesopores are closed therefore they cannot contribute to the transport of greater molecules.

In addition to extraframework aluminium, extraframework siliceous species occur as Al aluminosilicate and silica gel. With increasing steaming temperature, the aluminosilicate is decomposed into clay and silica gel. With the rising temperature, all extraframework components become inactive in alkaline treatment. Therefore, the process of Al enrichment of the zeolite framework during alkaline leaching is associated actually not with migrating of extra framework Al species back into the lattice but it results from the fact that the DAY framework becomes desilicated after such alkaline treatment.

Conflict of Interests

The author declares that there is no conflict of interests regarding the publication of this paper.

References

- [1] D. W. Breck, "Crystalline zeolite Y," U.S. Patent 3130007, 1964.
- [2] R. M. Milton, "Molecular sieve adsorbents," U.S. Patent 2882243, 1959.
- [3] R. M. Milton, "Molecular sieve adsorbents," U.S. Patent 2882244, 1959.
- [4] D. W. Breck, *Zeolite Molecular Sieves*, John Wiley & Sons, New York, NY, USA, 1974.
- [5] E. M. Flanigan, "Molecular sieve zeolite technology: the first twenty-five year," in *Proceedings of the 5th International Conference on Zeolites*, pp. 760–780, Naples, Italy, June 1980.
- [6] C. H. Rüscher, N. Salman, J.-C. Buhl, and W. Lutz, "Relation between growth-size and chemical composition of X and Y type zeolites," *Microporous and Mesoporous Materials*, vol. 92, no. 1–3, pp. 309–311, 2006.
- [7] C. W. McDaniel and P. K. Maher, in *Molecular Sieves*, p. 186, Society of Chemical Industry, London, UK, 1968.
- [8] P. B. Venuto and E. T. Habib Jr., "Catalyst-feedstock-engineering interactions in fluid catalytic cracking," *Catalysis Reviews: Science and Engineering*, vol. 18, no. 1, pp. 1–150, 1978.
- [9] D. J. Rawlence and K. Gosling, "FCC catalyst performance evaluation," *Applied Catalysis*, vol. 43, no. 2, pp. 213–237, 1988.
- [10] R. M. Barrer, *Zeolites and Clay Minerals as Sorbents and Molecular Sieves*, Academic Press, London, UK, 1978.
- [11] S. P. Zhdanov, S. S. Khvoshchev, and N. N. Feoktistova, *Synthetic Zeolites*, vol. 1, Gordon & Breach Science Publishers, New York, NY, USA, 1990.
- [12] G. T. Kerr, "Chemistry of crystalline aluminosilicates. V. Preparation of aluminum-deficient faujasites," *The Journal of Physical Chemistry*, vol. 72, no. 7, pp. 2594–2596, 1968.
- [13] H. K. Beyer, I. M. Belenykaja, F. Hange, M. Tielen, P. J. Grobet, and P. A. Jacobs, "Preparation of high-silica faujasites by treatment with silicon tetrachloride," *Journal of the Chemical Society, Faraday Transactions 1: Physical Chemistry in Condensed Phases*, vol. 81, no. 11, pp. 2889–2901, 1985.
- [14] J. W. Ward, "Thermal decomposition of ammonium Y zeolite," *Journal of Catalysis*, vol. 27, pp. 157–161, 1972.
- [15] P. K. Maher, F. D. Hunter, and J. Scherzer, "Crystal structures of ultrastable faujasites," in *Advances in Chemistry*, vol. 101, chapter 21, pp. 266–278, 1971.
- [16] W. J. Ambs and W. H. Flank, "Thermal behavior of synthetic faujasite," *Journal of Catalysis*, vol. 14, no. 2, pp. 118–125, 1969.
- [17] J. B. Peri, "The nature of ultrastable faujasite," in *Proceedings of the 5th International Congress on Catalysis*, J. W. Hightower, Ed., pp. 329–338, North-Holland, Miami Beach, Fla, USA, 1972.
- [18] G. T. Kerr, A. W. Chester, and D. H. Olson, "Preparation of ultrahigh silicon faujasite by controlled-rate aluminium removal," in *Proceedings of the Symposium on Zeolites*, Jozsef Attila University, 1978, published in *Acta Physica et Chemica, Nova Series*, vol. 24, pp. 169–174, 1978.
- [19] A. Corma and V. Fomés, "Delaminated zeolites as active catalysts for processing large molecules," in *Zeolites and Mesoporous Materials at the Dawn of the 21st Century: Proceedings of the 13th International Zeolite Conference, Montpellier, France, 8–13 July 2001*, A. Galarneau, F. di Renzo, F. Fajula, and J. Védrine, Eds., vol. 135 of *Studies in Surface Science and Catalysis*, pp. 73–82, Elsevier, Amsterdam, The Netherlands, 2001.
- [20] G. T. Kerr, "Chemistry of crystalline aluminosilicates. I. Factors affecting the formation of zeolite A," *The Journal of Physical Chemistry*, vol. 70, pp. 1047–1050, 1966.
- [21] G. T. Kerr, "Chemistry of crystalline aluminosilicates. IV. Factors affecting the formation of zeolites X and B," *The Journal of Physical Chemistry*, vol. 72, no. 4, pp. 1385–1386, 1968.
- [22] D. W. Breck and E. M. Flanigan, "Synthesis and properties of union carbide zeolites L, X and Y," in *Molecular Sieves*, pp. 47–60, Society of Chemical Industry, London, UK, 1968.
- [23] S. P. Zhdanov, "Some problems of zeolite crystallization," in *Molecular Sieve Zeolites-I*, E. M. Flanigan and L. B. Sand, Eds., vol. 101 of *Advances in Chemistry*, chapter 2, pp. 20–43, 1971.
- [24] B. D. McNicol, G. T. Pott, and K. R. Loos, "Spectroscopic studies of zeolite synthesis," *Journal of Physical Chemistry*, vol. 76, no. 23, pp. 3388–3390, 1972.
- [25] E. Thilo, W. Wieker, and H. Stade, "Chemische Untersuchungen von Silicaten, I. Über Beziehungen zwischen dem Polymerisationsgrad silicatischer Anionen und ihrem Reaktionsvermögen mit Molybdänsäure," *Zeitschrift für Anorganische und Allgemeine Chemie*, vol. 340, no. 5–6, pp. 261–276, 1965.

- [26] B. Fahlke, W. Wieker, H. Fürtig, W. Roscher, and R. Seidel, "Untersuchungen zum Bildungsmechanismus von Molsieben," *Zeitschrift für Anorganische und Allgemeine Chemie*, vol. 439, pp. 95–102, 1978.
- [27] W. Wieker and B. Fahlke, "On the reaction mechanism of the formation of molecular sieves and related compounds," in *Zeolites Synthesis, Structure, Technology and Application: Proceedings of an International Symposium, Organized by the "Boris Kidrič" Institute of Chemistry, Ljubljana, on Behalf of the International Zeolite Association*, B. Držaj, S. Hocevar, and S. Pejovnik, Eds., vol. 24 of *Studies in Surface Science and Catalysis*, pp. 161–181, Elsevier, Amsterdam, The Netherlands, 1985.
- [28] J. A. Kostinko, "Intrazeolite chemistry," in *Factors Influencing the Synthesis of Zeolites A, X, and Y*, G. D. Stucky and F. G. Dwyer, Eds., ACS Symposium Series 218, pp. 3–19, American Chemical Society, Washington, DC, USA, 1983.
- [29] C. Berger, R. Gläser, R. A. Rakoczy, and J. Weitkamp, "The synthesis of large crystals of zeolite Y re-visited," *Microporous and Mesoporous Materials*, vol. 83, no. 1–3, pp. 333–344, 2005.
- [30] N. Salman, *Crystal chemical studies on the growth size problem of Y zeolites [Ph.D. thesis]*, Institute for Mineralogy, University of Hannover, Hannover, Germany, 2006.
- [31] W. Lutz, R. Kurzhals, G. Kryukova, D. Enke, M. Weber, and D. Heidemann, "Formation of mesopores in USY zeolites: a case revisited," *Zeitschrift für Anorganische und Allgemeine Chemie*, vol. 636, no. 8, pp. 1497–1505, 2010.
- [32] S. Ferchiche, M. Valcheva-Traykova, D. E. W. Vaughan, J. Warzywoda, and A. Sacco Jr., "Synthesis of large single crystals of templated Y faujasite," *Journal of Crystal Growth*, vol. 222, no. 4, pp. 801–805, 2001.
- [33] S. Ferchiche, J. Warzywoda, and A. Sacco Jr., "Direct synthesis of zeolite Y with large particle size," *International Journal of Inorganic Materials*, vol. 3, no. 7, pp. 773–780, 2001.
- [34] Ch. Baerlocher, L. B. McCusker, and D. H. Olson, *Atlas of Zeolite Framework Types*, Elsevier, Amsterdam, The Netherlands, 2007.
- [35] W. Loevenstein, "The distribution of aluminum in the tetrahedra of silicates and aluminates," *American Mineralogist*, vol. 39, no. 1–2, pp. 92–96, 1954.
- [36] R. M. Barrer and J. D. Falconer, "Ion exchange in feldspaths as a solid-state reaction," *Proceedings of the Royal Society A*, vol. 236, pp. 227–249, 1956.
- [37] R. M. Barrer and W. M. Meier, "Structural and ion sieve properties of a synthetic crystalline exchanger," *Transactions of the Faraday Society*, vol. 54, pp. 1074–1085, 1958.
- [38] W. Lutz, non-published results.
- [39] Q. L. Wang, G. Giannetto, M. Torrealba, G. Perot, C. Kappenstein, and M. Guisnet, "Dealumination of zeolites II. Kinetic study of the dealumination by hydrothermal treatment of a NH_4NaY zeolite," *Journal of Catalysis*, vol. 130, no. 2, pp. 459–470, 1991.
- [40] R. M. Barrer and M. V. Makki, "Molecular sieve sorbents from clinoptilolite," *Canadian Journal of Chemistry*, vol. 42, no. 6, pp. 1481–1487, 1964.
- [41] U. Lohse, E. Löffler, M. Hunger, J. Stöckner, and V. Patzelová, "Hydroxyl groups of the non-framework aluminium species in dealuminated Y zeolites," *Zeolites*, vol. 7, no. 1, pp. 11–13, 1987.
- [42] P. Fejes, I. Kiricsi, I. Hannus, A. Kiss, and G. Schöbel, "A novel method for the dealumination of zeolites," *Reaction Kinetics and Catalysis Letters*, vol. 14, no. 4, pp. 481–488, 1980.
- [43] B. M. Lok and T. P. J. Izod, "Modification of molecular sieves—direct fluorination," *Zeolites*, vol. 2, no. 2, pp. 66–67, 1982.
- [44] G. Engelhardt, U. Lohse, A. Samoson, M. Mägi, M. Tarmak, and E. Lippmaa, "High resolution ^{29}Si n.m.r. of dealuminated and ultrastable Y-zeolites," *Zeolites*, vol. 2, no. 1, pp. 59–62, 1982.
- [45] U. Lohse, I. Pitsch, E. Schreier, B. Parltitz, and K.-H. Schnabel, "Cubic and hexagonal faujasites with varying Si/Al ratios I. Synthesis and characterization," *Applied Catalysis A: General*, vol. 129, no. 2, pp. 189–202, 1995.
- [46] N. Salman, C. H. Rüscher, J.-C. Buhl, W. Lutz, H. Toufar, and M. Stöcker, "Effect of temperature and time in the hydrothermal treatment of HY zeolite," *Microporous and Mesoporous Materials*, vol. 90, no. 1–3, pp. 339–346, 2006.
- [47] U. Lohse, E. Alsdorf, and H. Stach, "Dealuminierte Molekularsieve vom Typ Y. Herstellung und Charakterisierung durch IR-Spektren, DTA/DTG-Messungen und Adsorptionsdaten," *Zeitschrift für Anorganische und Allgemeine Chemie*, vol. 447, no. 1, pp. 64–74, 1978.
- [48] K. P. Schröder and J. Sauer, "Preferred stability of aluminum-oxygen-silicon-oxygen-aluminum linkages in high-silica zeolite catalysts: theoretical predictions contrary to Dempsey's rule," *The Journal of Physical Chemistry*, vol. 97, no. 25, pp. 6579–6581, 1993.
- [49] E. M. Flanigan, H. Khatami, and H. A. Szymanski, "Infrared structural studies of zeolite frameworks," in *Molecular Sieve Zeolites-I*, E. M. Flanigan and L. B. Sand, Eds., vol. 101 of *Advances in Chemistry*, chapter 16, pp. 201–229, 1971.
- [50] W. Lutz, C. H. Rüscher, and D. Heidemann, "Determination of the framework and non-framework $[\text{SiO}_2]$ and $[\text{AlO}_2]$ species of steamed and leached faujasite type zeolites: calibration of IR, NMR, and XRD data by chemical methods," *Microporous and Mesoporous Materials*, vol. 55, no. 2, pp. 193–202, 2002.
- [51] R. Bertram, U. Lohse, and W. Gessner, "Zur Charakterisierung des Extragitter-Aluminiums in Y-zeolithen mittels der Ferronmethode," *Zeitschrift für Anorganische und Allgemeine Chemie*, vol. 567, no. 1, pp. 145–152, 1988.
- [52] H. Fichtner-Schmittler, U. Lohse, H. Mießner, and H. E. Maneck, "Correlation between unit-cell parameter, skeletal stretching vibrations and molar fraction of aluminium of faujasite type zeolites for Si/Al = 1.1–1000," *Zeitschrift für Physikalische Chemie*, vol. 271, pp. 69–79, 1990.
- [53] C. H. Rüscher, J.-C. Buhl, and W. Lutz, " ^{13}P - ^{15}P -determination of the Si/Al ratio of faujasite-type zeolites," in *Zeolites and Mesoporous Materials at the Dawn of the 21st Century: Proceedings of the 13th International Zeolite Conference*, A. Galarneau, F. di Renzo, F. Fajula, and J. Védrine, Eds., vol. 135 of *Studies in Surface Science and Catalysis*, p. 343, Elsevier, Amsterdam, The Netherlands, 2001.
- [54] G. Engelhardt and D. Michel, *High Resolution Solid State NMR of Silicates and Zeolites*, John Wiley & Sons, New York, NY, USA, 1987.
- [55] W. Lutz, C. H. Rüscher, T. M. Gelsing et al., "Investigations of the mechanism of dealumination of zeolite Y by steam: tuned mesopore formation versus the Si/Al ratio," in *Recent Advances in the Science and Technology of Zeolites and Related Materials Part B: Proceedings of the 14th International Zeolite Conference*, E. van Steen, L. H. Callanan, and M. Claeys, Eds., vol. 154 of *Studies in Surface Science and Catalysis*, pp. 1411–1417, Elsevier, London, UK, 2004.
- [56] R. M. Barrer and D. L. Peterson, "Intracrystalline sorption by synthetic mordenites," *Proceedings of the Royal Society A: Mathematical, Physical and Engineering Sciences*, vol. 280, no. 1383, pp. 466–485, 1964.

- [57] G. T. Kerr, "Intracrystalline rearrangement of constitutive water in hydrogen zeolite Y," *The Journal of Physical Chemistry*, vol. 71, no. 12, pp. 4155–4156, 1967.
- [58] G. T. Kerr, "Chemistry of crystalline aluminosilicates: VII. Thermal decomposition products of ammonium zeolite Y," *Journal of Catalysis*, vol. 15, no. 2, pp. 200–204, 1969.
- [59] B. A. Baran, I. M. Belenkaya, and M. M. Dubinin, "Formation and properties of the hydrogen form of mordenite," *Izvestiya Akademii Nauk SSSR, Seriya Khimicheskaya*, vol. 4, pp. 742–749, 1973 (Russian).
- [60] D. W. Breck and G. W. Skeels, *Molecular Sieves II*, vol. 40 of *ACS Symposium Series*, American Chemical Society, Washington, DC, USA, 1977.
- [61] D. W. Breck and G. W. Skeels, "The role of aluminium in the thermal treatment of ammonium exchanged zeolite Y," in *Proceedings of the 6th International Congress on Catalysis*, G. C. Bond, P. B. Wells, and F. C. Tompkins, Eds., pp. 645–659, The Pitman Press, 1976.
- [62] J. Dwyer, F. R. Fitch, G. Qin, and J. C. Vickerman, "Study of the surface composition of zeolites by fast atom bombardment mass spectrometry," *Journal of Physical Chemistry*, vol. 86, no. 23, pp. 4574–4578, 1982.
- [63] T. Gross, U. Lohse, G. Engelhardt, K.-H. Richter, and V. Patzelová, "Surface composition of dealuminated Y zeolites studied by X-ray photoelectron spectroscopy," *Zeolites*, vol. 4, no. 1, pp. 25–29, 1984.
- [64] D. Freude, H. Ernst, and I. Wolf, "Solid-state nuclear magnetic resonance studies of acid sites in zeolites," *Solid State Nuclear Magnetic Resonance*, vol. 3, no. 5, pp. 271–286, 1994.
- [65] J. Jiao, J. Kanellopoulos, W. Wang et al., "Characterization of framework and extra-framework aluminum species in non-hydrated zeolites Y by ^{27}Al spin-echo, high-speed MAS, and MQMAS NMR spectroscopy at $B_0 = 9.4$ to 17.6 T," *Physical Chemistry Chemical Physics*, vol. 7, no. 17, pp. 3221–3226, 2005.
- [66] R. Bertram, W. Gessner, D. Müller, and M. Danner, "Characterization of Al(III) species in basic aluminium chloride flocculants by means of Ferron method and ^{27}Al nuclear magnetic resonance," *Acta Hydrochimica et Hydrobiologica*, vol. 22, no. 6, pp. 265–269, 1994.
- [67] J. Scherzer, "Dealuminated faujasite-type structures with $\text{Si}_2/\text{Al}_2\text{O}_3$ ratios over 100," *Journal of Catalysis*, vol. 54, no. 2, pp. 285–288, 1978.
- [68] N. P. Rhodes and R. Rudham, "Catalytic studies with dealuminated Y zeolite. Part 1.—Catalyst characterisation and the disproportionation of ethylbenzene," *Journal of the Chemical Society, Faraday Transactions*, vol. 89, no. 14, pp. 2551–2557, 1993.
- [69] D. Freude, T. Fröhlich, M. Hunger, and G. Scheler, "NMR studies concerning the dehydroxylation of zeolites HY," *Chemical Physics Letters*, vol. 98, no. 3, pp. 263–266, 1983.
- [70] M. Stockenhuber and J. A. Lercher, "Characterization and removal of extra lattice species in faujasites," *Microporous Materials*, vol. 3, no. 4-5, pp. 457–465, 1995.
- [71] J. Sanz, V. Fornes, and A. Corma, "Extraframework aluminium in steam- and SiCl_4 -dealuminated Y zeolite. A ^{27}Al and ^{29}Si nuclear magnetic resonance study," *Journal of the Chemical Society, Faraday Transactions 1: Physical Chemistry in Condensed Phases*, vol. 84, pp. 3113–3119, 1988.
- [72] W. E. E. Stone, G. M. S. El Shafei, J. Sanz, and S. A. Selim, "Association of soluble aluminum ionic species with a silica-gel surface. A solid-state NMR study," *Journal of Physical Chemistry*, vol. 97, no. 39, pp. 10127–10132, 1993.
- [73] I. Gromann and Th. Gross, "Quantitative analysis of X-ray photoelectron spectroscopy intensities for dealuminated zeolites and supported catalysts where the promoter-forming elements also occur in the support," *Journal of Electron Spectroscopy and Related Phenomena*, vol. 53, no. 3, pp. 99–106, 1990.
- [74] R. K. Iler, *The Chemistry of Silica*, John Wiley & Sons, New York, NY, USA, 1979.
- [75] W. Lutz, E. Löffler, and B. Zibrowius, "Non-framework aluminium in highly dealuminated Y zeolites generated by steaming or substitution," in *Progress in Zeolite and Microporous Materials: Preceedings of the 11th International Zeolite Conference*, H. Chon, S. K. Ihm, and Y. S. Uh, Eds., vol. 105 of *Studies in Surface Science and Catalysis*, pp. 439–446, Elsevier, Amsterdam, The Netherlands, 1995.
- [76] D. P. Siantar, W. S. Millman, and J. J. Fripiat, "Structural defects and cation exchange capacity in dealuminated Y zeolites," *Zeolites*, vol. 15, no. 6, pp. 556–560, 1995.
- [77] W. Lutz, H. Toufar, D. Heidemann et al., "Siliceous extra-framework species in dealuminated Y zeolites generated by steaming," *Microporous and Mesoporous Materials*, vol. 104, no. 1-3, pp. 171–178, 2007.
- [78] K. U. Gore, A. Abraham, S. G. Hegde, R. Kumar, J. Amoureux, and S. Ganapathy, " ^{29}Si and ^{27}Al MAS/3Q-MAS NMR studies of high silica USY zeolites," *Journal of Physical Chemistry B*, vol. 106, no. 23, pp. 6115–6120, 2002.
- [79] H. Hamid and M. A. Ali, *Handbook on MTBE and Other Gasoline Oxygenates*, Marcel Dekker, New York, NY, USA, 2004.
- [80] D. M. Ginter, A. T. Bell, and C. J. Radke, "The chemistry of NaY crystallization from sodium-silicate solution," in *Symposium on Synthesis of Microporous Materials*, M. L. Ocelli and H. E. Robson, Eds., vol. 1, pp. 6–30, Van Nostrand, New York, NY, USA, 1992.
- [81] A. Corma, F. V. Melo, and D. J. Rawlence, "Effect of the nonuniform dealumination on the acidity and catalytic activity of faujasite," *Zeolites*, vol. 10, no. 7, pp. 690–694, 1990.
- [82] G. Engelhardt, U. Lohse, E. Lippmaa, M. Tarmak, and M. Mägi, " ^{29}Si -NMR-Untersuchungen zur Verteilung der Silicium- und Aluminiumatome im Aluminosilikatgitter von Zeolithen mit Faujasit-Struktur," *Zeitschrift für Anorganische und Allgemeine Chemie*, vol. 482, no. 11, pp. 49–64, 1981.
- [83] K. Ehrhardt, M. Suckow, and W. Lutz, "Hydrothermal decomposition of aluminosilicate zeolites and prediction of their long-term stability," in *Catalysis by Microporous Materials: Proceedings of ZEOCAT '95*, H. K. Beyer, H. G. Karge, I. Kiricsi, and J. B. Nagy, Eds., vol. 94 of *Studies in Surface Science and Catalysis*, pp. 179–186, Elsevier, 1995.
- [84] W. Lutz, E. Löffler, M. Fichtelkord, E. Schreier, and R. Bertram, "Non-framework aluminium in highly dealuminated Y zeolites generated by steaming or substitution," in *Progress in Zeolite and Microporous Materials: Preceedings of the 11th International Zeolite Conference*, H. Chon, S.-K. Ihm, and Y. S. Uh, Eds., vol. 105 of *Studies in Surface Science and Catalysis*, pp. 439–446, Elsevier, 1997.
- [85] W. Lutz, D. Heidemann, C. Hübner, and W. Wieker, "Contribution of silica gels to superimposed ^{29}Si MAS NMR spectra of Y zeolites dealuminated by steaming," *Zeitschrift für Anorganische und Allgemeine Chemie*, vol. 627, no. 11, pp. 2559–2564, 2001.
- [86] W. Lutz, W. Wieker, D. Müller, M. Schneider, C. H. Rüscher, and J.-C. Buhl, "Phase transformations in alkaline and acid leached Y zeolites dealuminated by steaming," *Zeitschrift für Anorganische und Allgemeine Chemie*, vol. 626, no. 6, pp. 1460–1467, 2000.

- [87] W. Lutz, R. Bertram, D. Heidemann, R. Kurzhals, C. H. Rüscher, and G. Kryukova, "Reactivity of extra-framework species of USY zeolites in alkaline medium," *Zeitschrift für Anorganische und Allgemeine Chemie*, vol. 637, no. 1, pp. 75–82, 2011.
- [88] W. Lutz, D. Täschner, R. Kurzhals, D. Heidemann, and C. Hübner, "Characterization of silica gels by ^{29}Si MAS NMR and IR spectroscopic measurements," *Zeitschrift für Anorganische und Allgemeine Chemie*, vol. 635, no. 13-14, pp. 2191–2196, 2009.
- [89] J. Felsche and S. Luger, "Phases and thermal decomposition characteristics of hydro-sodalites $\text{Na}_{6+x}[\text{AlSiO}_4]_6(\text{OH})_x \cdot n\text{H}_2\text{O}$," *Thermochimica Acta*, vol. 118, pp. 35–55, 1987.
- [90] G. Engelhardt, J. Felsche, and P. Sieger, "The hydrosodalite system $\text{Na}_{6+x}[\text{SiAlO}_4]_6(\text{OH})_x \cdot n\text{H}_2\text{O}$: formation, phase composition, and de- and rehydration studied by ^1H , ^{23}Na , and ^{29}Si MAS-NMR spectroscopy in tandem with thermal analysis, X-ray diffraction, and IR spectroscopy," *Journal of the American Chemical Society*, vol. 114, no. 4, pp. 1173–1182, 1992.
- [91] J.-C. Buhl, M. Gerstmann, W. Lutz, and A. Ritzmann, "Hydrothermal stability of the novel zeolite type LSX in comparison to the traditional 13X modification," *Zeitschrift für Anorganische und Allgemeine Chemie*, vol. 630, no. 4, pp. 604–608, 2004.
- [92] U. Lohse, *Zur Struktur und zu den Adsorptionseigenschaften von siliciumreichen Molekularsieben [Ph.D. thesis]*, Academy of Sciences of GDR, Berlin, Germany, 1981.
- [93] W. Lutz, B. Zibrowius, and E. Löffler, "Hydrothermal and alkaline stability of high-silica Y-type zeolites in dependence on the dealumination procedure," in *Zeolites and Related Microporous Materials: State of the Art 1994—Proceedings of the 10th International Zeolite Conference, Garmisch-Partenkirchen, Germany, 17–22 July 1994*, J. Weitkamp, H. G. Karge, H. Pfeifer, and W. Hölderich, Eds., vol. 84 of *Studies in Surface Science and Catalysis*, pp. 1005–1012, Elsevier, 1994.
- [94] W. Lutz, B. Zibrowius, and E. Löffler, "Hydrothermal and alkaline stability of high-silica Y zeolites generated by combining substitution and steaming," in *Zeolites: A Refined Tool for Designing Catalytic Sites: Proceedings of the International Zeolite Symposium*, L. Bonnevot and S. Kaliaguine, Eds., vol. 84 of *Studies in Surface Science and Catalysis*, pp. 327–334, Elsevier, 1995.
- [95] W. Lutz, D. Heidemann, R. Kurzhals, and G. Kryukova, "Characterisation of siliceous extra-framework species in day zeolites by ^{29}Si MAS NMR and IR spectroscopic measurements," *Zeitschrift für Anorganische und Allgemeine Chemie*, vol. 636, no. 7, pp. 1361–1367, 2010.
- [96] W. Lutz, H. Toufar, R. Kurzhals, and M. Suckow, "Investigation and modeling of the hydrothermal stability of technically relevant zeolites," *Adsorption*, vol. 11, no. 3-4, pp. 405–413, 2005.
- [97] R. Dimitrijevic, W. Lutz, and A. Ritzmann, "Hydrothermal stability of zeolites: determination of extra-framework species of H-Y faujasite-type steamed zeolite," *Journal of Physics and Chemistry of Solids*, vol. 67, no. 8, pp. 1741–1748, 2006.
- [98] W. Lutz, "Stabilizing effect of non-framework AL on the structure of dealuminated y zeolites under hydrothermal conditions," *Crystal Research and Technology*, vol. 25, no. 8, pp. 921–926, 1990.
- [99] A. T. Steel and E. Dooryhee, "Time dependence of the structural changes occurring in $\text{NH}_4\text{-Y}$ zeolite on dealumination: a preliminary study using energy-dispersive X-ray diffraction," *Zeolites*, vol. 13, no. 5, pp. 336–340, 1993.
- [100] U. Lohse and M. Mildebrath, "Dealuminierte Molekularsieve vom Typ Y zur Porosität dealuminierter Molekularsieve," *Zeitschrift für Anorganische und Allgemeine Chemie*, vol. 476, no. 5, pp. 126–135, 1981.
- [101] W. Lutz, E. Löffler, and B. Zibrowius, "Increased hydrothermal stability of highly dealuminated Y zeolites by aluminations," *Zeolites*, vol. 13, no. 8, pp. 685–686, 1993.
- [102] W. Lutz, W. Gessner, R. Bertram, I. Pitsch, and R. Fricke, "Hydrothermally resistant high-silica Y zeolites stabilized by covering with non-framework aluminum species," *Microporous Materials*, vol. 12, no. 1-3, pp. 131–139, 1997.
- [103] S. Schönherr, H. Görz, W. Gessner, and R. Bertram, "Protolysevorgänge in wäßrigen Aluminiumchloridlösungen," *Zeitschrift für Chemie*, vol. 23, no. 12, pp. 429–434, 1983.
- [104] I. Pitsch, U. Kürschner, D. Müller et al., "Synthesis, characterization and catalytic activity of amorphous Al_2SiO_5 gels from weakly acidic aqueous solutions," *Journal of Materials Chemistry*, vol. 7, pp. 2469–2476, 1997.
- [105] M. W. Anderson, J. Klinowski, and X. Liu, "Alumination of highly siliceous zeolites," *Journal of the Chemical Society, Chemical Communications*, no. 23, pp. 1596–1597, 1984.
- [106] H. Hamdan, S. Endud, H. He, M. N. M. Muhid, and J. Klinowski, "Alumination of the purely siliceous mesoporous molecular sieve MCM-41 and its hydrothermal conversion into zeolite Na-A," *Journal of the Chemical Society, Faraday Transactions*, vol. 92, no. 12, pp. 2311–2315, 1996.
- [107] C. Yang and Q. Xu, "Aluminated zeolites β and their properties part 1.-Alumination of zeolites β ," *Journal of the Chemical Society, Faraday Transactions*, vol. 93, pp. 1675–1680, 1997.
- [108] W. Lutz, D. L. Hoang, G. Lischke, and B. Parltitz, "Extra-framework aluminium in DAY zeolites as carrier for catalytic ingredients," in *Proceedings of the 3rd Polish-German Zeolite Colloquium*, M. Rozwadowski, Ed., pp. 205–214, Nicolaus Copernicus University Press, 1998.
- [109] W. Lutz, R. Bertram, W. Wieker, and M. Jank, "Adsorber-Katalysator-Komposite für Umweltprozesse," in *Neue Entwicklungen zur adsorptiven Gas- und Wasserreinigung*, W. Henschel, Ed., vol. 859 of *Freiberger Forschungshefte A: Verfahrenstechnik/Umwelttechnik*, p. 256, Bergakademie Freiberg, Freiberg, Germany, 2000.
- [110] W. Lutz, P. Kleinschmit, and E. Roland, "Removing organic substances from aq. soln. for sepn. of harmful or useful organic substances," DE Patent 4406776, 1994.
- [111] W. Lutz, "Verfahren zum Entfernen von Stoffen aus wäßrigen Lösungen und Adsorptionsmittel," DE Patent 19531933, 1995.
- [112] W. Lutz, D. Hoang, R. Fricke, and H. Lieske, "Asorber/catalyst composite," DE Patent 19708746, 1997.
- [113] W. Lutz, W. Gessner, and R. Bertram, "Hydrothable catalytically active composites for separating organics from fluid phase," DE Patent 19718929, 1997.
- [114] B. Schlicht, H. J. Redlich, G. Höhne, and W. Lutz, "Verfahren zum Entfernen von problembehafteten Schadstoffen aus Abwasser," DE Patent 10114739, 2001.
- [115] C. D. Chang, S. D. Helling, J. N. Miale, P. W. Schmitt, and E. L. Wu, "Insertion of aluminium into high-silica-content zeolite frameworks. Part 3.-Hydrothermal transfer of aluminium from Al_2O_3 into [AL]ZSM-5 and [B]ZSM-5," *Journal of the Chemical Society, Faraday Transactions 1: Physical Chemistry in Condensed Phases*, vol. 81, pp. 2215–2224, 1985.
- [116] H. Hamdan and J. Klinowski, "Isomorphous substitution of framework silicon by aluminium in silicalite: factors determining resolution of ^{29}Si magic-angle-spinning NMR spectra of pentasil zeolites," *Chemical Physics Letters*, vol. 139, no. 6, pp. 576–580, 1987.

- [117] D. W. Breck and G. W. Skeels, "Zeolite chemistry IV-evidence for the elimination and subsequent reinsertion of framework aluminum during the stabilization of NH_4^+ -Exchanged zeolite X," in *Proceedings of the 5th International Conference on Zeolites*, L. V. C. Rees, Ed., pp. 335–343, London, UK, 1980.
- [118] X. Liu, J. Klinowski, and J. M. Thomas, "Hydrothermal isomorphous insertion of aluminium into the framework of zeolite Y: a convenient method of modifying the siting of Al and Si in faujasitic catalysts," *Journal of the Chemical Society, Chemical Communications*, no. 8, pp. 582–584, 1986.
- [119] H. Hamdan, B. Sulikowski, and J. Klinowski, "Hydrothermal isomorphous substitution of aluminum in faujasitic frameworks: second-generation zeolite catalysts," *Journal of Physical Chemistry*, vol. 93, no. 1, pp. 350–356, 1989.
- [120] G. Engelhardt and U. Lohse, "A reexamination of the hypothesis of Breck and Skeels concerning the reinsertion of aluminum in the framework of dealuminated Y zeolites," *Journal of Catalysis*, vol. 88, no. 2, pp. 513–515, 1984.
- [121] J. Klinowski and P. J. Barrie, "Recent advances in zeolite science," in *Proceedings of the Meeting of the British Zeolite Association*, B. Delmon and J. T. Yates, Eds., Cambridge, UK, April 1989.
- [122] Z. Zhang, X. Liu, Y. Xu, and R. Xu, "Realumination of dealuminated zeolites Y," *Zeolites*, vol. 11, no. 3, pp. 232–238, 1991.
- [123] M. Nayarana and B. D. Murray, "Process for realuminating zeolites," U.S. Patent 5118482, 1992.
- [124] P. J. Barry, L. F. Gladden, and J. Klinowski, "Neutron diffraction studies of realuminated zeolite Y," *Journal of the Chemical Society, Chemical Communications*, no. 8, pp. 592–594, 1991.
- [125] V. Calsavara, E. F. Sousa-Aguiar, and N. R. C. Fernandes-Machado, "Reactivity of USY extraframework alumina in alkaline medium," *Zeolites*, vol. 17, no. 4, pp. 340–345, 1996.
- [126] B. Sulikowski, J. Datka, B. Gil, J. Ptaszynski, and J. Klinowski, "Acidity and catalytic properties of realuminated zeolite Y," *Journal of Physical Chemistry B*, vol. 101, no. 35, pp. 6929–6932, 1997.
- [127] W. Wang and S. J. Hwang, "Effect of treatment conditions on Y-zeolite," *Chinese Journal of Chemical Engineering*, vol. 25, pp. 337–339, 1994.
- [128] D.-S. Liu, S.-L. Bao, and Q.-H. Xu, "Studies on realumination of dealuminated zeolite Y," *Acta Chimica Sinica*, vol. 54, no. 8, pp. 764–771, 1996.
- [129] W. Lutz, U. Lohse, and B. Fahlke, "Chemical reactions during alkaline treatment of dealuminated Y zeolites—impossibility of aluminium reinsertion into the framework," *Crystal Research and Technology*, vol. 23, no. 7, pp. 925–933, 1988.
- [130] W. Lutz, D. Heidemann, C. H. Rüscher, and J.-C. Buhl, "Formation of alkali-aluminosilicate layers on thermochemically dealuminated Y zeolites by alkaline leaching," *Crystal Research and Technology*, vol. 36, no. 1, pp. 9–14, 2001.
- [131] M. Fechtelkord, J.-C. Buhl, W. Lutz, and B. Zibrowius, "Realuminierung von Zeolith DAY infolge Si-Abreicherung," *Zeitschrift für Kristallographie, Supplement*, vol. 9, p. 154, 1995.
- [132] R. D. Bezman, "On the efficiency of insertion of aluminium into the framework of Y-type zeolite by the hydrothermal process of Liu, Klinowski, and Thomas," *Journal of Chemical Society, Chemical Communications*, pp. 1562–1563, 1987.
- [133] W. Lutz, W. Gessner, and D. Müller, "Formation of Al-rich aluminosilicate by alkaline treatment of DAY zeolite dealuminated by steaming," *Zeolites*, vol. 19, no. 2-3, pp. 209–212, 1997.
- [134] S. P. Zhdanov and E. N. Egorova, *Chimija Ceolitov*, Izd. Nauka, Leningrad, Moscow, Russia, 1968.
- [135] H. Stach, U. Lohse, H. Thamm, and W. Schirmer, "Adsorption equilibria of hydrocarbons on highly dealuminated zeolites," *Zeolites*, vol. 6, no. 2, pp. 74–90, 1986.
- [136] L. Aouali, J. Teanjan, A. Dereigne, P. Tougne, and D. Delafosse, "Structural evolution of dealuminated Y zeolites during various chemical treatments," *Zeolites*, vol. 8, no. 6, pp. 517–522, 1988.
- [137] R. M. Dessau, E. W. Valyocsik, and N. H. Goeke, "Aluminum zoning in ZSM-5 as revealed by selective silica removal," *Zeolites*, vol. 12, no. 7, pp. 776–779, 1992.
- [138] J. C. Groen, J. A. Moulijn, and J. Pérez-Ramirez, "Desilication: on the controlled generation of mesoporosity in MFI zeolites," *Journal of Materials Chemistry*, vol. 16, pp. 2121–2131, 2006.
- [139] D. Verbroekend and J. Pérez-Ramirez, "Design of hierarchical zeolite catalysts by desilication," *Catalysis Science & Technology*, vol. 1, no. 6, pp. 879–890, 2011.
- [140] W. Lutz, A. Grossmann, M. Bülow, and Th. Gross, "Questioning Klinowski's concept of isomorphous substitution of silicon by aluminium in the framework of silicates," *Crystal Research and Technology*, vol. 25, no. 2, pp. 135–138, 1990.
- [141] C. Mirodatos and D. Barthemeuf, "Superacid sites in zeolites," *Journal of the Chemical Society, Chemical Communications*, no. 2, pp. 39–40, 1981.
- [142] W. Lutz, U. Kürschner, and E. Löffler, "Fine-tuning of the catalytic activity of dealuminated faujasites by subsequent chemical treatment," in *Proceedings of the 2nd Polish-German Zeolite Colloquium*, M. Rozwadowski, Ed., pp. 165–170, Nicolas Copernicus University Press, 1995.
- [143] U. Lohse, H. Stach, H. Thamm et al., "Dealuminierte Molekularsieve vom Typ Y Bestimmung des Mikro- und Sekundärporenvolumens durch Adsorptionsmessungen," *Zeitschrift für Anorganische und Allgemeine Chemie*, vol. 460, no. 1, pp. 179–190, 1980.
- [144] G. Weber and M. Simonot-Grange, "Characterization of the dealumination effect into H faujasites by adsorption: part 2. The hexane molecule as a pore volume probe," *Zeolites*, vol. 14, no. 6, pp. 433–438, 1994.
- [145] A. Corma, "From microporous to mesoporous molecular sieve materials and their use in catalysis," *Chemical Reviews*, vol. 97, no. 6, pp. 2373–2419, 1997.
- [146] C. S. Triantafillidis, A. G. Vlessides, and N. P. Evmiridis, "Dealuminated H-Y zeolites: influence of the degree and the type of dealumination method on the structural and acidic characteristics of H-Y zeolites," *Industrial & Engineering Chemistry Research*, vol. 39, no. 2, pp. 307–319, 2000.
- [147] K. Sato, Y. Nishimura, N. Matsubayashi, M. Imamura, and H. Shimada, "Structural changes of Y zeolites during ion exchange treatment: effects of Si/Al ratio of the starting NaY," *Microporous and Mesoporous Materials*, vol. 59, no. 2-3, pp. 133–146, 2003.
- [148] W. Lutz, R. A. Shutilov, and V. Y. Gavrilov, "Pore structure of USY zeolites in dependence on steaming condition," *Zeitschrift für Anorganische und Allgemeine Chemie*, vol. 640, no. 3-4, pp. 577–581, 2014.
- [149] S. P. Zhdanov, L. S. Koshelova, T. I. Titova, and M. A. Shubaeva, "IR study of the peculiarities of the stabilization of the NH_4NaY zeolite structure during its hydrothermal dealumination," *Russian Chemical Bulletin*, vol. 42, no. 4, pp. 619–623, 1993.
- [150] D. Barthomeuf and B.-H. Ha, "Adsorption of benzene and cyclohexane on faujasite-type zeolites. Part 1.-Thermodynamic properties at low coverage," *Journal of the Chemical Society, Faraday Transactions 1: Physical Chemistry in Condensed Phases*, vol. 69, pp. 2147–2157, 1973.

- [151] P. D. Hopkins, "Adsorption of hydrocarbons on sodium and demetallated synthetic faujasites," *Journal of Catalysis*, vol. 29, no. 1, pp. 112–119, 1973.
- [152] V. Bosáček, V. Patzelová, C. Hýbl, and Z. Tvarůžková, "Sorption properties of $\text{Na}_x\text{H}_{1-x}\text{Y}$ zeolites," *Journal of Catalysis*, vol. 36, no. 3, pp. 371–378, 1975.
- [153] R. K. Iler, *The Colloid Chemistry of Silica and Silicates*, Cornell University Press, Ithaca, NY, USA, 1955.
- [154] A. H. Jansen, A. J. Koster, and K. P. de Jong, "Three-dimensional transmission electron microscopic observations of mesopores in dealuminated zeolite Y," *Angewandte Chemie International Edition*, vol. 40, no. 6, pp. 1102–1104, 2001.
- [155] J. Lynch, F. Raatz, and P. Dufresne, "Characterization of the textural properties of dealuminated HY forms," *Zeolites*, vol. 7, no. 4, pp. 333–340, 1987.
- [156] B. Sarkar, K. Arya, G. Ravichandran et al., "Ready-to-use seed composition and process thereof," USP 20080182744, 2008.
- [157] G. J. Ray and A. Samonson, "Double rotation and variable field ^{27}Al n.m.r. study of dealuminated Y zeolites," *Zeolites*, vol. 13, no. 6, pp. 410–413, 1993.
- [158] D. Ding, B. Li, P. Sun, Q. Jin, and J. Wang, "A simulated annealing study of Si,Al distribution in the faujasite framework," *Zeolites*, vol. 15, no. 6, pp. 569–573, 1995.
- [159] V. Jorik, "Semiempirical approach to determination of framework aluminum content in faujasite-type zeolites by X-ray powder diffraction," *Zeolites*, vol. 13, no. 3, pp. 187–191, 1993.
- [160] E. Merlen, J. Lynch, M. Bisiaux, and F. Raatz, "Surface modifications during Y zeolite dealumination," *Surface and Interface Analysis*, vol. 16, no. 1–12, pp. 364–368, 1990.
- [161] P. Kortunov, S. Vasenkov, J. Kärger et al., "The role of mesopores in intracrystalline transport in USY zeolite: PFG NMR diffusion study on various length scales," *Journal of the American Chemical Society*, vol. 127, no. 37, pp. 13055–13059, 2005.
- [162] L. Gueudré, M. Milina, S. Mitchell, and J. J. Pérez-Ramirez, "Superior mass transfer properties of technical zeolite bodies with hierarchical porosity," *Advanced Functional Materials*, vol. 24, no. 2, pp. 209–219, 2014.
- [163] J. Kärger and R. Valiullin, "Mass transfer in mesoporous materials: the benefit of microscopic diffusion measurement," *Chemical Society Reviews*, vol. 42, no. 9, pp. 4172–4197, 2013.
- [164] K. Li, J. Valla, and J. Garcia-Martinez, "Realizing the commercial potential of hierarchical zeolites: new opportunities in catalytic cracking," *ChemCatChem*, vol. 6, no. 1, pp. 46–66, 2014.
- [165] K. Möller and Th. Bein, "Mesoporosity—a new dimension for zeolites," *Chemical Society Reviews*, vol. 42, pp. 3689–3707, 2013.
- [166] M.-Ch. Silaghi, C. Chizallet, and P. Raybaud, "Challenges on molecular aspects of dealumination and desilication of zeolites," *Microporous and Mesoporous Materials*, vol. 191, pp. 82–96, 2014.
- [167] G. Clet, J. C. Jansen, and H. van Bekkum, "Synthesis of a zeolite Y coating on stainless steel support," *Chemistry of Materials*, vol. 11, no. 7, pp. 1696–1702, 1999.
- [168] W. Lutz, D. Enke, W.-D. Einicke, D. Taschner, and R. Kurzhals, "Mesopores in USY zeolites II," *Zeitschrift für Anorganische und Allgemeine Chemie*, vol. 638, pp. 2189–2192, 2012.
- [169] W. Lutz, D. Enke, W. Einicke, D. Täschner, and R. Kurzhals, "Mesopores in USY zeolites," *Zeitschrift für Anorganische und Allgemeine Chemie*, vol. 636, no. 15, pp. 2532–2534, 2010.

Research Article

The Anisotropy of Replicated Aluminum Foams

Eugeny L. Furman,¹ Arcady B. Finkelstein,¹ and Maxim L. Cherny²

¹ Department of Foundry Engineering, Ural Federal University, Ekaterinburg 620002, Russia

² Department of Rare Metals, Ural Federal University, Ekaterinburg 620002, Russia

Correspondence should be addressed to Maxim L. Cherny; fs@kompmat.ru

Received 30 November 2013; Revised 23 March 2014; Accepted 24 March 2014; Published 4 May 2014

Academic Editor: Nikolaos Michailidis

Copyright © 2014 Eugeny L. Furman et al. This is an open access article distributed under the Creative Commons Attribution License, which permits unrestricted use, distribution, and reproduction in any medium, provided the original work is properly cited.

The replication casting process gives the open-cell aluminum foams that can be used in many industrial applications as well as in filtering technology. The essential requirement for filters is the uniformity of filtering degree which is defined by the minimal pore size. However the structure of replication castings is often inhomogeneous and the minimal pore radius is decreasing in the direction of melt infiltration. The objective of this investigation is to study the dynamics of melt impregnation of the porous medium by vacuum suction to identify the possibility of reducing the anisotropy. Theoretical data illustrate the processes at the boundary between melt and gas medium. The experiments were carried out using the replication aluminum samples produced according to commercial technology. It was found that the permeability coefficient varies throughout the height of castings. A method for estimation of pressure on the line of melt movement was proposed. The resistance of NaCl layer and circular vents of the mold causes the inhomogeneity of castings. Finally the ways of minimizing the anisotropy were offered.

1. Introduction

Aluminum open-cell foams can be applied in a wide range of possible applications [1]. However their main field of application is filtration nowadays. The technology of replication casting creates the porous structure that differs radically from the pores obtained by powder metallurgy without using the space-holder material (Figure 1). The replicated aluminum foam obtained with vacuum suction has a porosity in the range of 50–65% which is higher than that for sintered porous structures (around 30–35%) and lower than that for replication casting under high pressure (up to 90%) [2, 3]. Relatively high volumetric porosity enables the gravity sedimentation of solid particles. These factors lead to a long-term operation of filter without a significant permeability loss.

The essential requirement for filters is the uniformity of filtering degree which is defined by the minimal pore size ($2r_{\min}$). This task can be solved with technology [3], when prebaked sodium chloride (NaCl) layer is infiltrated with aluminum melt under high pressure. In this case the minimal pore size is determined by the time of NaCl baking. However the technology is rarely used commercially due to its high

production cost. The technology with loose NaCl layer is applied by Composite Materials Ltd. (Ekaterinburg, Russia) [4] for production replicated aluminum foams in commercial scale. Here the granular sodium chloride is preheated in a furnace and is then filled into the mold and infiltrated with molten aluminum using vacuum suction. The technology is cost saving and allows producing a wide range of filters mainly for compressed air and gases. However the minimal pore radius (Figure 1) is often inhomogeneous and is decreasing in the direction of melt infiltration. The anisotropic part of the casting does not match the requirements of the customer and should be removed during machining. Therefore the objective of this investigation is to study the dynamics of melt impregnation of the porous medium by vacuum suction to identify the possibility of reducing the anisotropy.

2. Theory

The minimum pore radius of replicated aluminum foam is derived by the following equation [4]:

$$r_{\min} = \frac{-3\sigma + \sqrt{9\sigma^2 - 8\sigma RP \cos \theta}}{2P}, \quad (1)$$

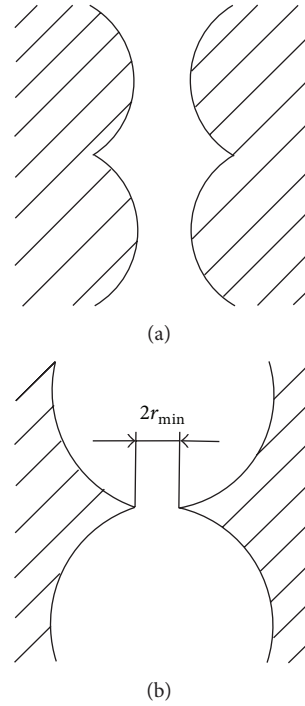


FIGURE 1: The shape of pores obtained by (a) metal sintering and (b) replication casting hatching area depicts metal.

where σ is the surface tension of molten metal, $2R$ is the average size of NaCl particles, θ is wetting angle, and $P = P_{at} - P_{ac} + \rho gh$, where P_{at} is the atmospheric pressure, P_{ac} is the pressure of the air entrapped during melt filtration in the air collar, ρ is the melt density, and h is the height of liquid column.

Hydrostatic pressure will always cause the anisotropy of porous structure. Decreasing the cast height is not an acceptable solution since it will increase the production costs. The influence of hydrostatic pressure can be reduced by increasing the pressure drop during the aluminum melt infiltration.

For example, when the pressure drop equals 60 000 Pa (0,6 atm), sodium chloride fraction is 0,32–0,63 mm and when the cast height equals 200 mm towards filtration, the estimated anisotropy of minimal pore radii caused by hydrostatic pressure (1) along the cast height will be 2.8%, and that is technologically acceptable.

The air is entrapped by melt at the front of melt movement and as a result the air collar is forming. Subsequently the pressure at the air collar is equal to the pressure at the front of melt movement.

The main factor in anisotropy of porous structure is an alternating pressure at the front line of impregnation.

The technology includes vacuum suction of the mold filled with salt granules after melt loading on the surface of NaCl bed. Impregnation does not start at the moment of connection of the mold to a vacuum line. Since the salt granules are not wetted by melt, the spontaneous impregnation does not occur. So there is a certain time gap between melt loading to the surface of NaCl bed and start of impregnation, and this time gap is enough to form the oxide film at the

border of melt and salt. The oxide film at the surface of melted aluminum has sufficiently high mechanical features; its burst pressure depends on the alloy content and for pure aluminum it is 18,000 Pa [5]. Therefore, the initial condition for impregnation is to provide the burst pressure of the oxide film at the border of melt and salt as follows:

$$P(x = l) = 18000 \text{ Pa.} \quad (2)$$

To determine the initial conditions in gaseous phase during the impregnation, it is necessary to solve the task of nonsteady air filtration in the porous medium. During gas filtration the influence of gravity and inertia can be neglected because of the low density of gases. The process of nonstationary gas flow in porous medium is described by Leibenson equation as follows:

$$\frac{\partial P}{\partial \tau} = \frac{K}{2\Delta\mu} \nabla^2 P^2. \quad (3)$$

Equation (3) is a parabolic-type nonlinear equation. In case of unidirectional air filtration, (3) can be presented as

$$\frac{\partial P}{\partial \tau} = \frac{K}{2\Delta\mu} \frac{\partial^2 P^2}{\partial x^2}. \quad (4)$$

Let us evaluate the mold with porous material of uniform cross section and finite length (Figure 2). Initial conditions are provided by pressure P_0 in the volume of salt granules at the initial moment ($\tau = 0$):

$$P(x, \tau = 0) = 101250 \text{ Pa.} \quad (5)$$

The constant pressure equal to the pressure in receiver is established for the boundary between vacuum receiver and porous bed as follows:

$$P(x=0, \tau) = P_{rec}. \quad (6)$$

The velocity of gas filtration is equal to zero for boundary between melt and porous bed; thus,

$$\frac{dP}{dx}(x=l, \tau) = 0. \quad (7)$$

The terminal condition of the task is (2).

Therefore, estimation of nonstationary gas filtration is equivalent to mathematical task of integration of homogeneous Fourier equation (4) with the mentioned-above initial and terminal conditions (5)–(7). The task is to determine flow capacity at the direction parallel to mold's walls at any moment. The dynamic viscosity of gas is accepted to be constant ($\mu = \text{const}$).

Equation (4) is nonlinear and cannot be solved analytically. Here, it is taken as a basis, the solution [6] representing an explicit schedule of the method of finite differences. Monodimensional field of pressures is an initial condition of the task of NaCl bed wetting out by melt.

In the process of wetting out, it comes further.

The subsequent air evacuation from NaCl bed to vacuum receiver is observed during the impregnation, as well as air displacement from porous medium being filled with melt. Consequently, a new source component which describes the air displacement arises in Leibenson equation for a boundary between a melt and air layer. The boundary layer of gas with volume V ,

$$V = S \cdot H \cdot \Delta, \quad (8)$$

with height H and surface S (where Δ is porosity) is taken conditionally as alternating H for estimation of melt line motion as

$$\frac{d(H)}{d\tau} = -\frac{dl}{d\tau}. \quad (9)$$

However, the layer's height H is taken as constant (H -coordinate increment in porous bed) for estimation of gas filtration into outside environment. Taking account of decrease of amount of filling with coming melt is performed by annulation of boundary layer after its total fulfillment. The estimation schedule is presented (Figure 2).

Pressure in this layer is accepted to be equal through all its volume. For this layer, the Mendeleev-Clapeyron equation differentiated with respect to time can be presented as

$$\frac{d}{d\tau}(PV) = \frac{d}{d\tau} \left(\frac{m}{M} RT \right). \quad (10)$$

The process is supposed to go under isothermal conditions. Getting (10) together with (8), (9) can be transformed into the following:

$$\left(\frac{dP}{d\tau} \right)_l = \frac{RT}{H\Delta SM} \frac{dm}{d\tau} + \frac{Pdl}{Hd\tau}. \quad (11)$$

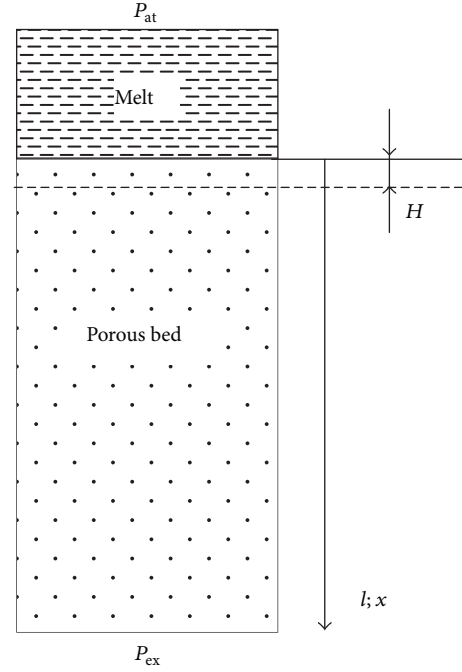


FIGURE 2: Principal scheme of NaCl porous bed impregnation.

If the boundary “melt-gas medium” was immovable ($dl/dt = 0$), (11) could be written in the form (4), but since there is a gas displacement from porous medium being filled by melt, (4) for boundary air layer on the line of melt motion is added by the source component from (11):

$$\left(\frac{dP}{d\tau} \right)_l = \frac{K}{2\Delta\mu} \frac{d^2 P^2}{dx^2} + \frac{Pdl}{Hd\tau}. \quad (12)$$

Equation (12) physically means that pressure in the boundary layer increases because of air displacement by melt and this pressure increases proportionally to the melt motion.

Estimation of pressure change on the line of impregnation is performed by a system of Leibenson equations (4) for gas flow with boundary conditions (6) and (12), as well as by Darcy's equation for fluid flow:

$$\frac{dl}{d\tau} = \frac{K \cdot (P_{ex} - P_l)}{\mu_l \cdot l}, \quad (13)$$

where $dl/d\tau$ is the average linear flow rate through porous medium, $P_{ex} - P_l$ is the change of fluid pressure through porous medium, μ_l is the dynamic viscosity of the fluid, l is the thickness of infiltrated porous medium along the direction of fluid flow, and K is permeability of porous medium.

The boundary conditions for fluid are as follows: P_l is determined by (12) and $P_{ex} = 101250$ Pa. The common initial condition for fluid and gas is $l = 0$.

This solution includes reduction of grid points, while melt is filling the salt layer. Because of approximation errors, it makes no sense to keep the amount of grid points steady, that is, to perform recalculation of pressures over the coordinate, coordinate increment, and time increment. The program is written in Delphi with Borland environment.

3. Experimental

In the process of impregnation, the air is entrapped by melt into the air collars. Their size is a function of residual air pressure [4]. Thus, there is a possibility to study the pressure experimentally on the line of impregnation using the dimensions of these air collars. To eliminate the influence of random collar selection, it is reasonable to use such an integrated characteristic property of porous metal as permeability coefficient. The method of the permeability coefficient evaluation is published [4].

Commercial metal mold with cylindrical cross section (Figure 3) was used for experimental samples production. The mould is placed on a vacuum receiver and is connected with it through gas valve. In commercial mold the bottom is covered by a plug, and vacuum suction is performed by air filtration through a circular vent between the mold and the plug. The gap creates sufficient hydraulic resistance. So the framed net was used instead of the full-metal plug during the experiments. The layer of cold salt was placed over the net to eliminate the filtration of melt into the vacuum receiver. Aluminum (Al) 99.95 (A95 grade in Russia) was used as melt in all experiments for proper control of physical and chemical characteristics of the process. The NaCl used in experiments was a commercial evaporated sodium chloride of such producers as Tyret salt mine OJSC, Uralkali. The sodium chloride was previously dried and sieved to obtain the desired granules fraction.

Inner diameter of working space of the mould is 30 mm and length is 140 mm including the metal head on the top –40 mm and cold salt layer on the bottom –20 mm. The obtained composite cast with 80 mm length was cut into 8 samples with 7 mm thickness. The granules of NaCl were removed from samples by dissolving in water. Porosity of the samples was estimated by weighting, supposing that all pores in the samples are open and interconnected.

The impregnation was carried out under isothermal conditions in order to prevent changes in the physical characteristics of the melt and NaCl during the impregnation. The temperature of aluminum melt, NaCl granules, and mold was equal to 700°C; the level of vacuum is indicated in Figures 4 and 5.

The results of permeability coefficient's calculation compared with experimental data are presented in Figures 4 and 5.

4. Discussion

The experimental results show that the permeability coefficient varies throughout the height of castings. A good repeatability of calculated and experimental results was observed with use of salt granules with fraction of 0.315–0.63 mm (Figure 4). Slightly higher variations between estimated and experimental data are observed for NaCl fraction of 1.5–2.5 mm (Figure 5). But the shape of curves and depth of inhomogeneous area (about 20% of the cast length) are identical both in theory and in practice. That proves the efficiency of proposed method for estimation of pressure on the line of melt movement.



FIGURE 3: Commercial metal mould.

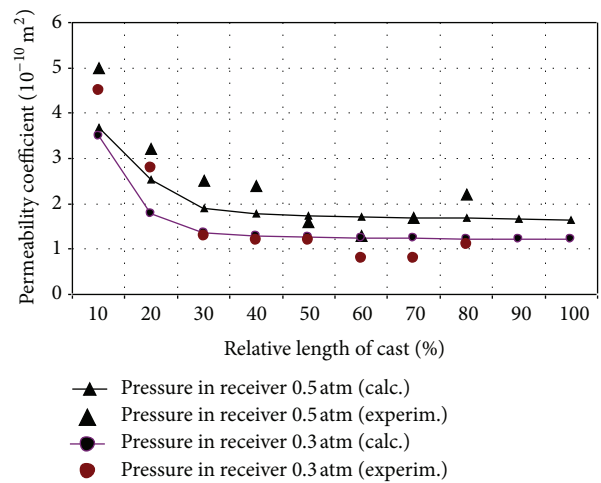


FIGURE 4: Variation of the permeability coefficient throughout the height of a cast with NaCl fraction of 0.315–0.63 mm.

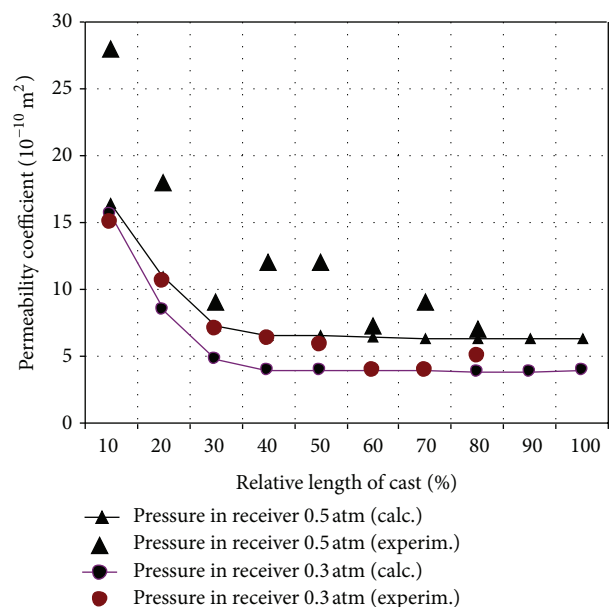


FIGURE 5: Variation of the permeability coefficient throughout the height of a cast with NaCl fraction of 1.5–2.5 mm.

The impregnation can be divided into two stages. The first stage is when the air pressure on the line of melt movement varies from oxide film burst pressure to pressure in receiver. The second stage is when the pressure on the line of melt movement is stable at the level of receiver pressure. The estimation of the size of anisotropic area under different conditions was performed to assess the capability for anisotropy control.

These estimations showed that a relative length of anisotropic area depends only on physical and chemical characteristics of gas and liquid phases (Figure 6).

The calculation was made for aluminum and zinc melts to demonstrate the effect of melt viscosity on the size of inhomogeneous area. Since zinc melt's viscosity is significantly lower than that for aluminum melt, the size of inhomogeneous area increases.

The size of inhomogeneous area does not depend on the permeability coefficient K . This may be explained by direct dependence on the filtration velocity from K for both liquid and gas phases.

The Hagen-Poiseuille equation is applied to liquid and gas phases contemporarily to solve the task of simultaneous flow of liquid and gas in cylindrical capillary [7]. The paper [7] shows that a velocity of liquid at the initial stage depends on the length of capillary and the viscosity of liquid and gas; that is, it is determined by formation of "air pillow" on the line of liquid flow. Presented in this paper, the estimations and experiments not only prove this hypothesis [7], but also allow evaluating the absolute amount of gas pressure on the line of melt movement and taking into account the distinctive features of melt, particularly the presence of solid oxide layers and specific features of impregnation technology (applying of vacuum suction or external pressure).

5. Conclusion

The present paper shows that it is impossible to decrease a relative amount of inhomogeneous area theoretically. In industrial scale, as it was mentioned above, the bottom of the mould is covered not by framed net but by a full-metal plug, and this significantly increases the total resistance of the system "NaCl layer + circular vent" (circular vent can be approximated as a part of filling). That is why the inhomogeneity is observed throughout the cast length at the direction of melt filtration in industrial.

We have found it reasonable to add a layer of fine fraction of NaCl granules above a basic filling layer before the impregnation [8] to stabilize the pressure. The size of NaCl particles in this additional layer should be as small as possible to provide higher resistance to the melt flow, but it must not be less than the capillary gaps in the basic filler to avoid the washing out by melt. Melt is casted down on the surface of fine fraction salt. During the vacuum suction the impregnation starts when a pressure on the boundary "fine fraction salt-melt" reaches the value of capillary pressure, that is, when it exceeds sufficiently a capillary pressure for the basic NaCl layer (or the pressure of destruction of oxide films). When the melt flows with higher resistance in fine fraction salt the

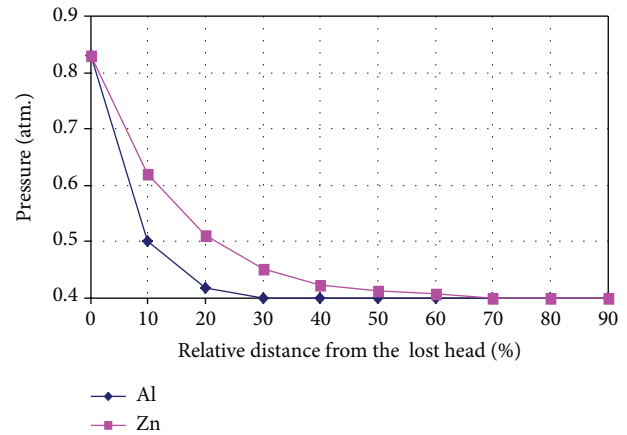


FIGURE 6: Gas pressure on the line of melt motion.

pressure in the basic salt layer becomes steady at the level of vacuum receiver pressure. Then the part of casting filled with fine fraction salt is disposed during machining. A serious restriction of this method is the impossibility to obtain the products with combination of porous and solid-metal parts.

The other method can be applied to avoid the cast inhomogeneity [9]. Here the salt layer is impregnated with melt at irreducibly small vacuum (0.2 atm). Then the form is covered by a cap and the compressed air is delivered under the cap. The obtained gradient of pressure allows adjusting the radius of air collar, as well as all performance characteristics of product within a rather wide range. This method allows producing the items that combined the porous and solid-metal parts, yet the instrumentation is more complicated in this case.

Conflict of Interests

The authors declare that there is no conflict of interests regarding the publication of this paper.

References

- [1] J. F. Despois, *Replicated aluminium foam, processing and properties [Doctoral Thesis]*, Institute of Materials, Ecole Polytechnique Federale de Lausanne, 2005.
- [2] J.-F. Despois and A. Mortensen, "Permeability of open-pore microcellular materials," *Acta Materialia*, vol. 53, no. 5, pp. 1381–1388, 2005.
- [3] A. Jinnapat and A. Kennedy, "The manufacture and characterisation of aluminium foams made by investment casting using dissolvable spherical sodium chloride bead preforms," *Metals*, vol. 1, no. 1, pp. 49–64, 2011.
- [4] E. Furman, A. Finkelstein, and M. Cherny, "Permeability of aluminium foams produced by replication casting," *Metals*, vol. 3, no. 1, pp. 49–57, 2013.
- [5] E. Furman, A. Finkelstein, and Y. Yun, "Tensile strength analysis of oxide film on the aluminium melt surface," in *Proceedings of the 11th Russian Conference on Structure and properties of metal and slag melts*, vol. 2, pp. 213–215, South Urals State University, Ekaterinburg, Russia, 2004.

- [6] J. S. Aronofsky and R. Jenkins, "Unsteady flow of gases through porous media," in *Proceedings of the 1st US National Congress of Applied Mechanics*, pp. 763–771, Illinois Institute of Technology, Chicago, Ill, USA, 1952.
- [7] J. R. Ligenza and R. B. Bernstein, "The rate of rise of liquids in fine vertical capillaries," *Journal of The American Chemical Society*, vol. 73, no. 10, pp. 4636–4640, 1951.
- [8] E. Furman, A. Finkelstein, and I. Furman, "Method of replicated foam production," Patent RU 2 256 530 B 22 D 25/00, 2005.
- [9] B. Pastukhov, M. Mitrofanov, E. Furman et al., "Method of replicated foam production," Patent RU 1 814 247 B 22 D 25/00, B 22 D 27/00, C 21 C01/0, 1995.

Review Article

Geometric Models for Isotropic Random Porous Media: A Review

Helmut Hermann¹ and Antje Elsner²

¹ *Institute for Solid State and Materials Research, IFW Dresden, P.O. Box 270116, 01171 Dresden, Germany*

² *Institute for Informatics, TU Dresden, 01062 Dresden, Germany*

Correspondence should be addressed to Helmut Hermann; h.hermann@ifw-dresden.de

Received 9 October 2013; Accepted 26 February 2014; Published 30 April 2014

Academic Editor: Thomas Hipke

Copyright © 2014 H. Hermann and A. Elsner. This is an open access article distributed under the Creative Commons Attribution License, which permits unrestricted use, distribution, and reproduction in any medium, provided the original work is properly cited.

Models for random porous media are considered. The models are isotropic both from the local and the macroscopic point of view; that is, the pores have spherical shape or their surface shows piecewise spherical curvature, and there is no macroscopic gradient of any geometrical feature. Both closed-pore and open-pore systems are discussed. The Poisson grain model, the model of hard spheres packing, and the penetrable sphere model are used; variable size distribution of the pores is included. A parameter is introduced which controls the degree of open-porosity. Besides systems built up by a single solid phase, models for porous media with the internal surface coated by a second phase are treated. Volume fraction, surface area, and correlation functions are given explicitly where applicable; otherwise numerical methods for determination are described. Effective medium theory is applied to calculate physical properties for the models such as isotropic elastic moduli, thermal and electrical conductivity, and static dielectric constant. The methods presented are exemplified by applications: small-angle scattering of systems showing fractal-like behavior in limited ranges of linear dimension, optimization of nanoporous insulating materials, and improvement of properties of open-pore systems by atomic layer deposition of a second phase on the internal surface.

1. Introduction

The development of models for random porous media and the setting-up of structure-property relationships have benefitted substantially from the rich body of theoretical work on disordered matter. Beginning with Ziman's famous book on models of disorder [1] treatises like that on the physics of structurally disordered matter [2], the physics of foam [3], mechanical properties of heterogeneous materials [4], effective medium theory for disordered microstructures [5], structure-property relations of random heterogeneous materials [6], transport, and flow in porous media [7] followed. Parallel to this progress in physics, mathematical methods for the description of random systems have been improved as documented in textbooks on stochastic geometry and its applications [8–10]. Activities of bridging ideas developed in physics and materials science on the one hand and of methods established by mathematicians on the other hand can be found, for example, in [10–14].

In this review we consider models for random isotropic porous media of both closed-pore and open-pore type. The pore surfaces have, at least piecewise, spherical curvature with arbitrary distribution of radii of curvature (for simplicity, called pore size distribution below). There is no restriction regarding the volume fraction of pores. The considered models are based on rules for arranging spheres in the three-dimensional space. Three types of rules are used: random arrangement of noninteracting spheres (Boolean model, this model is not restricted to spherical shape of pores), dense-random packing of hard spheres (DRP), and random packing of partially penetrable spheres each consisting of a hard core and a soft shell (cherry-pit model). The latter one appears as a numerical interpolation scheme between the Boolean model and the DRP method. A model for a porous medium is made by arranging spheres according to one of the above rules and, thereafter, allotting solid material to the space of the model which is not covered by any sphere. Such a model can be refined by coating the pore surfaces with a second solid phase.

The models are characterized by their basic geometrical features—volume fraction of pores, V_V , specific surface area, S_V , pore size distribution, $f(r)$, and correlation function, $C(r)$. On one hand, these characteristics are required to interpret experimental data, for example, small-angle scattering curves. On the other hand, they are important for understanding and control of the interplay between structure and physical properties of random porous media.

Physical properties of the models are discussed in terms of an effective medium approach. Explicit expressions for macroscopic elastic moduli, thermal and electrical conductivity, and static dielectric constant are given.

The definitions of the geometrical characteristics are explained in Section 2, the models are described in Section 3, physical properties are discussed in Section 4, and applications to experimental situations are presented in Section 5.

2. Geometrical Characteristics

The pore space is described as a random set A . We consider volume fraction $V_V(A)$, specific surface area $S_V(A)$, pore size distribution $f(r)$, and correlation function $C_A(r)$ as geometrical characteristics of A . It is useful to introduce the complement of A consisting of the part of the space which does not belong to A . The complement of A is indicated by A^c . This notation is standard in stochastic geometry [10]. For example, if A denotes the pore space of the porous medium, $c_p = V_V(A)$ and $c_b = V_V(A^c) = 1 - c_p$ are the volume fraction of the pore space and the solid bulk phase, respectively. $S_V(A) = S_V(A^c)$ is the same for A and A^c .

The pore space A is described by the shape function:

$$s^p(\mathbf{r}) = \begin{cases} 1, & \mathbf{r} \in A \\ 0, & \text{otherwise.} \end{cases} \quad (1)$$

The volume fraction c_p of pores is defined by the probability of finding a random test point \mathbf{r}_1 in A :

$$c_p = V_V(A) = P(\mathbf{r}_1 \in A). \quad (2)$$

If $s^p(\mathbf{r})$ is known c_p can be calculated by

$$c_p = \frac{1}{V} \int_V s^p(\mathbf{r}) dV. \quad (3)$$

The correlation function

$$C_p(\mathbf{r}) = P(\mathbf{r}_1 \in A, \mathbf{r}_2 \in A), \quad \mathbf{r} = \mathbf{r}_1 - \mathbf{r}_2, \quad (4)$$

denotes the probability of finding two random test points $(\mathbf{r}_1, \mathbf{r}_2)$ inside the pore space. It is calculated from the shape function by

$$C_p(\mathbf{r}) = \frac{1}{V} \int_V s^p(\mathbf{u} + \mathbf{r}) s^p(\mathbf{u}) dV_{\mathbf{u}}. \quad (5)$$

Because of isotropy it depends only on the distance $r = |\mathbf{r}_1 - \mathbf{r}_2|$ between the test points

$$C_p(r) = \frac{1}{4\pi} \int_{\Omega} C_p(\mathbf{r}) d\Omega, \quad (6)$$

where Ω is the solid angle. Replacing index p by b and setting $s^b(\mathbf{r}) = 1 - s^p(\mathbf{r})$ one obtains from ((1), (5), and (6)) for the correlation function of the solid phase

$$C_b(r) = 1 - 2c_p + C_p(r). \quad (7)$$

The specific surface area of A is defined by

$$s_p = S_V(A) = \lim_{\epsilon \rightarrow 0} \frac{P(\mathbf{r}_1 \in S_{\epsilon})}{2\epsilon}, \quad (8)$$

where $P(\mathbf{r}_1 \in S_{\epsilon})$ is the probability of finding a random test point \mathbf{r}_1 in S_{ϵ} and S_{ϵ} is defined by all points of the three-dimensional space the distance of which from the surface $S(A)$ is less than ϵ . If the correlation function of the system is known, s_p is related to $C_p(r)$ by [10]

$$s_p = -4 \lim_{r \rightarrow 0} \frac{dC_p(r)}{dr}. \quad (9)$$

For illustration we consider the most simple case of a single pore with radius R in a sample of volume V as a model for a dilute system of equal pores; that is, $c_p \ll 1$. The volume fraction and the specific surface area are given by $c_p = 4/3\pi R^3/V$ and $s_p = 4\pi R^2/V$, respectively. The integral in formula (5) is evaluated as the convolution integral of a spherical shape function [16]. Neglecting terms of the order c_p^2 one obtains

$$C_p(r) = \begin{cases} c_p \left(1 - \frac{3r}{4R} + \frac{r^3}{16R^3} \right), & 0 \leq r \leq 2R \\ 0, & r > 2R. \end{cases} \quad (10)$$

Polydisperse systems are additionally characterized by a size distribution function $f(r)$ with mean value

$$m = \int x f(x) dx \quad (11)$$

and variance

$$\sigma^2 = \int (x - m)^2 f(x) dx. \quad (12)$$

3. Models

3.1. Poisson Grain Model. The Poisson grain model (also known as Boolean model, see [10]) is an important and versatile model for generating random two-phase structures. It is created in two steps. In the first step a random (Poisson) point field is generated (here in the three-dimensional space) with number density ν of points. This point field has the following property. Considering an arbitrary finite region B with volume $V(B)$, the number $N(B)$ of points situated within B is a random variable. The probability that $N(B)$ takes the value n is

$$P(N(B) = n) = \frac{[\nu V(B)]^n}{n!} \exp(-\nu V(B)), \quad n = 0, 1, \dots \quad (13)$$

The numbers $N(B_1), N(B_2), \dots$ are independent random variables if the regions B_1, B_2, \dots do not overlap. Practically, the point field, that is, the coordinates of the points, can be produced using a random number generator for numbers equally distributed in finite coordinate intervals.

In the second step, respectively, one sphere is placed on each point of the point field where the size distribution of the spheres is arbitrary. The set-theoretical union of all spheres represents a random set A with volume fraction

$$V_V(A) = 1 - \exp(-\nu\bar{V}), \quad (14)$$

where $\bar{V} = (4\pi/3) \int_0^\infty x^3 f(x) dx$ is the mean volume of the spheres.

Consider definition (2) of volume fraction for the special case that A is generated using equal spheres with radius R and choose a sphere of the same radius for B in (13). Then the probability that B does not contain any point of the Poisson point field, that is, $n = 0$ in (13), is equal to the probability that the center of the sphere B has always a distance $r > R$ to any point of the point field. This is exactly definition (2) for the volume fraction of A^c , $V_V(A^c) = \exp(-\nu(4\pi/3)r^3) = 1 - V_V(A)$ which gives (14) for the considered special case. The general result (14) is obtained using the same idea.

The specific surface area of the model is

$$S_V = \nu [1 - V_V(A)] \bar{S}, \quad (15)$$

where $\bar{S} = 4\pi \int_0^\infty x^2 f(x) dx$ is the mean surface area of the spheres.

The correlation function as defined in (5) and (6) is

$$C_A(r) = 2c_A - 1 + (1 - c_A)^2 \exp(\nu\gamma(r)), \quad (16)$$

where $c_A = V_V(A)$ and $\gamma(r)$ is the correlation function of a single sphere averaged over the size distribution $f(r)$ according to

$$\gamma(r) = \frac{4\pi}{3} \int_{r/2}^\infty x^3 \left(1 - \frac{3r}{4x} + \frac{r^3}{16x^3}\right) f(x) dx. \quad (17)$$

The first formulation of the model was given by Porod [17] for equal spheres. A fundamental and general description can be found in [10].

Identifying the space covered by spheres in the Boolean model with the pore space of a random porous medium, one obtains

$$\begin{aligned} c_p &= V_V(A), \\ s_p &= S_V. \end{aligned} \quad (18)$$

Figure 1 shows a cutout of a Boolean model with constant distribution of radii in the interval from 1 to 2. Note that some of the small spheres may be not visible because they can be covered completely by large spheres.

3.2. Random Packing of Hard Spheres. The model of hard spheres is easily defined by the condition that two particles

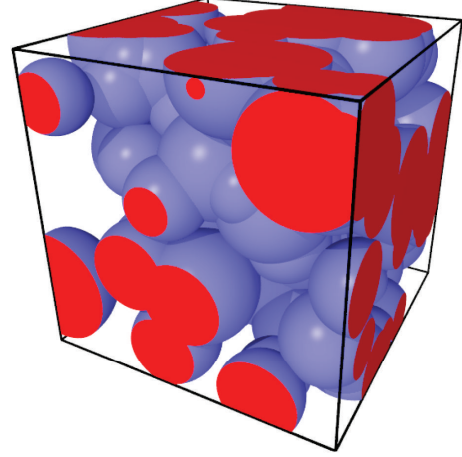


FIGURE 1: Cutout of a Boolean model with sphere radii equally distributed in the interval (1, 2), box size = 5, and volume fraction $V_V = 0.81$.

cannot overlap. Despite the simplicity of the model it appears very complex especially if the packing fraction of spheres is high. For equal spheres, packing fractions of 0.74 (regular hexagonal and face-centered cubic structure), 0.68 (regular body-centered cubic), and 0.636 (dense-random packing) are obtained. While regular packing of spheres has been known as a model for the arrangement of atoms in simple crystal structures [18], Bernal [19] proposed the model of dense-random packed spheres as an approach to the structure of simple liquids. Early reviews on construction algorithms and applications of randomly packed sphere models can be found in [20–22]. More recently, Löwen [23] reviewed methods for analyzing hard sphere systems such as the Percus-Yevick theory, the density-functional approach, and methods of computer simulations from the physical point of view. Mathematical theories are described in [10].

In this work we use the force-biased algorithm for the generation of computer models of hard spheres. This algorithm includes the simulation of systems with arbitrary size distribution of spheres and works very efficiently [24–26]. The algorithm starts with a dilute system of randomly distributed spheres in a parallelepipedal container with periodic boundary conditions applied. Initially, each sphere i has an inner hard core diameter $2r_i^{h,0}$ and an outer diameter $2r_i^{s,0}$. During iteration step n , distances $r_{ij} < r_i^{h,n} + r_j^{h,n}$ between two spheres are not allowed. No interaction occurs for $r_{ij} \geq r_i^{s,n} + r_j^{s,n}$. If $r_i^{h,n} + r_j^{h,n} < r_{ij} < r_i^{s,n} + r_j^{s,n}$, sphere i is shifted from position \mathbf{x}_i^n to position \mathbf{x}_i^{n+1} according to

$$\mathbf{x}_i^{n+1} = \mathbf{x}_i^n + \sum_{j=1}^{z_i} P_{ij} \frac{\mathbf{x}_i^n - \mathbf{x}_j^n}{|\mathbf{x}_i^n - \mathbf{x}_j^n|}, \quad (19)$$

where P_{ij} depends on the diameters of spheres i and j and on control parameters and z_i is the number spheres which have overlapped with sphere i . Quantity P_{ij} is only used to optimize the convergence of the algorithm. It does not represent any physical interaction. After each step n the packing fraction is

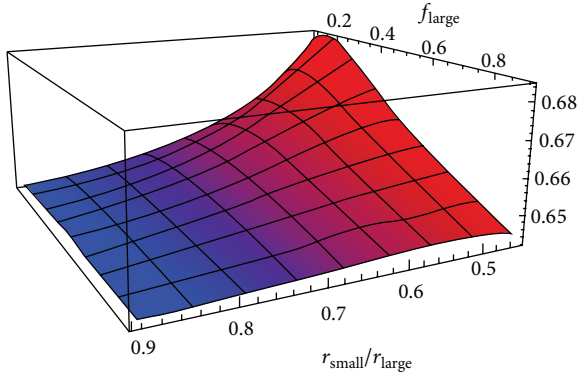


FIGURE 2: Volume fraction of systems of dense-random packed spheres with bimodal distribution of radii versus size ratio $r_{\text{small}}/r_{\text{large}}$ of spheres and number fraction f_{large} of large spheres.

enhanced by adjusting the sphere diameters at constant box size. Denoting the maximum number of iteration steps by n_{max} , $r_i^{s,n} - r_i^{h,n} \rightarrow 0$ for all i if $n \rightarrow n_{\text{max}}$.

The algorithm is terminated if either the desired packing fraction is attained, or if no further progress can be achieved, or if $n = n_{\text{max}}$. For details see [24–27].

The volume fraction of spheres and the specific surface area of a system of packed hard spheres with number density $\nu = N/V$ are simply given by

$$V_V = \nu \int_0^{\infty} \frac{4\pi}{3} r^3 f(r) dr, \quad (20)$$

$$S_V = \nu \int_0^{\infty} 4\pi r^2 f(r) dr, \quad (21)$$

respectively.

Figure 2 shows V_V of systems of dense-random packed hard spheres with bimodal size distribution. For a size ratio of 0.45 of small-to-large spheres the volume fraction has a maximum of 0.684 at a number fraction of 0.2 of large spheres. The maximum packing fraction decreases as the size ratio approaches 1 and takes the value of 0.636 for equal spheres.

There are no exact formulas for the correlation function of dense hard sphere systems. Current approximations and discussions of this problem can be found, for example, in [10, 11, 23]. Monte-Carlo simulations based on the definition (4) can be used to calculate the correlation function for numerically simulated hard sphere systems.

3.3. Penetrable Sphere Models. Penetrable sphere models can be used to describe open-pore structures. Widom and Rowlinson [28, 29] introduced a penetrable sphere model for the study of liquid-vapor phase transitions. In this model, the spheres are allowed to overlap completely. The main difference to the Boolean model described above consists in the definition of a potential energy which is related to the volume occupied by the overlapping spheres. The Widom-Rowlinson model was first extended and applied to studies on phase behavior of complex fluids in [30, 31]. Similar models were described by a number of authors [32–40]. Note that the force-biased algorithm described in the previous

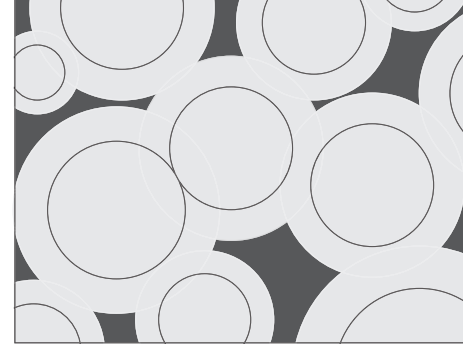


FIGURE 3: Construction scheme of the cherry-pit model. Circles (solid lines) mark the pits, gray regions are the spheres which partially overlap, and the solid material is black.

section shows features of a penetrable sphere model during the rearrangement process.

Torquato [41–43] introduced the penetrable concentric-shell model which is called cherry-pit model for brevity. In this model, each sphere of radius R is composed of an impenetrable core of radius λR (the pit) surrounded by a perfectly penetrable shell of thickness $(1 - \lambda)R$. For the case of randomly distributed sphere centers, the limits of $\lambda = 0$ and $\lambda = 1$ correspond to the Boolean model and the random hard sphere one, respectively. Approximate analytical expressions for volume fraction and specific surface area of this model were presented in [6, 39, 40, 44]. Results of numerical simulations with equally sized spheres [45] agreed reasonably with the predictions for the volume fractions by [39, 40]. Formulas with improved accuracy for volume fraction and specific surface area of the cherry-pit model with equally sized spheres have been given in [46, 47]. The cherry-pit model is a variable model which appears as an interpolation scheme communicating between the Boolean model and the hard sphere packing paradigm. Also it allows to vary the degree of open-porosity by changing the value of λ . While previous studies of the cherry-pit model concentrated on using equally sized spheres actual progress has been achieved by introducing arbitrary size distributions of the spheres [48].

Samples of the cherry-pit model can be generated by means of the force-biased procedure for packing of hard spheres. After choosing the number N of the spheres, the desired size distribution, and the intended packing fraction, the procedure is started. The result consists in the set of the coordinates (x_i, y_i, z_i) , $i = 1, 2, 3, \dots, N$, the radii λr_i of the spheres, and the achieved packing fraction ϕ_h given by (20). The corresponding cherry-pit model is obtained by identifying the spheres of the simulated system with the pits of the cherry-pit model. The union of all spheres with radii r_i represents the pore space of the model. The procedure is illustrated in Figure 3. Figure 4 shows cherry-pit models generated from a system of randomly packed pits with Gamma distributed radii

$$f(r) = \frac{b^p}{\Gamma(p)} r^{p-1} \exp(-br), \quad r \geq 0, \quad (22)$$

and $\bar{r} = p/b$, $\sigma^2 = p/b^2$, $\Gamma(p) = \int_0^{\infty} t^{p-1} \exp(-t) dt$.

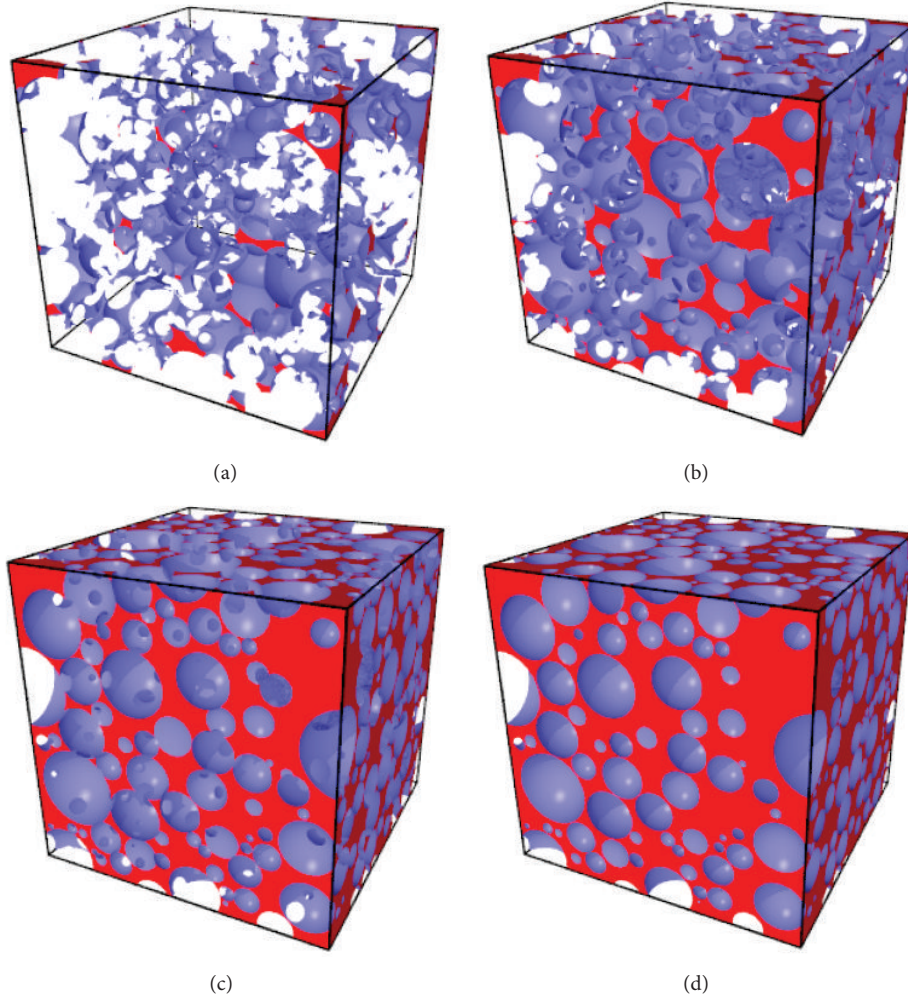


FIGURE 4: Models for porous media generated using the cherry-pit model; Gamma distributed pore size; mean pore size $\bar{r} = 1$, and variance $\sigma^2 = 0.5$; packing fraction of the pit system $\phi_h = 0.60$; $\lambda = 0.75, 0.85, 0.95, 1.00$ for ((a), (b), (c), and (d)).

The samples shown in Figure 4 differ by the values of λ chosen for the construction of the cherry-pit models. Clearly, the degree of open-porosity rises with decreasing λ -values.

The volume fraction of a simulated model is determined using the point-count method where random test points are scattered in the simulation box. The number of test points situated in pores divided by the number of all test points gives an estimate for the volume fraction of pores. The specific surface area is calculated in a similar way. Here, the random test points are distributed on the surfaces of the spheres of the cherry-pit model. The number of points on the surface of a sphere not covered by any other sphere contributes to the surface of the model. The number of contributing points to the number of all points gives an estimate for the surface area of the model. Figure 5 illustrates the statistical reliability of the simulations and its dependence on the size of the model measured by the number of spheres of the simulated cherry-pit model. The standard deviation of both V_V and S_V , each divided by the mean value of the corresponding quantity, decreases with increasing box size. The statistical accuracy of the volume fraction is of the order of 0.25% for $N \geq 10^4$. The

specific surface area is determined with an statistical accuracy of less than 2% for $N = 10^4$ and 0.5% for $N = 10^5$.

Statistical analysis of large numbers of simulated monodisperse [47] and polydisperse [48] cherry-pit models revealed that the volume fraction, V_V , of spheres and the specific surface area, S_V , are given by the approximate formulas:

$$V_V = \phi_h + (1 - \phi_h) \Phi \left(\frac{3\sqrt{2\pi}}{2} \frac{(1 - \lambda)\phi_h}{\lambda(1 - \phi_h)} \right), \quad (23)$$

$$\Phi(z) = \frac{2}{\sqrt{\pi}} \int_0^z \exp(-t^2) dt, \quad (24)$$

$$S_V = \frac{3}{\lambda r_{\text{ref}}} \phi_h \exp \left(-\frac{9\pi}{4} \frac{(1 - \lambda)^2 \phi_h^2}{\lambda^2 (1 - \phi_h)^2} \right). \quad (25)$$

Again, relations (18) apply if the spheres describe the pore space of a medium. Expressions (23) and (25) depend on the quantities ϕ_h and λ , which characterize the basic system of randomly packed hard spheres and the construction scheme

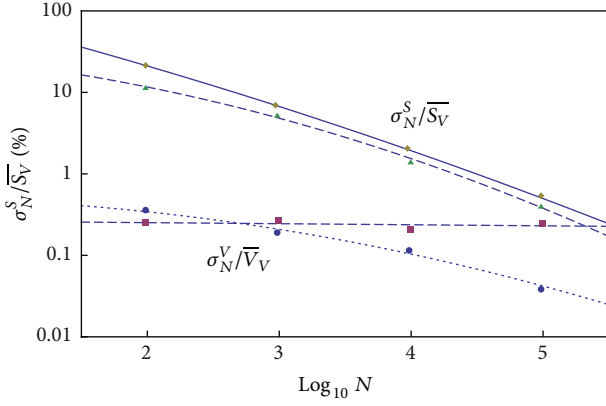


FIGURE 5: Normalized standard deviation σ_N^V / \bar{V}_V and σ_N^S / \bar{S}_V of respectively volume fraction, V_V , and specific surface area, S_V , of cherry-pit models with Gamma distributed radii and $\sigma/\bar{r} = 0.707$ versus number N of spheres used for the construction of a model. The standard deviation is calculated from 10 samples for each model. S_V : rhombuses and solid line: $\lambda = 0.75$, triangles and dashed line: $\lambda = 0.95$; V_V : circles and dotted line: $\lambda = 0.75$, squares and dashed line: $\lambda = 0.95$.

of the cherry-pit model, respectively. Parameter r_{ref} defines the unit of length of the system. For monodisperse systems it is equal to the sphere radius. In the polydisperse case the relation

$$\frac{r_{\text{ref}}}{\bar{r}} = a + b \left(\frac{\sigma}{\bar{r}} \right)^2 \quad (26)$$

with $a = 1.014 \pm 0.002$, $b = 0.454 \pm 0.006$ follows from fitting (25) to the values of the specific surface areas of simulated cherry-pit models [48]. Parameters \bar{r} and σ are the mean value and the standard deviation of the radii distribution, respectively, defined by ((11), (12)). The error appearing for $\sigma \rightarrow 0$ in (26) is below 2%.

Expression (23) does not depend on any parameter related to the size distribution of spheres. So it appears as quite a general relation. Detailed analyses in [48] showed that (23) is most reliable for systems with $0.40 \leq \phi_h \leq 0.71$, $c_p \leq 0.8$ and for size distributions with σ/\bar{r} up to about 3.5 (\bar{r} is the mean radius of spheres). Figure 6 compares (23) to simulated data obtained from systems with 10.000 spheres generated at periodic boundary conditions where the radii are distributed according to a Gamma distribution [48].

Formula (25) is accurate in the limits of few percent for $\sigma \leq 0.25$. The impact of the skewness of the size distributions on the accuracy of (25) is negligible. Figure 7 illustrates the validity of (25).

3.4. Interphase Models

3.4.1. Limit of Very Thin Interphase Layer. We start with one of the models for a porous medium with a single bulk phase. The pore space is characterized by its volume fraction V_V and the specific surface area S_V . Then, the internal surface

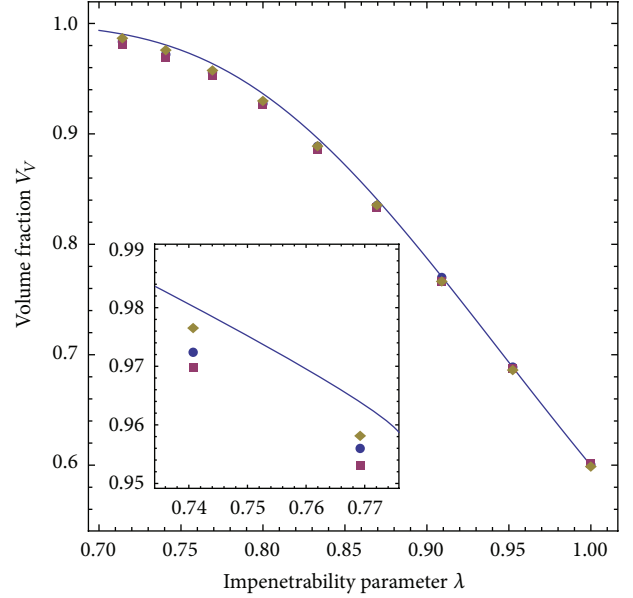


FIGURE 6: Volume fraction of cherry-pit models for Gamma distributed pore size with $\sigma/\bar{r} = 0.25$ (rhombuses), 0.71 (squares), and 1.00 (circles).

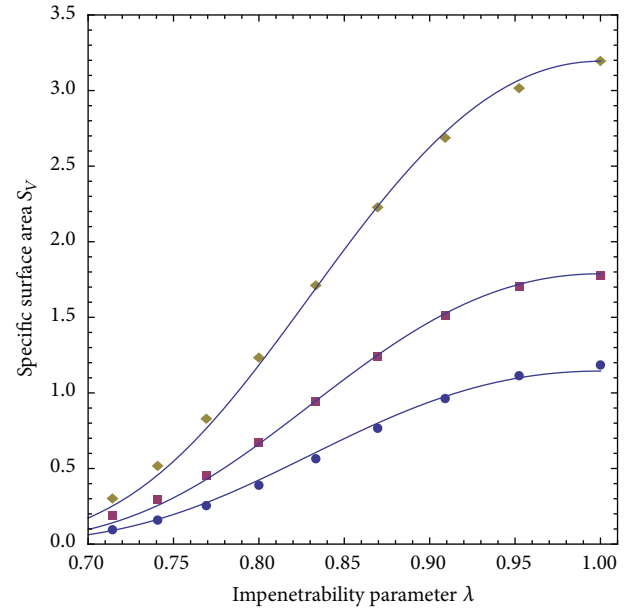


FIGURE 7: Specific surface area of cherry-pit models for Gamma distributed pore size with $\sigma/\bar{r} = 0.25$ (rhombuses), 0.71 (squares), and 1.00 (circles).

of the model is coated by a layer of a second solid phase of thickness δt . This layer is called interphase. Denoting the smallest radius of curvature of a pore of the model by r_{min} , for $\delta t \ll r_{\text{min}}$, the volume fraction of the layer is approximately

$$c_i = \delta t S_V, \quad (27)$$

the volume fraction of the pores reduces to

$$c_p = V_V - \delta t S_V, \quad (28)$$

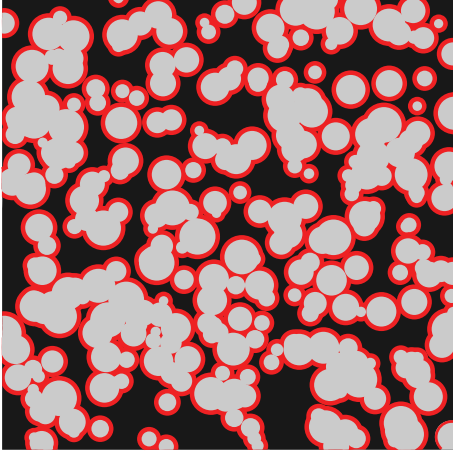


FIGURE 8: Planar intersection of a Boolean interphase model, pores-light gray, bulk phase-black, and interphase layer-red.

and the volume fraction of the bulk phase remains

$$c_b = 1 - V_V = 1 - c_p - c_i. \quad (29)$$

3.4.2. Boolean Interphase Model. Another way to calculate the volume fraction of the interphase is to compare two models differing only by the size of the spheres used for the construction. Consider a Boolean model 1 generated using spheres with size distributions $f_1(r)$. The space not covered by any sphere defines the bulk phase 1. Reducing the radius of each of the spheres of exactly this model by δt a second model 2 is obtained with size distribution $f_2(r) = f_1(r - \delta t)$, where $f_1(r) = 0$ for $r \leq \delta t$ is required. This model defines the pore space. Then, the interphase of thickness δt is given by the space neither belonging to the bulk phase 1 nor to the pore space and the volume fraction of the interphase follows as

$$c_i = V_V(1) - V_V(2). \quad (30)$$

Figure 8 shows the intersection of a Boolean interphase model. For the special case of Boolean models with spheres of equal radius R one obtains

$$c_i = \left\{ 1 - \exp\left(-\nu \frac{4\pi}{3} R^3\right) \right\} - \left\{ 1 - \exp\left(-\nu \frac{4\pi}{3} (R - \delta t)^3\right) \right\}. \quad (31)$$

For $\delta t \ll R$,

$$c_i = \exp\left(-\nu \frac{4\pi}{3} R^3\right) 4\pi\nu R^2 \delta t = \nu(1 - V_V(1)) 4\pi R^2 \delta t \quad (32)$$

follows which corresponds to ((15), (27)).

3.4.3. Hard Sphere Interphase Models. For interphase models based on one hard sphere system the volume fraction of the interphase is calculated similarly. Assuming a Gaussian distribution of radii

$$f(r) = \frac{1}{\sqrt{2\pi}\sigma} \exp\left(-\frac{(r - \bar{r})^2}{2\sigma^2}\right) \quad (33)$$

the volume fraction of the interphase is according to (20):

$$c_i = \frac{4\pi\rho}{3} \left\{ \bar{r} [\bar{r}^2 + 3\sigma^2] - (\bar{r} - \delta t) [(\bar{r} - \delta t)^2 + 3\sigma^2] \right\}. \quad (34)$$

In the limit $\delta t \ll \bar{r}$ one obtains with ((21), (33)) analogously to (27)

$$c_i = 4\pi\rho (\bar{r}^2 + \sigma^2) \delta t = S_V \delta t. \quad (35)$$

3.4.4. Cherry-Pit Interphase Model. The cherry-pit model with one bulk phase can be transformed to an interphase model in a similar way as the Boolean model and the hard spheres one. However, expression (14) for the volume fraction of pores for the cherry-pit model does not depend explicitly on the pore size. Remembering that the hard core radius r_h and the corresponding pore radius r_p are related by

$$r_h = \lambda r_p \quad (36)$$

and considering two monodisperse cherry-pit models 1 and 2 characterized by the same values of ϕ_h and r_h but different pore size r_{p1}, r_{p2} with $r_{p2} = r_{p1} - \delta t$ and $\lambda_1 = r_h/r_{p1}$, $\lambda_2 = r_h/r_{p2}$, the volume fraction of the interphase of the corresponding cherry-pit interphase models is

$$c_i = V_V(\phi_h, \lambda_1) - V_V(\phi_h, \lambda_2), \quad \lambda_2 = \frac{\lambda_1}{1 - \delta t/r_{p1}}. \quad (37)$$

Setting $\lambda_1 = \lambda$, $\delta t = r\delta\lambda/\lambda$, replacing

$$\frac{V_V(\phi_h, \lambda) - V_V(\phi_h, \lambda + \delta\lambda)}{\delta\lambda} \quad (38)$$

by

$$\frac{\partial V_V(\phi_h, \lambda)}{\partial \lambda} \quad (39)$$

and carrying out $\delta\lambda \rightarrow 0$ one obtains from ((23), (25))

$$c_i = r \frac{\delta\lambda}{\lambda} S_V = \delta t S_V \quad (40)$$

which corresponds with (27).

3.5. Reconstruction. It is often important to generate models not from mathematical algorithms or rules but from experimentally obtained structural information. Such information is basically incomplete for random systems. The generation of models from experimental data or reconstruction must therefore focus on reproducing important structure parameters like volume fraction, pore size distribution, or correlation functions. The problem of reconstruction is related to the well-known field of stereology (see chapter 10 in [10]). A typical problem of stereology is, for example, to estimate the size distribution of particles from the length distribution of chords inside particles where the chords are determined from linear sections of the considered sample. Few problems are exactly solved, for example, the determination of the size distribution of pores from planar sections of the sample if

the pores have spherical shape. The size distribution of the pores determines, however, not yet the spatial distribution of the spheres. In this case, small-angle scattering data would be helpful to complete information about spatial correlations of the 3-dimensional arrangement of the pores.

Procedures for the reproduction of random structures have been successfully developed in recent years. Roberts generated 3-dimensional models from 2-dimensional images [49]. Yeong and Torquato [50, 51] proposed a procedure applicable to very different types of random media. Hilfer and Manwart [52] used physical properties like conductivity and permeability in order to improve reconstruction. Reconstruction from microtomographic images was carried out by Øren and Bakke [53]. Ohser and Schladitz [14] presented general methods of computational image analysis. Methods for the reconstruction of random media of the type described by the Poisson grain model have been developed by Arns et al. [54, 55]. Problems occurring with reconstruction on the nanometer scale have been addressed by Prill et al. [56].

4. Structure-Property Relationships

Properties of random heterogeneous materials including porous media have been considered in many theoretical studies. The effective medium theory see, for example, [4, 5], and its combination with the maximum entropy approach [57] have been proven as a powerful tool to understand macroscopic properties, and various structure models have been considered for the study of structure-property relations of heterogeneous materials [6, 7, 58–60]. Among the different structure models, the Poisson grain model appears as one of the most successful approaches for establishing structure-property relationships of random media [58, 61–66]. Recent work on the optimization of property combinations of random media by means of structure variation can be found in [67, 68].

We consider the composite sphere assemblage model (see, e.g., [4]) and related effective medium theories (see, e.g., [5]) as most adequate for the models described in the previous sections. Explicit expressions for dielectric constants, thermal conductivity, and isotropic elastic moduli of models consisting of a matrix and spherical inclusions have been derived and discussed in [4, 5, 67–69]. Below, the idea of this approach is explained for the example of the thermal conductivity of a porous medium with coated pore surface.

A corresponding composite sphere element (CSE) is made up by a central sphere with radius r_p filled with phase p , a concentric spherical shell of phase i with thickness $r_i - r_p$, and a second shell of phase b with thickness $r_b - r_i$ (see Figure 9). In our case, phase p represents the pore content (vacuum, air, or something else), phase i is the pore coating layer, and phase b is the bulk material of the porous medium. The CSE is embedded in the effective medium. The volume fraction of the pores, the coating, and the bulk material are denoted by c_p , c_i , and c_b , respectively. Writing

$$r_{pi} = \left(\frac{r_p}{r_i}\right)^3, \quad r_{ib} = \left(\frac{r_i}{r_b}\right)^3, \quad r_{pb} = \left(\frac{r_p}{r_b}\right)^3 \quad (41)$$

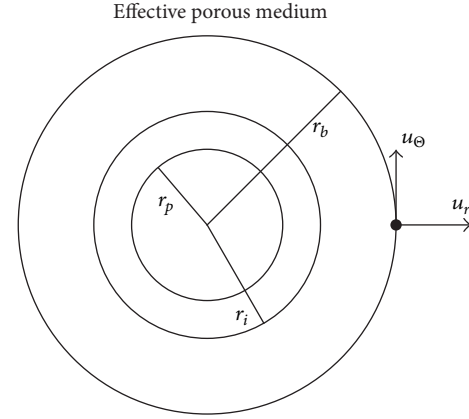


FIGURE 9: Composite sphere element.

the volume fractions of the phases are

$$c_p = r_{pb}^3, \quad c_i = r_{ib}^3 - r_{pb}^3, \quad c_b = 1 - r_{ib}^3. \quad (42)$$

The temperature distribution in the porous medium follows the Laplace equation

$$\Delta T = 0, \quad (43)$$

And the corresponding intensity field is

$$\mathbf{f} = -\nabla T. \quad (44)$$

Heat flux \mathbf{j} and thermal conductivity σ are defined by

$$\mathbf{j} = \sigma \mathbf{f}. \quad (45)$$

According to [70] the solution of the Laplace (43) for the CSE unit embedded in the effective medium is

$$\mathbf{f} = \begin{cases} C_p \sin \Theta \mathbf{u}_\Theta - C_p \cos \Theta \mathbf{u}_r, & 0 \leq r \leq r_p, \\ \left(C_i + \frac{D_i}{r^3}\right) \sin \Theta \mathbf{u}_\Theta \\ + \left(-C_i + 2\frac{D_i}{r^3}\right) \cos \Theta \mathbf{u}_r, & r_p \leq r \leq r_i, \\ \left(C_b + \frac{D_b}{r^3}\right) \sin \Theta \mathbf{u}_\Theta \\ + \left(-C_b + 2\frac{D_b}{r^3}\right) \cos \Theta \mathbf{u}_r, & r_i \leq r \leq r_b, \\ -f_0 \sin \Theta \mathbf{u}_\Theta + f_0 \cos \Theta \mathbf{u}_r, & r_b \leq r. \end{cases} \quad (46)$$

The boundary conditions of the heat flux through the interfaces *pore to coating*, *coating to bulk*, and *bulk to effective medium* require continuity of the radial component \mathbf{j}_r of the heat flux, \mathbf{j} , and of the tangential component \mathbf{f}_Θ of the temperature gradient, $-\mathbf{f}$. Denoting the values of the thermal conductivity of the pore phase, the coating interlayer, the bulk

TABLE 1: Mathematically equivalent properties (according to [5]).

Problem	Potential	Field	Flux	Property
Heat conduction	Temperature T	Temperature gradient $-\nabla T$	Heat flux \mathbf{f}	Heat conductivity σ
Electrical conductivity	Electrical potential	Electric field	Current density	Electrical conductivity
Diffusion	Density	Density gradient	Current density	Diffusion constant
Electrostatics	Electric potential	Electric field	Electric displacement	Dielectric constant
Magnetostatics	Magnetic potential	Magnetic field	Magnetic induction	Permeability

material, and the effective medium by $\sigma_p, \sigma_i, \sigma_b$, and σ^* one obtains a system of linear equations

$$\begin{pmatrix} 1 & -r_{pi} & -1 & 0 & 0 & 0 \\ -\sigma_p & r_{pi}\sigma_i & -2\sigma_i & 0 & 0 & 0 \\ 0 & 1 & 1 & -r_{ib} & -1 & 0 \\ 0 & -\sigma_i & 2\sigma_i & r_{ib}\sigma_b & -2\sigma_b & 0 \\ 0 & 0 & 0 & 1 & 1 & 1 \\ 0 & 0 & 0 & -\sigma_b & 2\sigma_b & -\sigma^* \end{pmatrix} \begin{pmatrix} C_p \\ C_i \\ D_i \\ C_b \\ D_b \\ f_0 \end{pmatrix} = 0. \quad (47)$$

This system has a solution if the determinant of the coefficient matrix vanishes. Solving the resulting equation for σ^* one obtains for the effective thermal conductivity

$$\sigma^* = \sigma_b + \frac{r_{ib}}{(1 - r_{ib})/3\sigma_b - 1/(\sigma_b - \sigma^*)} \quad (48)$$

with

$$\sigma^{\#} = \sigma_i + \frac{r_{pi}}{(1 - r_{pi})/3\sigma_i - 1/(\sigma_i - \sigma_p)}. \quad (49)$$

Quantity $\sigma^{\#}$ can be interpreted as the effective conductivity of a subsystem consisting of spherical pores with conductivity σ_p embedded in a matrix with property σ_i and the corresponding volume fractions.

It is known that a number of physical problems are mathematically equivalent to the formulation of thermal conductivity [5]. Therefore, (43) to (49) apply also to electrical conductivity, static dielectric property, magnetostatics, and diffusion (see Table 1).

The elastic moduli of the considered model can be calculated using either the CSA model [4] or the extended replacement method [71]. The results can be expressed in a similar form as expressions ((48), (49)). Denoting the

effective property of the system by a^* , one can write [48, 68, 69]:

$$\frac{a^*}{a_b} = 1 + \frac{1 - c_b}{\alpha_b^a c_b - a_b / (a_b - a^*)}, \quad (50)$$

$$\frac{a^{\#}}{a_i} = 1 + \frac{1 - c^{\#}}{\alpha_i^a c^{\#} - a_i / (a_i - a_p)}, \quad (51)$$

$$c^{\#} = \frac{c_p}{c_p + c_i}, \quad (52)$$

$$\alpha_m^a = \begin{cases} \frac{1}{3}, & a = \sigma \\ \frac{3K_m}{3K_m + 4G_m}, & a = K \\ \frac{6(K_m + 2G_m)}{5(3K_m + 4G_m)}, & a = G. \end{cases} \quad (53)$$

The symbol σ stands for dielectric constant, thermal conductivity, and related properties, K, G denote elastic bulk and shear modulus for isotropic systems, and index $m = p, i, b$ stands for pore, interphase layer, and bulk phase.

Expressions ((50) to (53)) are rigorous results obtained for geometrical situations as given in the structure models described above. The results for the properties are unique and no uncertainty due to unknown topology of phase distribution occurs. Nevertheless there are relations to the Hashin-Shtrikman bounds for properties of heterogeneous materials [72] which we discuss here for the case of the dielectric constant k . For simplicity, we use a model consisting of a matrix and spherical inclusions. Choosing $c_i = 0$ with $c_p = 1 - c_b$, $a = k$, and $\alpha^k = 1/3$, assuming $k_b < k_p$, and changing the topology of the system by interchanging properties and volume fractions of matrix and inclusions, that is, $k_b \leftrightarrow k_p$, $c_b \leftrightarrow c_p$, one obtains from ((50), (51)) the Hashin-Shtrikman bounds for the effective dielectric constant, k^* , of a two-component composite (see also [5], (2.3))

$$k_b + \frac{k_b c_p}{c_p/3 - k_p / (k_p - k_b)} \leq k^* \leq k_p + \frac{k_p c_b}{c_b/3 - k_b / (k_b - k_p)}. \quad (54)$$

The same procedure can be carried out for the Hashin-Shtrikman bounds for the isotropic elastic moduli (see [4],

Sections 3.2 and 4.1). For a given distribution of phases on pores, interphase layer, and bulk there is no uncertainty of the topology and, consequently, expressions ((50) to (53)) for the properties are unique.

5. Applications

5.1. Fractal-Like Pore Structure. Porous media may have fractal features (see, e.g., [73–75]). We consider here a model for surface fractals which is based on the Boolean model described in Section 3.1. This model is tunable with respect to the fractal dimension of the internal surface, and explicit expression for the geometrical characteristics defined in Section 2 is known [68, 76]. The size distribution of spheres used for the construction of the model is defined by self-similarity rules for the radii r_u and the partial number density ν_u of spheres r_u :

$$r_u = u^s r_1, \quad \nu_u = u^{-t} \nu_1, \quad u_0 \leq u \leq 1, \quad (55)$$

where r_u and ν_u are radius and number density of spheres belonging to the interval $(u-du, u)$. Parameter $\kappa = r_0/r_1 = u_0^s$ describes the ratio of minimum and maximum sphere size. The normalized size distribution $f(r)$ is then given by

$$f(r) = \begin{cases} \frac{\eta \kappa^\eta}{(1-\kappa^\eta) r_1} \left(\frac{r}{r_1}\right)^{-\eta-1}, & r_0 \leq r \leq r_1 \\ 0, & \text{otherwise} \end{cases} \quad (56)$$

$$\eta = \frac{t-1}{s}.$$

Number density of spheres, volume fraction, specific surface area, and correlation function are given by ((14), (15), and (16)) and

$$\nu = \nu_1 \frac{1-\kappa^\eta}{\kappa^\eta \eta s}, \quad (57)$$

$$\nu \bar{V} = \nu_1 \frac{4\pi r_1^3}{3} \frac{1-\kappa^{3-\eta}}{(3-\eta)s}, \quad (58)$$

$$\nu \bar{S} = \nu_1 4\pi r_1^2 \frac{\kappa^{2-\eta} - 1}{(\eta-2)s}, \quad (59)$$

$$\begin{aligned} \nu \gamma(r) &= \frac{3-\eta}{1-\kappa^{3-\eta}} \ln \frac{1}{1-V_V} \\ &\times \left\{ \frac{1-(\rho/r_1)^{3-\eta}}{3-\eta} + \frac{3}{2} \left(\frac{r}{2r_1}\right) \frac{1-(\rho/r_1)^{2-\eta}}{\eta-2} \right. \\ &\quad \left. - \frac{1}{2} \left(\frac{r}{2r_1}\right)^3 \frac{1-(\rho/r_1)^{-\eta}}{\eta} \right\}, \\ &0 \leq r \leq 2r_1, \end{aligned} \quad (60)$$

where

$$\rho = \begin{cases} r_0, & \frac{r}{2} < r_0 \\ \frac{r}{2}, & r_0 \leq \frac{r}{2} \leq r_1. \end{cases} \quad (61)$$

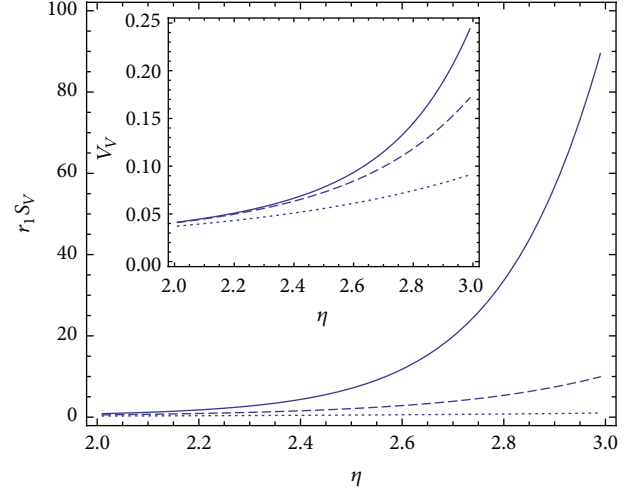


FIGURE 10: Volume fraction (insert) and specific surface area of self-similar Boolean models versus self-similar parameter η ; $r_1 = 1$, $\nu_1 = 0.01$, and $s = 1$; $\kappa = 0.1$ (dotted), 0.01 (dashed), and 0.001 (solid line).

The self-similar model described by ((14), (15), and (16)) and ((58), (59), and (60)) exhibits the properties of a surface fractal if the specific surface area tends to infinity while the volume fraction remains finite for $\kappa \rightarrow 0$. This is the case for

$$2 \leq \eta < 3,$$

$$d_f = \lim_{\epsilon \rightarrow 0} \frac{\ln(P(\mathbf{r} \in S_\epsilon)/\epsilon^3)}{\ln(1/\epsilon)} = \eta \quad (62)$$

is the dimension of the fractal internal surface of the model according to the Minkowski-Bouligand definition [77, 78]. Quantity S_ϵ is the same as in (8). Fractality of a porous medium can be detected by means of small-angle scattering methods [73]. In such cases the limit $r/r_1 \ll 1$ is of interest which determines the behavior of the scattering intensity at large scattering angles. One obtains from ((7), (60))

$$C(r) - V_V^2 \propto \left(\frac{r}{2r_1}\right)^{3-d_f} \quad (63)$$

which is in accordance with [73, 79].

The behavior of the self-similar system is illustrated by Figures 10 and 11. The volume fraction of pores increases with increasing values of the self-similarity parameter η and also with decreasing ratio of radii κ of smallest to largest pores (Figure 10). Of course, V_V keeps limited in the fractal limit $\kappa \rightarrow 0$, where η takes the meaning of the fractal dimension of the internal surface (see expressions ((14), (58)). In the extreme case of $\kappa = 0$ and $d_f \rightarrow 3$ the porosity V_V tends to 1. The specific surface area given by ((15), (59)) is controlled by the term $\kappa^{2-\eta}$. Clearly, S_V tends to infinity for $\kappa \rightarrow 0$ independent of the value $2 < d_f < 3$ of the fractal dimension of the internal surface. The behavior of S_V in the fractal limit appears also applying (9) to (63). Obviously, S_V tends to infinity for each fractal dimension $2 < d_f < 3$ of the

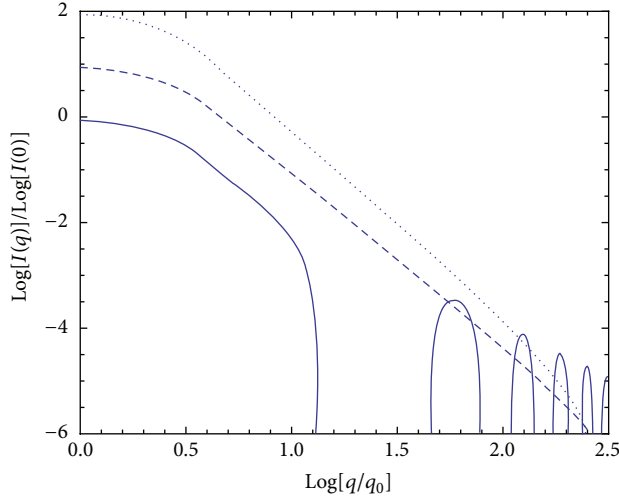


FIGURE 11: Small-angle scattering intensity of self-similar Boolean models; $q_0 = 1$, $r_1 = 1$, $\nu_1 = 0.05$, $s = 1$; $\kappa = 0.001$, and $\eta = 2.1$ (dotted, curve shifted on the ordinate by 2); $\eta = 2.1$ (dashed, shifted by 1); $\kappa = 0.05$, and $\eta = 2.5$ (solid line).

internal surface. Figure 10 illustrates the dependence of S_V on the self-similarity parameter η for different values of κ .

The scattering intensity of the self-similar system can be calculated [11, 68, 78] using

$$I(q) = 4\pi \int_0^\infty r^2 [C(r) - V_V^2] \frac{\sin(qr)}{qr} dr, \quad (64)$$

where q is the absolute value of the scattering vector defined in the usual way [74]. If the size of pores is on the nanometer scale, $I(q)$ is called small-angle scattering intensity. Inserting ((16), (60)) in (64) an explicit expression for the small-angle scattering intensity can be obtained. The limit of small r -values given in (63) becomes apparent in $I(q)$ in the form

$$I(q) \propto q^{6-d_f} \quad (65)$$

in the fractal limit for not too small q -values.

Figure 11 shows scattering intensities of a self-similar system with fractal-like behavior for small κ . The scattering intensity is dominated in the region $\log(q/q_0) < 0.5$ by the largest pores of the system ($r_1 = 1$ in suitable units, e.g., in nanometers). The curve for the system with small range $\kappa = 0.05$ of self-similarity follows approximately expression (65) in the interval $0.5 < \log(q/q_0) < 1$, and for $\log(q) > 1$ the scattering intensity $I(q)$ is determined by the smallest pores of size $r_0 = \kappa r_1$. Systems showing such scattering curves are sometimes called fractal-like. Seriously speaking, the system is self-similar over about one order of magnitude of length scale. The curves for $\kappa = 0.001$ represent systems which are self-similar over 3 orders of magnitude. This is reflected by the linear behavior in the $\log(I(q))$ versus $\log(q/q_0)$ plot for $0.5 < \log(q/q_0) < 2.3$ where the limit (65) applies. Here, the term fractal-like would be justified.

5.2. Optimization of Porous Dielectric Materials. The improvement of silicon based microelectronic devices like microprocessors has been a continuing process over decades [80]. This includes the further development of many components and also the replacement of components by new materials, for example, the replacement of aluminum wires for connecting billions of transistors in a microprocessor circuit by copper wires. This replacement was necessary because the performance of microprocessors is increasingly affected by the on-chip interconnect design and technology. Signal delay caused by the resistor-capacitor (RC) interaction in the system of copper wires and insulating layers becomes more and more important compared to the transistors' signal delay [81, 82]. Additionally, cross-talking and power dissipation worsen due to increasing RC coupling caused by continuous reduction of device dimensions [83, 84]. The introduction of the copper technology was one step to reduce these unfavorable implications of continuous miniaturization. Another one concerns the reduction of the dielectric constant of the insulating layers separating the copper wires. Manufacturable materials with effective dielectric constants of 2.90 to 2.60 are available at the present time; however, feasible solutions with $k < 2.60$ are difficult to obtain [85].

Research is in progress to define dielectric materials with extremely low dielectric constant. Besides dense low- k materials like organosilicate glass and the challenging airgap technology, insulating materials with porosity on the nanometer scale are considered as a promising way to reduce the above problems [85]. Among possible nanoporous insulating materials [86–88] nanoporous silica has the advantage that it can be implemented comparably easily in the current silicon technology.

We consider the following problem: optimize the structure of nanoporous silica in such a way that the dielectric constant k is as low as possible, for example, less than 2 (vacuum: $k = 1$, SiO_2 : $k = 4$), and the Young's modulus E as high as possible, for example, higher than 5 GPa (SiO_2 : $E = 74$ GPa) which would match future technological requirements. Using an interphase model specified by the volume fractions of pores, c_p , and interphase, c_i , and choosing a favorable second material additionally to silica, effective properties can be calculated for the models with ((50), (51), and (52)) and (53) with the corresponding values for α_a^k ; the Young's modulus is given by

$$E = \frac{9KG}{3K + G} \quad (66)$$

for isotropic systems. The properties of the components used for the simulations are quoted in Table 2. Figure 12 shows contour plots of effective property combinations in the plane spanned by c_i and c_p for a model consisting of porous Parylene coated with SiO_2 . Due to the porosity and the low k -value of the bulk material very low values of the dielectric constant can be achieved. However, the Young's modulus is too small for pure porous Parylene. Coating with SiO_2 improves the effective modulus with the result that for $c_i \approx 0.2$ and pore fraction of at least 0.65 excellent values for $k^* < 1.5$ can be combined with reasonable values $E^* \geq 5$ GPa. The required

TABLE 2: Properties of the structural components for models of coated porous ultralow k dielectrics.

Component	K (GPa)	G (GPa)	k
Parylene	4.7	1.0	2
SiO ₂	36.7	31.2	4
Vacuum	0	0	1

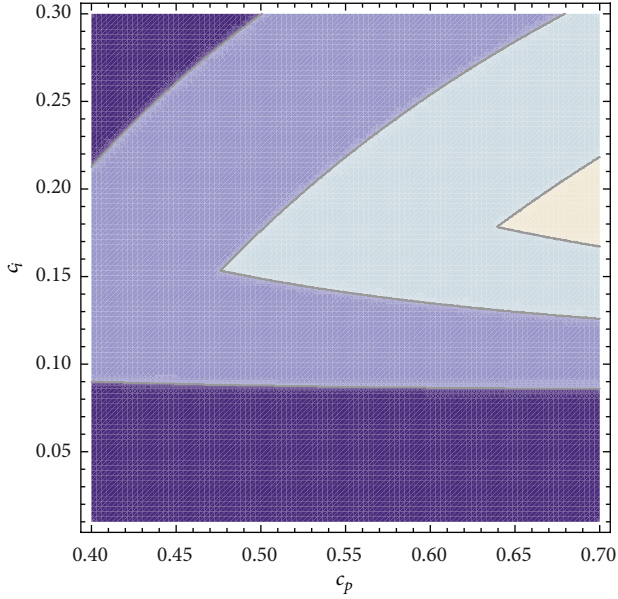


FIGURE 12: Effective property map for porous Parylene coated with SiO₂ versus volume fractions c_p and c_i of pores and coating layer, respectively. Properties of the components are given in Table 2. Regions with $k^* < 1.5, E^* > 5$ GPa (yellow), $k^* < 1.6, E^* > 4$ GPa (light blue), $k^* < 1.7, E^* > 3$ GPa (blue), and $k^* \geq 1.7, E^* \leq 3$ GPa (dark blue).

porosity of at least 0.65 is, however, very high and cannot be achieved with random hard sphere packing models with equal spheres. Instead, the pores must have a polydisperse size distribution to obtain $c_p > 0.65$. The parameters of the required size distribution can be determined using the methods described in Section 3; see also Figure 2.

Starting with porous silica and coating it with Parylene another effective property map appears (Figure 13). Systems with an effective dielectric constant of $k^* < 1.8$ can be achieved at moderate porosity of about 0.60 for values of the effective Young's modulus of not less than 12 GPa, which appears as an excellent combination of dielectric and mechanical properties for the purpose under consideration.

5.3. Simulation of Coating Processes. The previous section showed for a specific case that introducing an interphase layer into a porous system may come out as a useful method to improve effective properties of a porous system. Coating of porous media has been proven to be a successful method to modify their properties in many fields of application. This applies not only to the properties discussed above but also

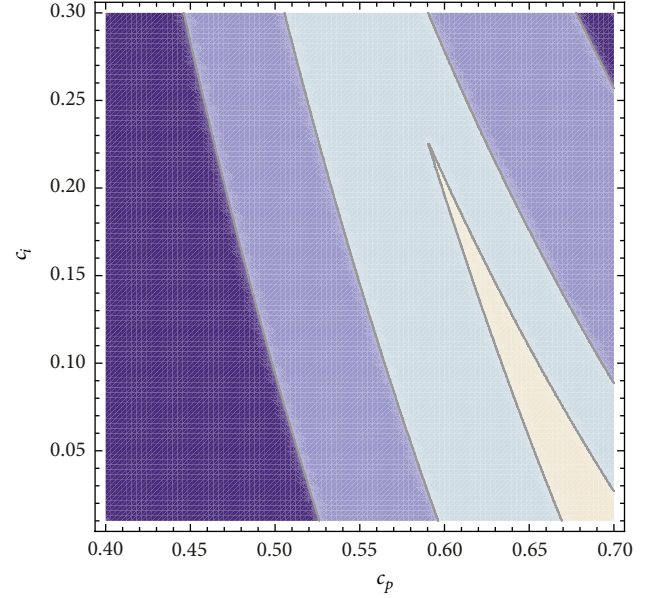


FIGURE 13: Effective property map for porous SiO₂ coated with Parylene versus volume fractions c_p and c_i of pores and coating layer, respectively. Properties of the components are given in Table 2. Regions with $k^* < 1.8, E^* > 12$ GPa (yellow), $k^* < 2.0, E^* > 10$ GPa (light blue), $k^* < 2.2, E^* \leq 5$ GPa (blue), and $k^* \geq 2.2, E^* \leq 5$ GPa (dark blue).

to flow and transport in porous media [7], percolation [89], enzyme immobilization [90, 91], adsorption processes [92–94], and others. Different methods of coating and surface refinement of open-pore materials are known, for example, spray coating [95] and microarc oxidation coating [96] of metallic foams [97], and atomic layer deposition [15, 98–101]. The latter method is of special interest for media which are characterized by open-porosity on the nanometer scale.

We study the growth of a layer on the internal surface of open-pore systems within the framework of the cherry-pit model. Expression (37) for the volume fraction of a coating layer is written in the form

$$c_i = V_V(\lambda_0) - V_V(\lambda_\tau), \quad (67)$$

where τ denotes the coating time. For simplicity we consider a system with narrow pore size distribution. In a continuous coating process the radius r_τ of a given pore reduces according to

$$r(\lambda_\tau) = r_0 - \mu r_h \tau = \frac{r_h}{\lambda_\tau}, \quad r_0 = \frac{r_h}{\lambda_0}. \quad (68)$$

One obtains

$$\lambda_\tau = \frac{\lambda_0}{1 - \lambda_0 \mu \tau}, \quad (69)$$

where μ is the growth rate of layer thickness measured in units of the pit radius of the cherry-pit model. For discontinuous processes like atomic layer deposition, $\mu\tau$ has to be replaced by Δtn , where n is the number of the deposition cycle and

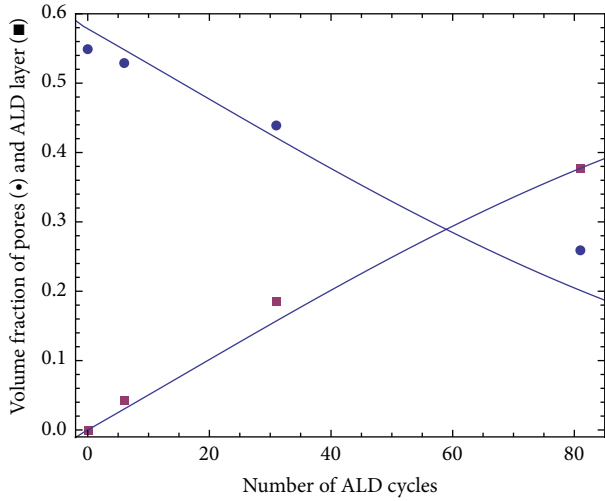


FIGURE 14: Volume fraction of pores (circles) and ALD layer (squares) of Al_2O_3 coated polypropylene. Experimental data points taken from [15]. Curves calculated using formula (36).

TABLE 3: Properties of the structural components used for the atomic layer deposition process.

Component	K (GPa)	G (Gpa)	σ (W/mK)
Polypropylene	6	0.6	0.12
Al_2O_3	165	124	18

Δt is the increment of layer thickness achieved by one cycle measured in units of the pit radius. We apply the present approach to experimental results for atomic layer deposition of Al_2O_3 on porous polypropylene [15]. Figure 14 compares the evolution of the porosity and the volume fraction of the Al_2O_3 layer with the number of deposition cycles. The cycle numbers are corrected for the induction period [15]. The model curves reproduce the trend of the experimental data with an accuracy of about 20%.

The estimated volume fractions can now be used to predict effective properties of the coated material. Using known data (see Table 3) for bulk, K , shear, G , modulus, and the thermal conductivity σ of polypropylene and for Al_2O_3 the effective elastic and thermophysical properties of the coated material are calculated. Figure 15 shows the results for the effective thermal conductivity and the Young's modulus. Both for the Young's modulus and the thermal conductivity the essential increase is achieved within the first 20 deposition cycles. These results supplement the experimental data obtained in [15] by predicting the change of physical properties during the deposition process.

6. Conclusion

There are appropriate theoretical tools for a consistent description of the structure and effective properties of isotropic random porous media. These tools provide improved facilities to develop suitable models for porous materials from experimentally obtained structural parameters and to optimize

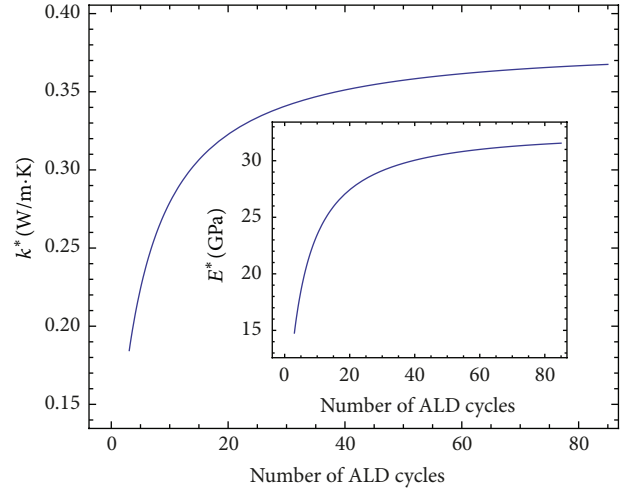


FIGURE 15: Effective thermal conductivity and Young's modulus of Al_2O_3 coated polypropylene versus ALD cycle number.

effective properties by simulating the response of effective properties on structural modification.

Conflict of Interests

The authors declare that there is no conflict of interests regarding the publication of this paper.

References

- [1] J. M. Ziman, *Models of Disorder*, Cambridge University Press, Cambridge, UK, 1979.
- [2] N. E. Cusack, *The Physics of Structurally Disordered Matter*, Adam Hilger, Bristol, UK, 1987.
- [3] D. Weaire, *The Physics of Foam*, Clarendon Press, Oxford, UK, 1999.
- [4] W. Kreher and W. Pompe, *Internal Stresses in Heterogeneous Solids*, Akademie-Verlag, Berlin, Germany, 1999.
- [5] T. C. Choy, *Effective Medium Theory—Principles and Applications*, Clarendon Press, Oxford, UK, 1999.
- [6] S. Torquato, *Random Heterogeneous Materials: Microstructure and Macroscopic Properties*, Springer, New York, NY, USA, 2002.
- [7] M. Sahimi, *Flow and Transport in Porous Media and Fractured Rock: From Classical Methods to Modern Approaches*, Wiley-VCH, Weinheim, Germany, 1995.
- [8] D. Stoyan, W. S. Kendall, and J. Mecke, *Stochastic Geometry and Its Applications*, Akademie-Verlag, Berlin, Germany, 1987.
- [9] D. Stoyan, W. S. Kendall, and J. Mecke, *Stochastic Geometry and Its Applications*, Wiley, Chichester, UK, 2nd edition, 1995.
- [10] S. N. Chiu, D. Stoyan, W. S. Kendall, and J. Mecke, *Stochastic Geometry and Its Applications*, Wiley, Weinheim, Germany, 3rd edition, 2013.
- [11] H. Hermann, *Stochastic Models of Heterogeneous Materials*, Trans Tech, Zurich, Switzerland, 1991.
- [12] K. R. Mecke and D. Stoyan, Eds., *Statistical Physics and Spatial Statistics—The Art of Analyzing and Modeling Spatial Structures and Pattern Formation*, Springer, Berlin, Germany, 2000.

- [13] J. Ohser and F. Mücklich, *3D Images of Materials Structures: Processing and Analysis*, Wiley-VCH, Weinheim, Germany, 2000.
- [14] J. Ohser and K. Schladitz, *3D Images of Materials and Structures: Processing and Analysis*, Wiley-VCH, Weinheim, Germany, 2009.
- [15] S. Y. Jung, A. S. Cavanagh, L. Gevilas et al., "Improved functionality of lithium-ion batteries enabled by atomic layer deposition on the porous microstructure of polymer separators and coating electrodes," *Advanced Energy Materials*, vol. 2, no. 8, pp. 1022–1027, 2012.
- [16] R. Hosemann and S. N. Bagchi, *Direct Analysis of Diffraction by Matter*, North-Holland, Amsterdam, The Netherlands, 1962.
- [17] G. Porod, "Die Röntgenkleinwinkelstreuung von dichtgepackten kolloiden Systemen," *Kolloid-Zeitschrift*, vol. 125, no. 1, pp. 51–57, 1952.
- [18] C. Kittel, *Introduction to Solid State Physics*, John Wiley & Sons, New York, NY, USA, 1996.
- [19] J. D. Bernal and J. Mason, "Packing of spheres: co-ordination of randomly packed spheres," *Nature*, vol. 188, no. 4754, pp. 910–911, 1960.
- [20] G. S. Cargill III, "Structure of metallic alloy glasses," *Solid State Physics*, vol. 30, pp. 227–320, 1975.
- [21] J. L. Finney, "Modelling the structures of amorphous metals and alloys," *Nature*, vol. 266, no. 5600, pp. 309–314, 1977.
- [22] M. R. Hoare, "Packing models and structural specificity," *Journal of Non-Crystalline Solids*, vol. 31, no. 1-2, pp. 157–179, 1978.
- [23] H. L. Löwen, "Fun with hard spheres," in *Statistical Physics and Spatial Statistics—The Art of Analyzing and Modeling Spatial Structures and Pattern Formation*, K. R. Mecke and D. Stoyan, Eds., pp. 295–331, Springer, Berlin, Germany, 2000.
- [24] W. S. Jodrey and E. M. Tory, "Computer simulation of close random packing of equal spheres," *Physical Review A*, vol. 32, no. 4, pp. 2347–2351, 1985.
- [25] J. Moscinski and M. Bargiel, "C-language program for the irregular close packing of hard spheres," *Computer Physics Communications*, vol. 64, no. 1, pp. 183–192, 1991.
- [26] A. Bezrukov, M. Bargiel, and D. Stoyan, "Statistical analysis of simulated random packings of spheres," *Particle & Particle Systems Characterization*, vol. 19, no. 2, pp. 111–118, 2002.
- [27] A. Elsner, *Computer-aided simulation and analysis of random dense packings of spheres [thesis]*, 2009 (German).
- [28] B. Widom and J. S. Rowlinson, "New model for the study of liquid-vapor phase transitions," *The Journal of Chemical Physics*, vol. 52, no. 4, pp. 1670–1684, 1970.
- [29] B. Widom, "Geometrical aspects of the penetrable-sphere model," *The Journal of Chemical Physics*, vol. 54, no. 9, pp. 3950–3957, 1971.
- [30] C. N. Likos, K. R. Mecke, and H. Wagner, "Statistical morphology of random interfaces in microemulsions," *The Journal of Chemical Physics*, vol. 102, no. 23, pp. 9350–9361, 1995.
- [31] K. R. Mecke, "A morphological model for complex fluids," *Journal of Physics Condensed Matter*, vol. 8, no. 47, pp. 9663–9667, 1996.
- [32] F. H. Stillinger, "Phase transitions in the Gaussian core system," *The Journal of Chemical Physics*, vol. 65, no. 10, pp. 3968–3974, 1976.
- [33] C. N. Likos, M. Watzlawek, and H. Löwen, "Freezing and clustering transitions for penetrable spheres," *Physical Review E*, vol. 58, no. 3, pp. 3135–3144, 1998.
- [34] C. N. Likos, A. Lang, M. Watzlawek, and H. Löwen, "Criterion for determining clustering versus reentrant melting behaviour for bounded interaction potentials," *Physical Review E*, vol. 63, no. 3, Article ID 031206, 2001.
- [35] C. N. Likos, B. M. Mladek, D. Gottwald, and G. Kahl, "Why do ultrasoft repulsive particles cluster and crystallize? Analytical results from density-functional theory," *The Journal of Chemical Physics*, vol. 126, no. 22, Article ID 224502, 2007.
- [36] M.-J. Feraud, E. Lomba, and L. L. Lee, "A self-consistent integral equation study of the structure and thermodynamics of the penetrable sphere fluid," *The Journal of Chemical Physics*, vol. 112, no. 2, pp. 810–816, 2000.
- [37] A. Santos and A. Majewsky, "Fluids of spherical molecules with dipolarlike nonuniform adhesion: an analytically solvable anisotropic model," *Physical Review E*, vol. 78, no. 2, Article ID 021201, 2008.
- [38] L. Blum and G. Stell, "Polydisperse systems—I. Scattering function for polydisperse fluids of hard or permeable spheres," *The Journal of Chemical Physics*, vol. 71, no. 1, pp. 42–46, 1979.
- [39] P. A. Rikvold and G. Stell, "Porosity and specific surface for interpenetrable-sphere models of two-phase random media," *The Journal of Chemical Physics*, vol. 82, no. 2, pp. 1014–1020, 1985.
- [40] P. A. Rikvold and G. Stell, "D-dimensional interpenetrable-sphere models of random two-phase media: microstructure and an application to chromatography," *Journal of Colloid and Interface Science*, vol. 108, no. 1, pp. 158–173, 1985.
- [41] S. Torquato, "Bulk properties of two-phase disordered media—I. Cluster expansion for the effective dielectric constant of dispersions of penetrable spheres," *The Journal of Chemical Physics*, vol. 81, no. 11, pp. 5079–5088, 1984.
- [42] S. Torquato, "Bulk properties of two-phase disordered media—II. Effective conductivity of a dilute dispersion of penetrable spheres," *The Journal of Chemical Physics*, vol. 83, no. 9, pp. 4776–4785, 1985.
- [43] S. Torquato, "Bulk properties of two-phase disordered media—III. New bounds on the effective conductivity of dispersions of penetrable spheres," *The Journal of Chemical Physics*, vol. 84, no. 11, pp. 6345–6359, 1986.
- [44] K. Gotoh, M. Nakagawa, M. Furuuchi, and A. Yoshigi, "Pore size distributions in random assemblies of equal spheres," *The Journal of Chemical Physics*, vol. 85, no. 5, pp. 3078–3080, 1986.
- [45] S. B. Lee and S. Torquato, "Porosity for the penetrable-concentric-shell model of two-phase disordered media: computer simulation results," *The Journal of Chemical Physics*, vol. 89, no. 5, pp. 3258–3263, 1988.
- [46] D. Stoyan, A. Wagner, H. Hermann, and A. Elsner, "Statistical characterization of the pore space of random systems of hard spheres," *Journal of Non-Crystalline Solids*, vol. 357, no. 6, pp. 1508–1515, 2011.
- [47] A. Elsner, A. Wagner, T. Aste, H. Hermann, and D. Stoyan, "Specific surface area and volume fraction of the cherry-pit model with packed pits," *The Journal of Physical Chemistry B*, vol. 113, no. 22, pp. 7780–7784, 2009.
- [48] H. Hermann, A. Elsner, and D. Stoyan, "Surface area and volume fraction of random open-pore systems," *Modelling and Simulation in Materials Science and Engineering*, vol. 21, no. 8, Article ID 085005, 2013.
- [49] A. P. Roberts, "Statistical reconstruction of three-dimensional porous media from two-dimensional images," *Physical Review E*, vol. 56, no. 3, pp. 3203–3212, 1997.

- [50] C. L. Y. Yeong and S. Torquato, "Reconstructing random media," *Physical Review E*, vol. 57, no. 1, pp. 495–506, 1998.
- [51] C. L. Y. Yeong and S. Torquato, "Reconstructing random media—II. Three-dimensional media from two-dimensional cuts," *Physical Review E*, vol. 58, no. 1, pp. 224–233, 1998.
- [52] R. Hilfer and C. Manwart, "Permeability and conductivity for reconstruction models of porous media," *Physical Review E*, vol. 64, no. 2, Article ID 021304, 4 pages, 2001.
- [53] P.-E. Øren and S. Bakke, "Process based reconstruction of sandstones and prediction of transport properties," *Transport in Porous Media*, vol. 46, no. 2-3, pp. 311–343, 2002.
- [54] C. H. Arns, M. A. Knackstedt, and K. R. Mecke, "Reconstructing complex materials via effective grain shapes," *Physical Review Letters*, vol. 91, no. 21, Article ID 215506, 4 pages, 2003.
- [55] C. H. Arns, M. A. Knackstedt, and K. R. Mecke, "Boolean reconstructions of complex materials: integral geometric approach," *Physical Review E*, vol. 80, no. 5, Article ID 051303, 17 pages, 2009.
- [56] T. Prill, K. Schladitz, D. Jeulin, M. Faessel, and C. Wieser, "Morphological segmentation of FIB-SEM data of highly porous media," *Journal of Microscopy*, vol. 250, no. 2, pp. 77–87, 2013.
- [57] W. Kreher and W. Pompe, "Field fluctuations in a heterogeneous elastic material—an information theory approach," *Journal of the Mechanics and Physics of Solids*, vol. 33, no. 5, pp. 419–445, 1985.
- [58] D. Jeulin, *Morphologie mathématique et propriétés physiques des agglomérés de minerai de fer et de coke métallurgique [Ph.D. thesis]*, School of Mines, Paris, France, 1979.
- [59] C. H. Arns, M. A. Knackstedt, W. V. Pinczewski, and K. R. Mecke, "Euler-Poincaré characteristics of classes of disordered media," *Physical Review E*, vol. 63, no. 3, Article ID 031112, 13 pages, 2001.
- [60] C. H. Arns, M. A. Knackstedt, and K. R. Mecke, "Characterisation of irregular spatial structures by parallel sets and integral geometric measures," *Colloids and Surfaces A*, vol. 241, no. 1–3, pp. 351–372, 2004.
- [61] H. Hermann and W. Kreher, "Structure, elastic moduli and internal stresses of iron-boron metallic glasses," *Journal of Physics F: Metal Physics*, vol. 18, no. 4, pp. 641–655, 1988.
- [62] M. D. Rintoul and S. Torquato, "Precise determination of the critical threshold and exponents in a three-dimensional continuum percolation model," *Journal of Physics A: Mathematical and General*, vol. 30, no. 16, pp. L585–L592, 1997.
- [63] A. P. Roberts and E. J. Garboczi, "Computation of the linear elastic properties of random porous materials with a wide variety of microstructure," *Proceedings of the Royal Society A*, vol. 458, no. 2021, pp. 1033–1054, 2002.
- [64] K. Mecke and C. H. Arns, "Fluids in porous media: a morphometric approach," *Journal of Physics Condensed Matter*, vol. 17, no. 9, pp. S503–S534, 2005.
- [65] F. Willot and D. Jeulin, hal-00553376, version 1–7, 2011.
- [66] D. Jeulin, "Multi scale random sets: from morphology to effective behaviour," in *Progress in Industrial Mathematics at ECMI 2010*, M. Günther, A. Bartel, M. Brunk, S. Schöps, and M. Striebel, Eds., pp. 381–393, Springer, Berlin, Germany, 2012.
- [67] S. Torquato, "Optimal design of heterogeneous materials," *Annual Review of Materials Research*, vol. 40, pp. 101–129, 2010.
- [68] H. Hermann, "Effective dielectric and elastic properties of nanoporous low- k media," *Modelling and Simulation in Materials Science and Engineering*, vol. 18, no. 5, Article ID 055007, 2010.
- [69] V. Kokotin, H. Hermann, and J. Eckert, "Theoretical approach to local and effective properties of BMG based matrix-inclusion nanocomposites," *Intermetallics*, vol. 30, pp. 40–47, 2012.
- [70] L. D. Landau and E. M. Lifschitz, *Elektrodynamik der Kontinua*, Akademie-Verlag, Berlin, Germany, 1967.
- [71] I. Shen and J. Li, "Effective elastic moduli of composites reinforced by particle or fiber with an inhomogeneous interphase," *International Journal of Solids and Structures*, vol. 40, no. 6, pp. 1393–1409, 2003.
- [72] Z. Hashin, "The elastic moduli of heterogeneous materials," *Journal of Applied Mechanics*, vol. 29, pp. 143–150, 1962.
- [73] P. W. Schmidt, A. Hohn, H. B. Neumann, H. Kaiser, D. Avnir, and J. S. Lin, "Small-angle X-ray scattering study of the fractal morphology of porous silicas," *The Journal of Chemical Physics*, vol. 90, no. 9, pp. 5016–5023, 1989.
- [74] P. W. Schmidt, "Small-angle scattering studies of disordered, porous and fractal systems," *Journal of Applied Crystallography*, vol. 24, pp. 414–435, 1991.
- [75] B. Yu, "Analysis of flow in fractal porous media," *Applied Mechanics Reviews*, vol. 61, no. 5, Article ID 050801, 19 pages, 2008.
- [76] H. Hermann and J. Ohser, "Determination of microstructural parameters of random spatial surface fractals by measuring chord length distributions," *Journal of Microscopy*, vol. 170, no. 1, pp. 87–93, 1993.
- [77] U. Zähle, "Random fractals generated by random cutouts," *Mathematische Nachrichten*, vol. 116, no. 1, pp. 27–52, 1984.
- [78] H. Hermann, "A new random surface fractal for applications in solid state physics," *Physica Status Solidi B*, vol. 163, no. 2, pp. 329–336, 1991.
- [79] H. D. Bale and O. W. Schmidt, "Small-angle X-ray-scattering investigation of submicroscopic porosity with fractal properties," *Physical Review Letters*, vol. 53, no. 6, pp. 596–599, 1984.
- [80] "International Technological Roadmap for Semiconductors," Interconnect. Semiconductor Industry Association, 2007, <http://www.itrs.net/>.
- [81] S. P. Jeng, R. H. Havemann, and M. C. Chang, "Process integration and manufacturability issues for high performance multilevel interconnect," *Materials Research Society Symposium Proceedings*, vol. 337, article 25, 1994.
- [82] S. H. Rhee, M. D. Radwin, J. I. Ng, and D. Erb, "Calculation of effective dielectric constants for advanced interconnect structures with low- k dielectrics," *Applied Physics Letters*, vol. 83, no. 13, pp. 2644–2646, 2003.
- [83] S. Yu, T. K. S. Wong, K. Pita, X. Hu, and V. Ligatchev, "Surface modified silica mesoporous films as a low dielectric constant intermetal dielectric," *Journal of Applied Physics*, vol. 92, no. 6, pp. 3338–3344, 2002.
- [84] M. R. Wang, R. Rusli, M. B. Yu, N. Babu, C. Y. Li, and K. Rakesh, "Low dielectric constant films prepared by plasma-enhanced chemical vapor deposition from trimethylsilane," *Thin Solid Films*, vol. 462–463, pp. 219–222, 2004.
- [85] K. Zagorodniy, D. Chumakov, C. Täschner et al., "Novel carbon-cage-based ultralow- k materials: modeling and first experiments," *IEEE Transactions on Semiconductor Manufacturing*, vol. 21, no. 4, pp. 646–660, 2008.
- [86] J. L. Plawski, W. N. Gill, A. Jain, and S. Rogojevic, "Nanoporous dielectric films: fundamental property relations and microelectronics applications," in *Interlayer Dielectrics for Semiconductor Technology*, S. P. Murarka, M. Eizenberg, and A. K. Sinha, Eds., pp. 261–325, Elsevier, Amsterdam, The Netherlands, 2003.

- [87] K. Zagorodniy, H. Hermann, and M. Taut, "Structure and properties of computer-simulated fullerene-based ultralow- k dielectric materials," *Physical Review B*, vol. 75, no. 24, Article ID 245430, 6 pages, 2007.
- [88] K. Zagorodniy, G. Seifert, and H. Hermann, "Metal-organic frameworks as promising candidates for future ultralow- k dielectrics," *Applied Physics Letters*, vol. 97, no. 25, Article ID 251905, 2010.
- [89] J. Ohser, C. Ferrero, O. Wirjadi, A. Kuznetsova, J. Düll, and A. Rack, "Estimation of the probability of finite percolation in porous microstructures from tomographic images," *International Journal of Materials Research*, vol. 103, no. 2, pp. 184–191, 2012.
- [90] H. Takahashi, B. Li, T. Sasaki, C. Miyazaki, T. Kajino, and S. Inagaki, "Catalytic activity in organic solvents and stability of immobilized enzymes depend on the pore size and surface characteristics of mesoporous silica," *Chemistry of Materials*, vol. 12, no. 11, pp. 3301–3305, 2000.
- [91] J.-K. Kim, J.-K. Park, and H.-K. Kim, "Synthesis and characterization of nanoporous silica support for enzyme immobilization," *Colloids and Surfaces A: Physicochemical and Engineering Aspects*, vol. 241, no. 1–3, pp. 113–117, 2004.
- [92] C. Vega, R. D. Kaminsky, and P. A. Monson, "Adsorption of fluids in disordered porous media from integral equation theory," *The Journal of Chemical Physics*, vol. 99, no. 4, pp. 3003–3013, 1993.
- [93] G. V. Kapustin and J. Ma, "Modeling adsorption-desorption processes in porous media," *Computing in Science & Engineering*, vol. 1, no. 1, pp. 84–91, 2002.
- [94] A. Touzik and H. Hermann, "Theoretical study of hydrogen adsorption on graphitic materials," *Chemical Physics Letters*, vol. 416, no. 1–3, pp. 137–141, 2005.
- [95] M. Maurer, L. Zhao, and E. Lugscheider, "Surface refinement of metal foams," *Advanced Engineering Materials*, vol. 4, no. 10, pp. 791–797, 2002.
- [96] J. Liu, X. Zhu, Z. Huang, S. Yu, and X. Yang, "Characterization and property of microarc oxidation coatings on open-cell aluminum foams," *Journal of Coatings Technology and Research*, vol. 9, no. 3, pp. 357–363, 2012.
- [97] J. Banhart, "Manufacture, characterisation and application of cellular metals and metal foams," *Progress in Materials Science*, vol. 46, no. 6, pp. 559–632, 2001.
- [98] M. Ritala, M. Kemell, M. Lautala, A. Niskanen, M. Leskelä, and S. Lindfors, "Rapid coating of through-porous substrates by atomic layer deposition," *Chemical Vapor Deposition*, vol. 12, no. 11, pp. 655–658, 2006.
- [99] J. W. Elam, G. Xiong, C. Y. Han et al., "Atomic layer deposition for the conformal coating of nanoporous materials," *Journal of Nanomaterials*, vol. 2006, Article ID 64501, 5 pages, 2006.
- [100] J. W. Elam, J. A. Libera, M. J. Pellin, A. V. Zinovev, J. P. Greene, and J. A. Nolen, "Atomic layer deposition of W on nanoporous carbon aerogels," *Applied Physics Letters*, vol. 89, no. 5, Article ID 053124, 3 pages, 2006.
- [101] F. Li, Y. Yang, Y. Fan, W. Xing, and Y. Ang, "Modification of ceramic membranes for pore structure tailoring: the atomic layer deposition route," *Journal of Membrane Science*, vol. 297–298, pp. 17–23, 2012.

Research Article

Mesostructural Design and Manufacturing of Open-Pore Metal Foams by Investment Casting

Alexander Martin Matz,^{1,2} Bettina Stefanie Mocker,² Daniel Wyn Müller,²
Norbert Jost,² and Gunther Eggeler¹

¹ Institute for Materials, Ruhr-University Bochum, Universitätsstraße 150, 44780 Bochum, Germany

² Institute for Materials and Material Technologies, Pforzheim University of Applied Sciences, Tiefenbronner Straße 65, 75175 Pforzheim, Germany

Correspondence should be addressed to Alexander Martin Matz; alexander.matz@ruhr-uni-bochum.de

Received 11 October 2013; Accepted 12 March 2014; Published 15 April 2014

Academic Editor: Thomas Hipke

Copyright © 2014 Alexander Martin Matz et al. This is an open access article distributed under the Creative Commons Attribution License, which permits unrestricted use, distribution, and reproduction in any medium, provided the original work is properly cited.

The present paper describes the manufacturing process of open-pore metal foams by investment casting and the mesostructural/morphological evolution resulting from a new technique of modifying the precursor. By this technique, the precursor is coated with a polymer layer whereby a thickening of the struts occurs. Relative densities in the range of $1.85 \leq \rho_{rel} \leq 25\%$ of open-pore metal foams can be achieved with high accuracy. The samples investigated have pore densities of $\rho_p = 7$ ppi, 10 ppi, and 13 ppi. The relevant processing parameters needed for a homogenous formation of the polymer layer are determined for two different coating materials and the resulting open-pore foam's mesostructure is characterized qualitatively and quantitatively. The alloy used for investment casting open-pore metal foams is AlZn11. The microstructural evolution of these foams is evaluated as a function of the mesostructure. Differences in the microstructure are observed for foams with low and high relative densities and discussed in terms of cooling subsequent to investment casting.

1. Introduction

Open-pore metal foams possess attractive properties due to their highly porous and light weight structure in combination with their base material. Hence, this group of materials is of great interest for different fields of application, such as in the sectors of heat engineering [1, 2], biomedical engineering [3, 4], electrical energy storage [5, 6], or lightweight design [7, 8].

Common processing techniques for manufacturing open-pore metal foams are based on sintering or casting [9, 10]. The method used in this investigation is a modified investment casting process which offers great advantages due to a targeted adaptation/tailoring of the relative density ρ_{rel} , structure of the cells, geometry, and alloy composition for any specific application. The open-pore metal foam also acts as an exact copy of the precursor—whereby also highly complex component geometries are possible—and regular structures and pore-size distributions can be achieved

[11–13]. Typically, a reticulated polymer foam [14] is used as a precursor. In many investigations (cf. [15–17]) these polymer foams are used for the metal foam production in as-received conditions leading to a relative density of $\rho_{rel} = 2 \pm 0.2\%$ for samples in a range of pore densities of $10 \text{ ppi} \leq \rho_p \leq 40 \text{ ppi}$. However, for some applications such a low metallic portion is not adequate and hence the relative density needs to be enhanced. One common method of doing this is by thickening the struts of the polymer foam by dunking it into liquid wax [16, 18–20]. However, this method requires a high level of experience to achieve a homogenous structure in a repetitive accuracy and to avoid blocking of the pores [18, 19]. Furthermore, thickening the struts can just be conducted within narrow confines.

For these reasons an alternative method for a mesostructural design of open-pore metal foams is developed. Using this method any required relative density ρ_{rel} can be achieved through a homogenous thickening of the struts. The

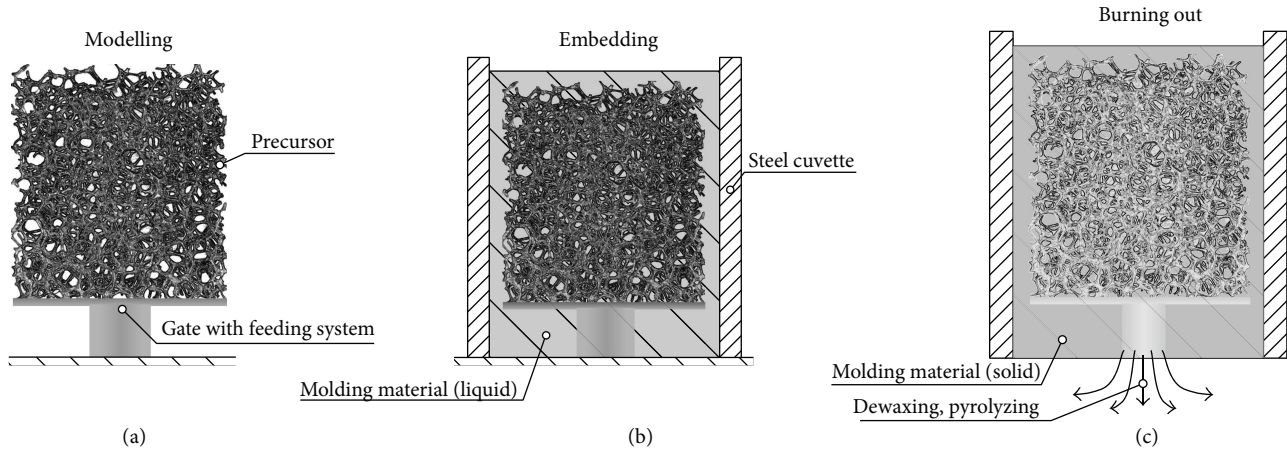


FIGURE 1: Schematic diagram of mold preparation process: (a) modelling in terms of mounting precursor on gate with feeding system, (b) embedding in terms of infiltrating the pattern placed in a steel cuvette by molding material, and (c) burning out in terms of dewaxing the gating system, pyrolyzing the precursor, and hardening the mold.

thickening is a thermal-additive process where the struts of the samples are firstly coated with an adhesive layer, followed secondly by powdering them with polymer granules and thirdly treating the samples above the melting temperature ϑ_M of the polymer granules. In the present study the basics of the modified investment casting process for open-pore metal foams are described briefly. Furthermore, the influence of treatment time t_{th} , treatment temperature ϑ_{th} , diameter of polymer granules d_p , and quantity of treatment runs n_{th} on the open-pore metal foam's mesostructure and its relative density ρ_{rel} is investigated. The microstructural evolution resulting in the investment casted open-pore metal foams is identified.

2. Experimental

2.1. Strut Thickening. The precursors for the modified investment casting process used in this investigation are commercial reticulated open-pore polymer foams (brand name "Regicell") with different pore densities of $\rho_p = 7$ ppi, 10 ppi, and 13 ppi, obtained from Foampartner Reising's Schaumstoffe GmbH in Leverkusen, GER. These as-received samples have a relative density of $\rho_{rel} = 1.95 \pm 0.05\%$ representing the reference condition for this study. The thickening of the open-pore polymer foam's struts as a three-step process is achieved via the following:

- (1) spray coating with a synthetic elastomer based aerosol glue with the brand name "Scotch-Weld Spray 77" from 3M Deutschland GmbH in Neuss, GER as an adhesive layer in an apparatus with a rotating sample holder at standard conditions, resulting in a homogenous distribution of the adhesive on the polymer foam's surface,
- (2) powdering with polymer granules in diameters of $d_p \approx 290 \mu\text{m}$ (PG1) of the type Abcite X1060 from DuPont Polymer Powders Switzerland Sàrl in Bulle,

CH and $d_p \approx 32 \mu\text{m}$ (PG2) of the type FA-7035-SG412 from Ganzlin Beschichtungspulver GmbH in Ganzlin, GER in the abovementioned apparatus at standard conditions, resulting in a homogenous distribution of the polymer granule on the polymer foam's spray coated surface, and

- (3) thermal treatment of the coated samples in a batch furnace at $\vartheta_{th} = 160^\circ\text{C}$ for $t_{th} = 14$ min (PG1) or $t_{th} = 12$ min (PG2), respectively, followed by cooling at standard conditions.

2.2. Mold Preparation. The precursor in its dimensions of $50 \cdot 50 \cdot 20 \text{ mm}^3$ is mounted on a gate with a feeding system made of wax which represents the pattern in its final state (Figure 1). Thereupon this pattern is placed in a steel cuvette. The molding material is a sulfate-bonded investment, supplied by SRS Ltd. in Riddings, GB, which is mixed with water and stirred to form a ceramic slurry which gets evacuated until reaching a residual pressure of $p \approx 25$ mbar to minimize trapped air. After drying for $t = 1$ h at standard conditions, the mold is heated in an incineration furnace in a multistep cycle, shown in Figure 2. The first step at a temperature of $\vartheta = 110^\circ\text{C}$ is conducted to counteract the hygroscopicity. In a second step at $\vartheta = 240^\circ\text{C}$ the gating system is dewaxed and in a third step at $\vartheta = 360^\circ\text{C}$ the polymeric precursor is pyrolyzed. The final drying and hardening of the mold is achieved at $\vartheta = 720^\circ\text{C}$ in a last step followed by furnace cooling. Due to phase transitions and volume changes, these temperatures are kept for at least $t = 1.5$ h and a heating rate of max. $T/t = 6 \text{ K/min}$ is chosen to prevent crack formation.

2.3. Casting. The alloy used for all castings in this study is AlZn11. The starting materials are Al granules with a purity of $\geq 99.99\%$ and Zn pieces with a purity of $\geq 99.995\%$ from Chempur Feinchemikalien und Forschungsbedarf GmbH in Karlsruhe, GER. The metallurgical processing of the open-pore metal foam is carried out by centrifugal casting. Both,

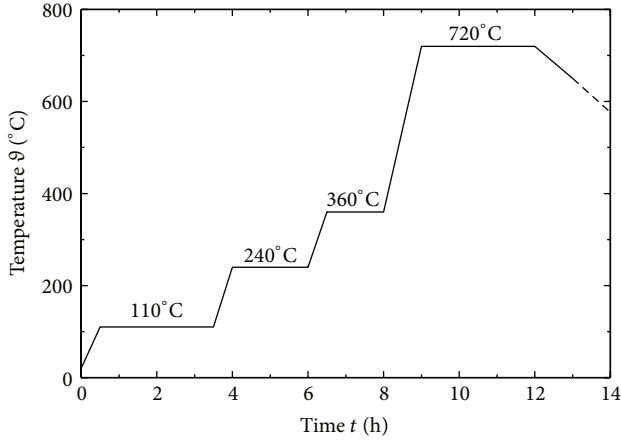


FIGURE 2: Process of dewaxing, pyrolyzing, and mold hardening.

Al and Zn in the mass ratio $m_{\text{Al}}/m_{\text{Zn}} = 89/11$, are placed in a preheated crucible and inductively melted under vacuum. At a temperature of $\vartheta = 750^\circ\text{C}$, the casting is induced and the mold, which was preheated at $\vartheta = 650^\circ\text{C}$ for $t = 5$ h, is infiltrated by the melt. After $t = 3$ min, the mold is removed from the casting machine whereupon it is quenched in water ($\vartheta = 20^\circ\text{C}$). In a last step the samples are cleaned by water jet and Tetranatriummethyldiamintetraacetate ($\text{C}_{10}\text{H}_{12}\text{N}_2\text{Na}_4\text{O}_8$).

2.4. Mesostructural Characterization. The mesostructure of open-pore foams includes the geometric parameters of the foam-like structure such as strut width s_{st} and cell diameter d_c and general foam parameters including pore density ρ_p and relative density ρ_{rel} . To determine the effects of strut thickening on the foam's mesostructure, the digital microscope "VHX-500FD" from Keyence NV/SA in Mechelen, BEL, is used. The conducted investigations are focused on the degree of wetting of the struts by the polymer layer and the interaction of successively added polymer granules, which is analyzed qualitatively. Furthermore, quantitative correlations of polymer granules diameter d_p , strut width s_{st} , and relative density ρ_{rel} are deduced. The relative density, which is defined as

$$\rho_{\text{rel}} = \frac{m_f}{m_s}, \quad (1)$$

the ratio of the foam's mass m_f and the mass of a solid body m_s with the same base material in identical outer dimensions, is governed by weighing the open-pore AlZn11 foam sample with a microbalance (type "AB104" from Mettler-Toledo GmbH in Gießen, GER).

2.5. Microstructural Characterization. To evaluate the influence of the relative density ρ_{rel} on the microstructural evolution of the open-pore AlZn11 foams, microscopical studies are carried out. Therefore, the metal foam samples are partitioned at a distance of $s = 25$ mm to the deadhead by a wet disc grinder. The single sample pieces are embedded in a cold polymerizing plastic (Scandiplex in addition to Varioplex from Scan-Dia Hans-P. Tempelmann GmbH &

Co.KG in Hagen, GER) for further mechanical sample preparation. This is carried out by an automatic grinding/polishing machine (TegraPol-21 from Struers GmbH, GER) in two main steps, namely, wet grinding and diamond polishing as well as chemic-mechanical polishing, as described in [21] in detail. Subsequent to these preliminary steps, electrolytic etching according to Barker is applied (cf. [22]). The microscopical studies of the prepared samples are obtained by a light-optical microscope (DMI 500 M from Leica GmbH, GER) at amplifications of $V = 100 : 1$ in polarized light for evaluating the microstructural morphology.

3. Results and Discussion

In the following, the results of the experimental investigations are pointed out. The processing quality is examined to determine the optimum processing parameters for strut thickening and the mesostructural evolution is characterized by quantifying mesostructural parameters. Moreover, the microstructural evolution in consequence of the varied mesostructure is evaluated for the investment casted foam samples.

3.1. Processing Quality. The key factors for the mesostructural design of open-pore metal foams are the processing parameters of the thermal-additive method for thickening the struts. Particularly temperature ϑ_{th} and time t_{th} of thermal treatment affect the quality of the precursor considerably.

As basic conditions for identifying the optimum thermal treatment temperature ϑ_{th} , the chosen temperature needs to exceed the melting temperature $\vartheta_{\text{th}} > \vartheta_M$ of the polymer granules or coating material, respectively, and needs to be below the temperature where the skeletal structure of the polymer foam collapses, $\vartheta_{\text{th}} < \vartheta_c$. According to manufacturer's data and DSC measurements the relevant temperatures for both polymer granules ϑ_M and the polymer foam ϑ_c are determined. The melting temperature is $\vartheta_M \approx 93^\circ\text{C}$ for PG1 and $\vartheta_M \approx 95^\circ\text{C}$ for PG2. The foam proves to be inherently stable until reaching a temperature of $\vartheta_c \approx 255^\circ\text{C}$.

In a series of experiments, thermal treatment in a temperature range of $120^\circ\text{C} \leq \vartheta_{\text{th}} \leq 200^\circ\text{C}$ was conducted. The results show at $\vartheta_{\text{th}} \leq 155^\circ\text{C}$ that the desired effect of strut thickening can be achieved. However, the process needs up to half an hour to be finished. At $\vartheta_{\text{th}} \geq 165^\circ\text{C}$, the process can be accelerated which is yet coupled with the negative side effect of mass stratification of the polymer layer due to gravitation and a nonhomogenous relative density within the foam, respectively. The best results are determined to be at $\vartheta_{\text{th}} = 160^\circ\text{C}$ for PG1 and PG2.

The required duration of the thermal treatment is investigated in another series of experiments. For this purpose several polymer foam samples are prepared using the first and second process step mentioned in Section 2.1 and thermal treatment at $\vartheta_{\text{th}} = 160^\circ\text{C}$ in a time range of $4 \text{ min} \leq t_{\text{th}} \leq 14 \text{ min}$ is applied, whereby all minute samples are taken and qualitatively analyzed by the digital microscope. The evolution of strut thickening is shown in Figure 3 which demonstrates the formation of a polymer layer

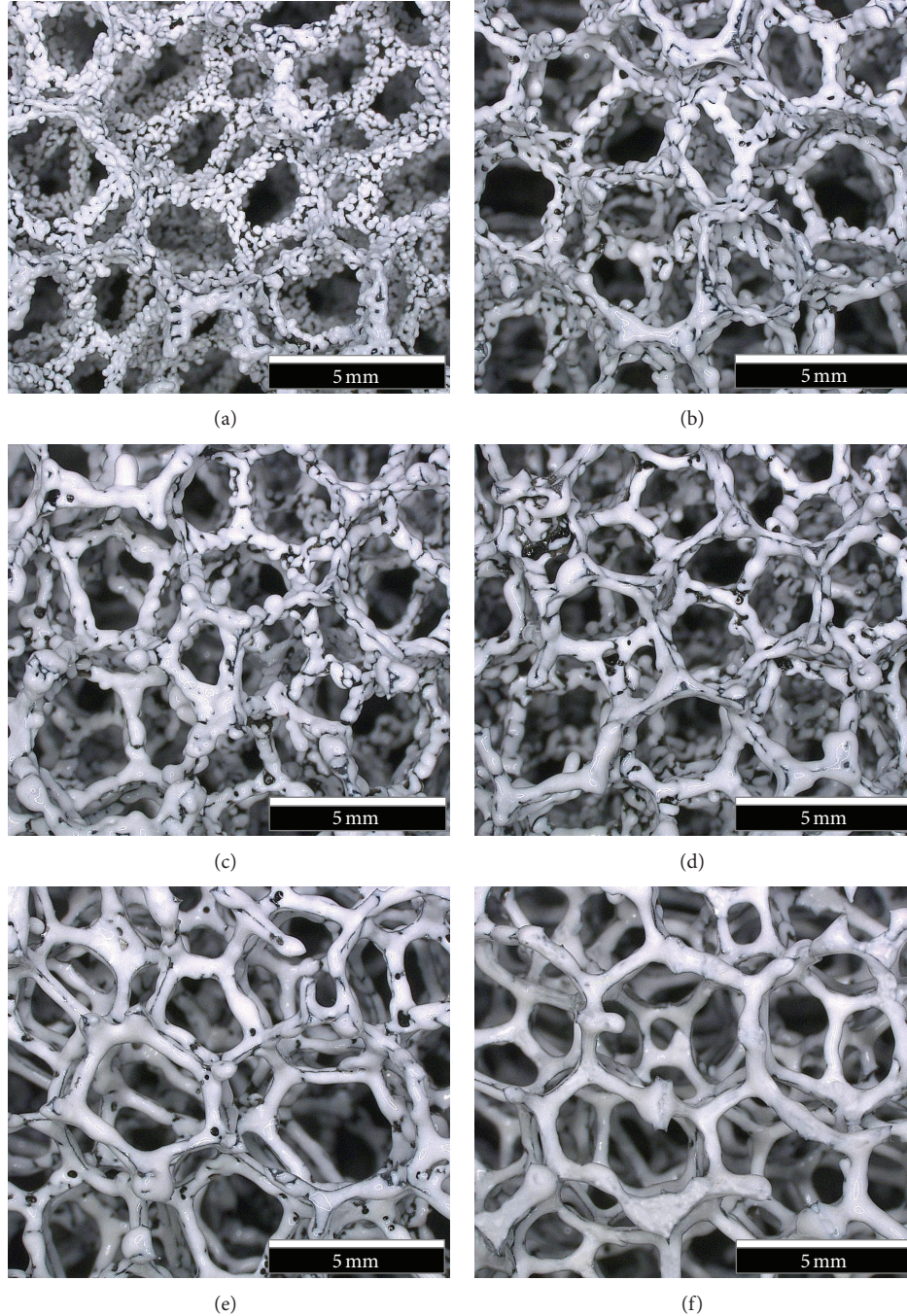


FIGURE 3: Evolution of strut thickening by PG1 at $\vartheta_{th} = 160^\circ\text{C}$ after thermal treatment of (a) $t_{th} = 4$ min, (b) $t_{th} = 6$ min, (c) $t_{th} = 8$ min, (d) $t_{th} = 10$ min, (e) $t_{th} = 12$ min, and (f) $t_{th} = 14$ min using the example of a polymer foam with a pore density of $\rho_p = 10$ ppi.

by agglomeration of the single powder granules as a function of time leading to the result of a homogenous layer after $t_{th} = 14$ min for PG1. Using PG2, a homogenous layer is formed after $t_{th} = 12$ min.

3.2. Mesostructural Evolution. To quantify the mesostructural evolution aroused by the thermal-additive process for strut thickening, all the polymer foam samples are characterized in consideration of the overall mesostructural key

parameter: the relative density ρ_{rel} . It can be observed that ρ_{rel} is in a linear relationship as a function of the quantity of thermal treatment runs n_{th} , as shown in Figure 4. By comparing the pore densities ρ_p of the foam samples, it can be seen that the increase in relative density $\Delta\rho_{rel}$ with each treatment run n_{th} rises by a higher pore density ρ_p or a smaller cell diameter d_c , respectively. An increase of pore density by $\Delta\rho_p = 3$ ppi leads to an approx. 0.325% higher relative density per treatment $\Delta\rho_{rel}/n_{th}$.

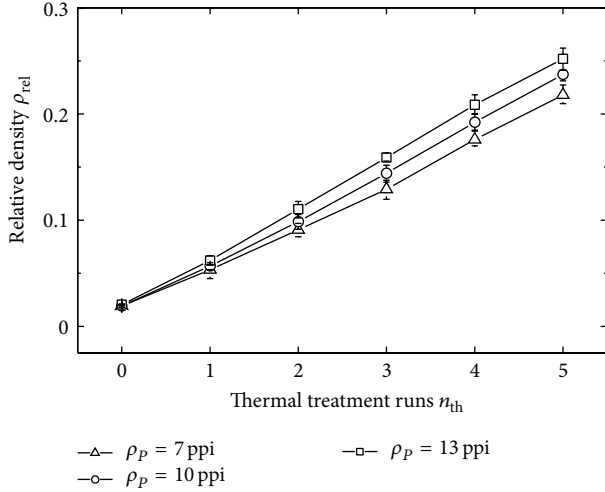


FIGURE 4: Relative density ρ_{rel} as a function of the quantity of thermal treatment runs n_{th} of strut thickened (by PG1) polymer foams with pore densities of $\rho_P = 7$ ppi, 10 ppi, and 13 ppi.

This can be explained by considering the specific surface area of the foam which is available for coating by the polymer powder. Using the example of a simple expression for the specific surface area

$$\xi_f = \frac{c_1}{d_c}, \quad (2)$$

(see [23, 24]) with c_1 as a constant and d_c as the cell diameter and the relation between the relative density and cell diameter

$$d_c = \frac{c_2}{\rho_P}, \quad (3)$$

with c_2 as another constant and inserting (2) in (3) leads to the relation

$$\xi_f \propto \rho_P, \quad (4)$$

between the specific surface area and pore density with the consequence of a higher relative density by increasing the pore density.

As another mesostructural parameter, the strut width s_{st} is characterized by measuring the distance between the outer edges of a single strut, as the example depicted by Inayat et al. [23]. In each sample batch with identical pore density ρ_P and identical quantity of thermal treatment runs n_{th} , at least 150 single struts are measured to achieve a representative mean value, since the mesostructural parameters, such as the strut width, are normally distributed [23]. For a sample batch with $\rho_P = 10$ ppi, which was treated by $n_{th} = 2$ runs with PG1 (resulting in a relative density of $\rho_{rel} = 9.86\%$), the strut width distribution is shown in Figure 5. The mean value of the strut width is $s_{st} = 0.834$ mm and the standard deviation amounts to $\sigma_{st} = 0.037$ mm for this foam. The corresponding strut widths resulting for the other samples coated by PG1 are listed in Table 1 and the ones coated by PG2 are listed in Table 2.

The increase in strut width s_{st} shows, similarly to the relative density ρ_{rel} , that it is in a linear conjunction with the

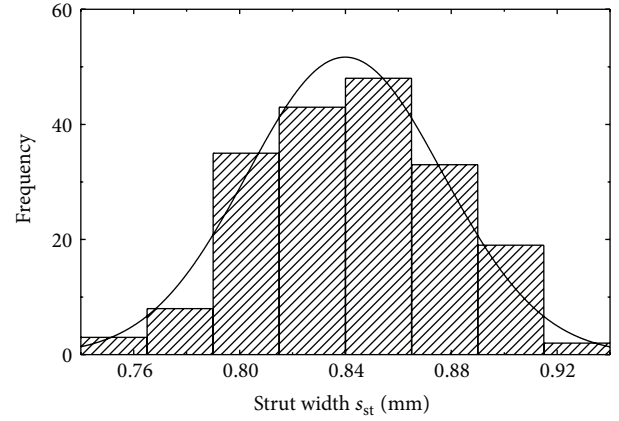


FIGURE 5: Strut width distribution of open-pore foams with a pore density of $\rho_P = 10$ ppi and a relative density of $\rho_{rel} = 9.86\%$.

TABLE 1: Mesostructural parameters of strut thickened polymer foams by PG1.

Pore density ρ_P (ppi)	Quantity of thermal treatment runs n_{th}	Relative density ρ_{rel}	strut width s_{st} (mm)
7	0	0.01922	0.362
7	1	0.05335	0.595
7	2	0.09088	0.849
7	3	0.12906	1.190
7	4	0.17593	1.536
7	5	0.21794	1.820
10	0	0.01918	0.322
10	1	0.05694	0.541
10	2	0.09857	0.834
10	3	0.14421	1.141
10	4	0.19211	1.423
10	5	0.23721	1.797
13	0	0.02060	0.278
13	1	0.06205	0.531
13	2	0.11053	0.796
13	3	0.15899	1.011
13	4	0.20870	1.383
13	5	0.25196	1.706

quantity of thermal treatment runs n_{th} and can be expressed by

$$s_{st,x} \approx d_p \cdot n_{th} + s_{st,0} \quad (5)$$

in which the strut width resulting for any thermal treatment run $s_{st,x}$ increases by the product of the polymer granule's particle diameter d_p and the quantity of thermal treatment runs n_{th} . However, this expression is, in this investigation, only valid for the polymer granule PG1. For the other polymer granule, PG2, the function

$$s_{st,x} \approx \begin{cases} s_{st,0} & n_{th} \leq 2 \\ d_p \cdot n_{th} + s_{st,0} & n_{th} > 2 \end{cases} \quad (6)$$

TABLE 2: Mesostructural parameters of strut thickened polymer foams by PG2.

Pore density ρ_p (ppi)	Quantity of thermal treatment runs n_{th}	Relative density ρ_{rel}	strut width s_{st} (mm)
10	0	0.01918	0.322
10	1	0.02296	0.320
10	2	0.02803	0.325
10	3	0.03210	0.360
10	4	0.03592	0.391
10	5	0.04162	0.420
10	6	0.04510	0.438
10	7	0.04860	0.486
10	8	0.05361	0.507
10	9	0.05921	0.554
10	10	0.06412	0.587

results. This can be justified by the small particle diameter d_p of PG2 (compared to PG1) which forms just a thin polymer layer on the foam's surface in conjunction with the fact that the polymer foam in reference conditions or untreated conditions ($n_{th} = 0$), respectively, exhibits a strut cross section which can be described by a concaved equilateral triangle (Plateau border). Treating the polymer foam by $n_{th} = 1$, its strut cross sections result in an equilateral triangle (Figure 6(a)) and by $n_{th} = 2$ the strut cross sections become shaped as a convex equilateral triangle (Figure 6(b)). In all three conditions, $n_{th} = 0, 1$, and 2 , the outer tips of the plateau border remain as the outer edges by applying the above named method for measuring, resulting in an identical strut width s_{st} . In comparison, a strut of a polymer foam treated by $n_{th} = 3$ is shown in Figure 6(c) at which the strut cross section emerges in a circular-like shape.

Furthermore, it can be deduced from Table 1 that a lower pore density ρ_p leads to a higher strut width s_{st} for each treatment run. This fact results due to the already higher strut width s_{st} of low-pore density foams in untreated or as-received conditions as the consequence of a lower amount of struts in total by an approx. identical relative density ρ_{rel} .

3.3. Microstructural Evolution. The evaluation of the microstructural evolution as a result of the varied mesostructural parameters is investigated for the open-pore AlZn11 foams with a pore density of $\rho_p = 10$ ppi. The sample illustrated in Figure 7(a) represents the reference conditions and is hence not strut thickened ($n_{th} = 0$). The ones shown in Figures 7(b) and 7(c) are strut thickened by a quantity of thermal treatment runs $n_{th} = 3$ and $n_{th} = 5$ with PG1. The increase in strut width with each treatment run $\Delta s_{st}/n_{th}$ can be seen clearly through these macroscopic photographs.

Sample preparation and metallographic analysis are applied as mentioned in Section 2.5 whereby the investigated sections of the foam represent a strut orientated parallel to the sample plane. The micrograph illustrated in Figure 8(a) shows a strut in untreated conditions ($n_{th} = 0$) with

two comparatively large grains. In contrast, in the investigated sections of the samples strut thickened with PG1 by $n_{th} = 5$ (Figure 8(c)), a dominant dendritic microstructure with small grains is visible. The samples treated by $n_{th} = 3$ (Figure 8(b)) partly exhibit a distinctive dendritic microstructure and there are partial zones at which no casting structure is evident.

These differences in microstructure can be explained by the fact that after solidification in the mold, the cooling rate is higher in foam samples with a higher relative density since a higher volume fraction of AlZn11 is existent and more heat can be dissipated due to the high thermal conductivity λ of an Al alloy. In contrast, the thermal conductivity of the plaster is much smaller but its heat capacity c_p is much higher which leads to a lower heat dissipation in foams with small relative densities ρ_{rel} .

4. Summary and Conclusion

In the present study, a new method of thickening the struts is proposed to achieve defined relative densities of investment-cast open-pore metal foams in the range of $1.85\% \leq \rho_{rel} \leq 25\%$. This method is a three-step process, where the open-pore polymer foams need to get spray coated by an adhesive layer, afterwards powdered with polymer granules, and thermally treated to achieve a precursor in its required relative density with homogenous struts. Subsequently, the common procedure of investment casting has to be applied.

For evaluating the processing quality of the strut thickening process, two polymer powders with different particle diameters $d_p \approx 290 \mu\text{m}$ (PG1) and $d_p \approx 32 \mu\text{m}$ (PG2) are investigated. By varying temperature ϑ_{th} and time t_{th} of thermal treatment, the optimum parameters for a homogenous mesostructure of the foam and for a uniform formation of the polymer layer are identified. The processing temperature is determined to be at $\vartheta_{th} = 160^\circ\text{C}$ for both powder types. The formation of the polymer layer occurring by agglomeration of the powder granules is achieved after $t_{th} = 14$ min for PG1 and $t_{th} = 12$ min for PG2.

With respect to the mesostructural parameters resulting from this method, the relative density ρ_{rel} and strut widths s_{st} as a function of the quantity of thermal treatment runs n_{th} are determined for open-pore foams with pore densities of $\rho_p = 7$ ppi, 10 ppi, and 13 ppi. A linear relationship between ρ_{rel} and n_{th} is observed whereby the increase of ρ_{rel} with each treatment run is more dominant as the pore density ρ_p is higher which is a consequence of the foam's specific surface area ξ_f . Furthermore, the strut widths s_{st} also show a linear dependency on the quantity of thermal treatment runs n_{th} in compliance with the requirement of a circular-like shaped strut cross section which can be ascribed by the product of the polymer powder's particle diameters ρ_p and quantity of thermal treatment runs n_{th} in addition to the strut width of the foam in untreated conditions $s_{st,0}$.

The microstructural evaluation indicates differences in the microstructure of the open-pore AlZn11 foams as a function of the mesostructural parameters. A dominant dendritic structure in foams with high relative densities is

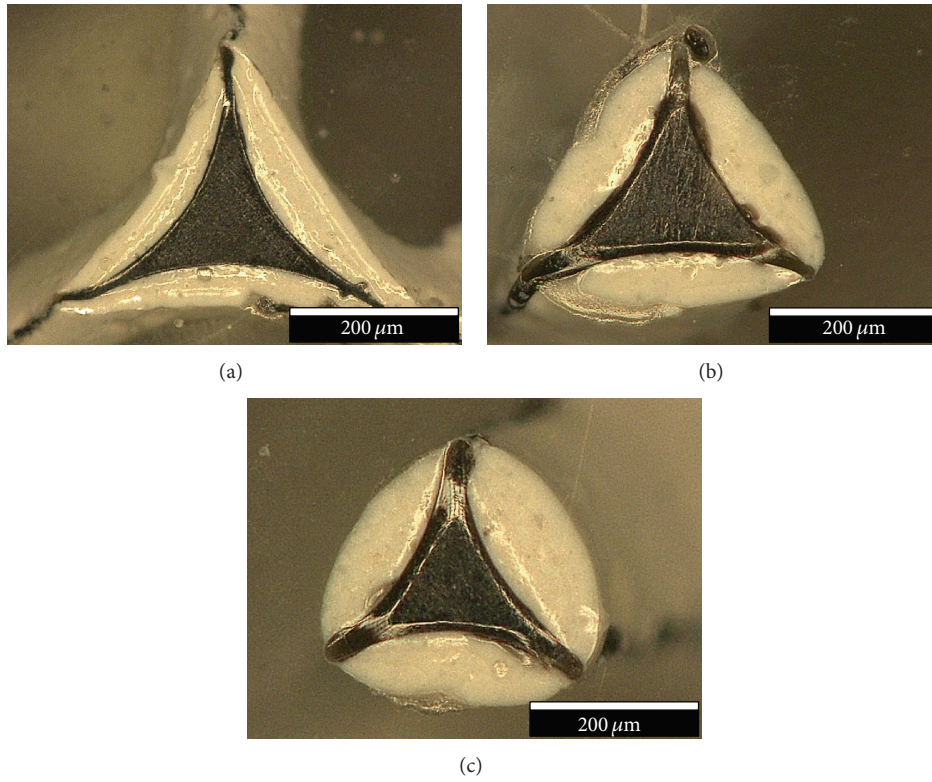


FIGURE 6: Cross section of a single strut of a PG2-treated polymer foam with a pore density of $\rho_p = 10$ ppi by a quantity of thermal treatment runs of (a) $n_{th} = 1$, (b) $n_{th} = 2$, and (c) $n_{th} = 3$.

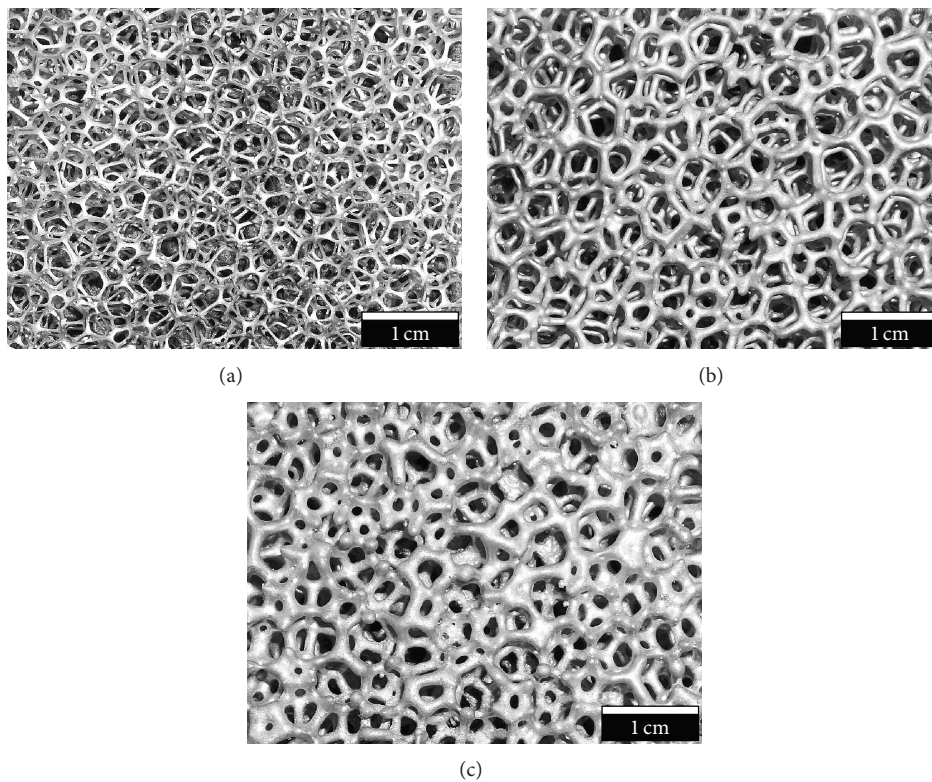


FIGURE 7: Open-pore AlZn11 foams with a pore density of $\rho_p = 10$ ppi (a) in untreated conditions ($n_{th} = 0$), (b) strut thickened with PG1 by $n_{th} = 3$, and (c) strut thickened with PG1 by $n_{th} = 5$.

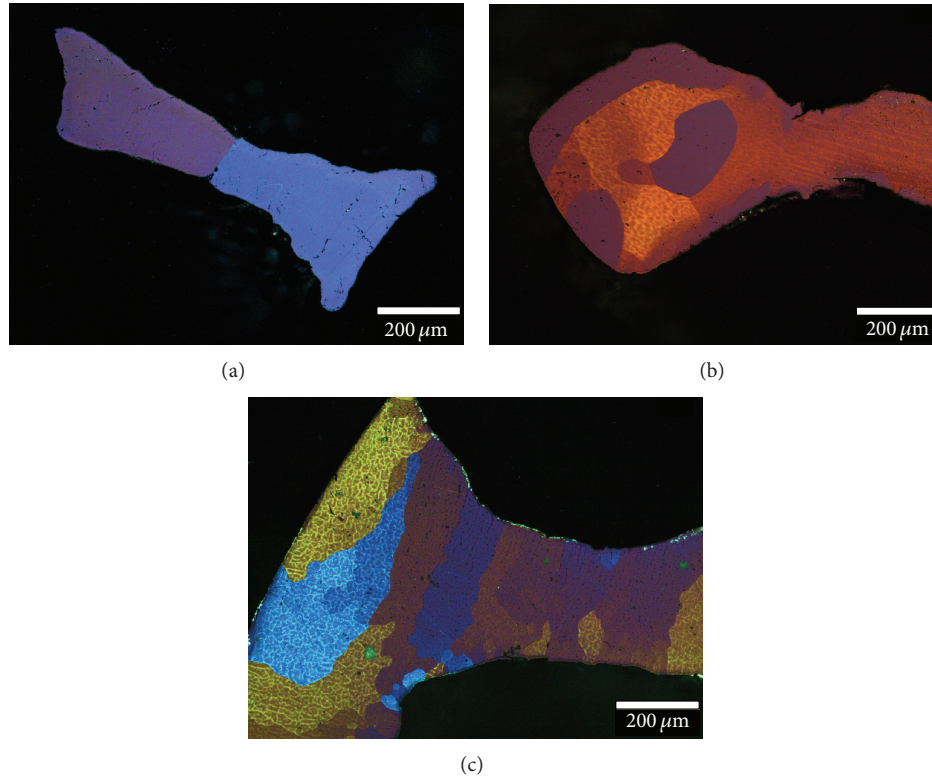


FIGURE 8: Microstructure of open-pore AlZn11 foams (a) in untreated conditions ($n_{th} = 0$), (b) with PGI strut thickened by $n_{th} = 3$, and (c) with PGI strut thickened by $n_{th} = 5$.

observed whereas no indications for that are evident in foams with low relative densities. The reason might be a higher cooling rate resulting from the higher metal portion with its high thermal conductivity in foams with high relative densities.

Conflict of Interests

The authors declare that there is no conflict of interests regarding the publication of this paper.

Acknowledgments

The authors gratefully acknowledge the European Union/European Fund for Regional Development and the federal state Baden-Württemberg for financial support. Moreover, they wish to thank Foampartner Reisinger Kunststoffe GmbH, especially H.-J. Stolz, DuPont Polymer Powders Switzerland Sàrl, and Ganzlin Beschichtungspulver GmbH for material support. The authors would also like to express their gratitude to E. Drotleff, R. Burkart, and J. Aktas for assistance concerning experimental tasks.

References

- [1] X.-H. Han, Q. Wang, Y.-G. Park, C. T'Joel, A. Sommers, and A. Jacobi, "A review of metal foam and metal matrix composites for heat exchangers and heat sinks," *Heat Transfer Engineering*, vol. 33, no. 12, pp. 1–20, 2012.
- [2] C. Y. Zhao, "Review on thermal transport in high porosity cellular metal foams with open cells," *International Journal of Heat and Mass Transfer*, vol. 55, no. 13-14, pp. 3618–3632, 2012.
- [3] Y. Er and E. Unsaldi, "The production of nickel-chromium-molybdenum alloy with open pore structure as an implant and the investigation of its biocompatibility in vivo," *Advances in Materials Science and Engineering*, vol. 2013, Article ID 568479, 7 pages, 2013.
- [4] D. W. Müller, A. M. Matz, and N. Jost, "Casting open porous Ti foam suitable for medical applications," *Bioinspired, Biomimetic and Nanobiomaterials*, vol. 2, no. 2, pp. 76–83, 2013.
- [5] P. S. Liu, T. F. Li, and C. Fu, "Relationship between electrical resistivity and porosity for porous metals," *Materials Science and Engineering A*, vol. 268, no. 1-2, pp. 208–215, 1999.
- [6] Q.-X. Low, W. Huang, X.-Z. Fu et al., "Copper coated nickel foam as current collector for H₂S-containing syngas solid oxide fuel cells," *Applied Surface Science*, vol. 258, no. 3, pp. 1014–1020, 2011.
- [7] M. F. Ashby, "The mechanical properties of cellular solids," *Metallurgical Transactions A*, vol. 14, no. 9, pp. 1755–1769, 1983.
- [8] H. Kanahashi, T. Mukai, Y. Yamada et al., "Experimental study for the improvement of crashworthiness in AZ91 magnesium foam controlling its microstructure," *Materials Science and Engineering A*, vol. 308, no. 1-2, pp. 283–287, 2001.
- [9] G. J. Davies and S. Zhen, "Metallic foams: their production, properties and applications," *Journal of Materials Science*, vol. 18, no. 7, pp. 1899–1911, 1983.
- [10] H. N. G. Wadley, "Cellular metals manufacturing," *Advanced Engineering Materials*, vol. 4, no. 10, pp. 726–733, 2002.

- [11] S. F. Fischer, M. Thielen, R. R. Loprang et al., "Pummelos as concept generators for biomimetically inspired low weight structures with excellent damping properties," *Advanced Engineering Materials*, vol. 12, no. 12, pp. B658–B663, 2010.
- [12] A. Jung, *Offenporige, nanobeschichtete hybrid-metallschäume: herstellung und mechanische eigenschaften [Ph.D. dissertation]*, Saarland University, Saarbrücken, Germany, 2011, (German).
- [13] U. Krupp, A. Ohmdorf, T. Guillén et al., "Isothermal and thermomechanical fatigue behavior of open-cell metal sponges," *Advanced Engineering Materials*, vol. 8, no. 9, pp. 821–827, 2006.
- [14] R. A. Volz, "Reticulated polyurethane foams and process for their production," US3171820, 1965.
- [15] S. F. Fischer, P. Schüler, C. Fleck, and A. Bühring-Polaczek, "Influence of the casting and mould temperatures on the (micro)structure and compression behaviour of investment-cast open-pore aluminium foams," *Acta Materialia*, vol. 61, no. 14, pp. 5152–5161, 2013.
- [16] L. C. Wang and F. Wang, "Preparation of the open pore aluminum foams using investment casting process," *Acta Metallurgica Sinica (English Letters)*, vol. 14, no. 1, pp. 27–32, 2001.
- [17] Y. Yamada, K. Shimojima, Y. Sakaguchi et al., "Processing of an open-cellular AZ91 magnesium alloy with a low density of 0.05 g/cm³," *Journal of Materials Science Letters*, vol. 18, no. 18, pp. 1477–1480, 1999.
- [18] M. Grohn, *Feingegossene metallschwämme als preform zur schmelzflüssigen infiltration [Ph.D. dissertation]*, Shaker, Aachen, Germany, 2005, (German).
- [19] C. A. Hintz, *Präzisionsgegossene metallische schwammstrukturen [Ph.D. dissertation]*, Shaker, Aachen, Germany, 2003, (German).
- [20] L. Wang, H. Li, F. Wang, and J. Ren, "Preparation of open-cell metal foams by investment cast," *China Foundry*, vol. 2, no. 1, pp. 56–59, 2005.
- [21] B. S. Mocker, U. Christian, A. M. Matz, N. Jost, and C. Siegle, "Mikrostrukturelle charakterisierung im feingussverfahren hergestellter offenporiger metallschäume aus aluminium-silizium-legierungen," *Fortschritte in der Metallographie*, vol. 45, pp. 279–284, 2013 (German).
- [22] G. Petzow, *Metallographic Etching: Techniques for Metallography, Ceramography, Plastography*, ASM International, Materials Park, Ohio, USA, 2nd edition, 2001.
- [23] A. Inayat, H. Freund, T. Zeiser, and W. Schwieger, "Determining the specific surface area of ceramic foams: the tetrakaidehedra model revisited," *Chemical Engineering Science*, vol. 66, no. 6, pp. 1179–1188, 2011.
- [24] J. Vicente, F. Topin, and J.-V. Daurelle, "Open celled material structural properties measurement: from morphology to transport properties," *Materials Transactions*, vol. 47, no. 9, pp. 2195–2202, 2006.

Research Article

The Role of Foaming Agent and Processing Route in Mechanical Performance of Fabricated Aluminum Foams

Alexandra Byakova,¹ Iegor Kartuzov,¹ Svyatoslav Gnyloskurenko,² and Takashi Nakamura³

¹ Institute for Problems of Materials Science, National Academy of Sciences of Ukraine, Kiev 03142, Ukraine

² Physical-Technological Institute of Metals and Alloys, National Academy of Sciences of Ukraine, Kiev 03142, Ukraine

³ Institute of Multidisciplinary Research for Advanced Materials, Tohoku University, Sendai 980-8577, Japan

Correspondence should be addressed to Svyatoslav Gnyloskurenko; slava.vgn@gmail.com

Received 18 December 2013; Revised 4 March 2014; Accepted 5 March 2014; Published 31 March 2014

Academic Editor: Alexander Tsouknidas

Copyright © 2014 Alexandra Byakova et al. This is an open access article distributed under the Creative Commons Attribution License, which permits unrestricted use, distribution, and reproduction in any medium, provided the original work is properly cited.

The results of this study highlight the role of foaming agent and processing route in influencing the contamination of cell wall material by side products, which, in turn, affects the macroscopic mechanical response of closed-cell Al-foams. Several kinds of Al-foams have been produced with pure Al/Al-alloys by the Alporas like melt process, all performed with and without Ca additive and processed either with conventional TiH₂ foaming agent or CaCO₃ as an alternative one. Damage behavior of contaminations was believed to affect the micromechanism of foam deformation, favoring either plastic buckling or brittle failure of cell walls. No discrepancy between experimental values of compressive strengths for Al-foams comprising ductile cell wall constituents and those prescribed by theoretical models for closed-cell structure was found while the presence of low ductile and/or brittle eutectic domains and contaminations including particles/layers of Al₃Ti, residues of partially reacted TiH₂, and Ca bearing compounds, results in reducing the compressive strength to values close to or even below those of open-cell foams of the same relative density.

1. Introduction

Remarkable absorbing ability resulted from capacity of closed-cell aluminum foams to undergo large strains (up to 60–70%) under almost constant stress offers significant performance gains for crash protection and other applications where effective utilizations of impact energy are required [1]. For instance, in aluminum foam sandwich (AFS) structures composed of metal/ceramic coversheets and Al-foam core, the last one is an efficient impact energy absorber that limits accelerations in crash accidents, providing crash protection for terrestrial and marine vehicles [2, 3]. That is why there has been an extensive interest in the production [1, 4–10] and mechanical performance of Al-foams [11–16].

Despite continuous efforts, the production processes for Al-foams suffer technical and economical limitations. As applied to the high-usage production methods based on handling of a melt and powder compact technique [4, 10] economical limitation arises particularly due to the employing of costly conventional foaming agent, titanium hydride (TiH₂).

In addition, expensive granulated Ca used as thickening agent contributes in material cost of Al-foam produced by conventional melt processing like Alporas route [17] while rather expensive gas atomized Al/Al alloy powder leads to increasing the material cost of the precursor and therefore products manufactured via powder compact technique [4, 10]. Because of this there is a strong motivation to develop cost effective processing routs. At this point cheap calcium carbonate (CaCO₃) as alternative foaming agent has been originally proposed by the researches in Japan in the developing the Alporas route [6] and later its applicability has been extended for powder compact technique [5, 6, 9]. In addition, melt processing like Alporas route that provides the increasing melt effective viscosity with no admixture of granulated Ca has been recently developed [18]. Nevertheless, transfer of Al-foam in engineering practice cannot be done without a detailed knowledge of the Al-foam properties (including mechanical ones) and limits of foaming processes.

It is of common knowledge that the most important microstructural feature affecting the mechanical properties

is relative density, the ration of density of the foam to that of the solid, ρ/ρ_s . Several approaches based on an idealized representation of a defect-free cellular structure have been developed for interpreting mechanical behavior of foams. Among those are the high-usage approaches for describing mechanical properties of ideal open- and closed-cell foams which are summarized in [11]. The simplest approach is based on dimensional arguments and gives the dependence of properties on relative density and on cell wall properties but not on cell geometry [19]. The complex cell geometry of foams is difficult to model accurately. At this approach the constants relating to cell geometry are usually found by fitting the model equations to experimental data. The second method that approximates the unit cell as tetrakaidecahedron is capable of estimating geometrical constants by using either structural mechanics or finite element analysis [20–23]. The third approach based on spatially periodic arrangement of several random Voronoi cells by using finite element analysis [24] provides the best representation of foams cell geometry. Cell unit with flat faces are usually used in the models.

However, the actual profile of mechanical properties for real Al-foams is far removed from theoretical predictions based on idealized representations of defect-free cellular materials [11]. In particular, a number of available cellular materials and especially closed-cell foams yield at a relatively strength that is lower than that predicted by theoretical models [11, 19]. The scattering of the mechanical properties impedes practical applications of foams [25, 26].

It is commonly considered that disagreements between experimental results and theoretical predictions arise due to different structural imperfections existing in real metallic foams. Combination of synchrotron X-ray microtomography and mechanical analysis including finite element simulation elucidates the influence of structural imperfection on mechanical performance of foams [11, 27–32]. In particular, deformation mechanism of foams depends strongly on the cell morphology whilst the effect of the cell size is negligible [27, 29, 32]. Irregularities in the cell shape on mesoscopic level can induce localized bending. For instance, X-ray microtomography indicates that highly elliptical cells with T-shape can induce bending in the neighboring cell walls, initiating the collapse of deformation bands [11, 27]. Finally, curvature and corrugation of cell faces [26, 28] and micropores and their spatial distribution in cell walls [33] as well as nonhomogeneous density distribution [29, 34] and fractured cell walls [11, 35] are considered to be the key factors in control of mechanical behavior of aluminum foams. However, it is difficult to quantify the precise significance of these factors because of microscopic features such as foreign particles, precipitates, and solute elements present in the cell wall material, currently thought to be also of great importance, resulting at least in the nonhomogeneous stress/strain distribution. Nevertheless, the microstructural aspects (especially those referred to mechanical properties of the cell wall constituents) are still largely ignored in most studies, despite the known fact that microstructural features would have dramatic effects on the performance characteristics of corresponding bulk material.

This problem becomes increasingly pronounced when foaming processes are performed with gas-releasing agent and other additives, resulting in unconventional matrix alloy comprising great number of various intermetallic compounds and other foreign particles [2, 8, 11, 36]. Great number of various intermetallic compounds and other foreign particles formed in the course of the foaming process substantially affect the micromechanism of deformation, degrading the mechanical response of foams [2, 14, 15, 36]. Unfortunately, evidence concerning the mechanical response of Al-based intermetallic compounds and other particles, typical for the cell wall material of aluminum foams, is few in number [16, 36].

This effort is to elucidate the role of processing additives in influencing the mechanical performance of Al-foams processed with different kinds of parent Al-alloys via Alporas route. Attention is primarily concentrated on the effect of damage behavior of cell wall constituents induced by processing additives on macroscopic compressive behavior of Al-foam.

2. Materials and Experimental Procedure

2.1. Materials. Several kinds of closed-cell foams marked as F1–F14 and listed in Table 1 were used in experiments. Pure aluminum (purity 99.95) and several conventional Al-alloys were used as matrix materials. Foams 1 and 2 were processed with pure aluminum, whereas the foams F3–F6 were processed with cast Al-7Si alloy (similar to A356 alloy). Wrought alloy with elementary composition of Al-1Mg-0.6Si-0.28Cu-0.2Cr (similar to 6061 alloy) and Al-5Mg alloy (similar to 5356 alloy) were employed to produce the foams F7, F8, F9, and F10, respectively. In addition, Al-Zn-Mg alloy with composition of Al-5.5Zn-3Mg-0.6Cu-0.5Mn doped additionally by small amount (<0.6 wt.%) of Sc and Zr (similar to 7075 alloy) was also chosen as a parent material for fabrication of F11–F14 foams.

All kinds of Al-foams were produced via Alporas like route in which either titanium hydride TiH_2 or calcium carbonate CaCO_3 were employed as foaming agents [9, 14, 15]. In addition, both hydride and carbonate Al-foams were produced either with or without Ca additive introduced usually into melt as thickening agent. All kinds of Al-based foams were performed by cylindrical blocks of 90 mm in diameter and 180 mm in height. A number of samples were directly machined from each kind of as-received foamed materials to use them for structural characterization and testing. Sample dimensions were about $20 \times 20 \times 30 \text{ mm}^3$ and $30 \times 30 \times 45 \text{ mm}^3$.

In addition, several solid alloys of compositions roughly corresponded to those formed in the cell wall materials of the studied Al-foams were fabricated by casting to use them in the experimentation. Approximated values of yield strength for these solid materials, listed in Table 1, were determined by the conventional mechanical tests in tensile to use them as input data in theoretical models for interpreting the behavior of foam under compression.

TABLE 1: Characteristics for different kinds of Al-based foams produced by Alporas like route.

Foam code	Processing variables (alloy and additives) wt.%	Relative density (ρ/ρ_s) ¹	Cell size, mm	Solid yield strength, σ_{ys} (MPa)
F1	Al + 1TiH ₂ + 1Ca	0.21–0.37	3.1 ± 0.9	42.8 ± 4.89
F2	Al + 2CaCO ₃ + 1Ca	0.24–0.09	1.5 ± 0.6	43.5 ± 7.12
F3	Al-7Si alloy + 1.5TiH ₂ + Ca	0.17–0.30	3.0 ± 0.4	220 ± 20.54
F4	Al-7Si alloy + 1.5TiH ₂	0.17–0.24	3.2 ± 0.5	180 ± 21.68
F5	Al-7Si alloy + 2CaCO ₃ + 1Ca	0.18–0.29	1.5 ± 0.5	195 ± 19.53
F6	Al-7Si alloy + 2CaCO ₃	0.18–0.27	1.7 ± 0.6	140 ± 15.67
F7	Al-1Mg-0.6Si alloy + 1.5TiH ₂ + 1Ca	0.15–0.26	2.1 ± 0.6	120 ± 14.82
F8	Al-1Mg-0.6Si alloy + 1.5TiH ₂	0.25–0.43	2.3 ± 0.7	100 ± 9.85
F9	Al-5Mg alloy + 1.5TiH ₂ + 1Ca	0.18–0.32	3.6 ± 0.5	180 ± 19.73
F10	Al-5Mg alloy + 1.5TiH ₂	0.31–0.40	3.5 ± 0.6	160 ± 17.13
F11	Al-Zn-Mg alloy + 1.5TiH ₂ + 1Ca	0.22–0.38	2.1 ± 0.7	560 ± 28.24
F12	Al-Zn-Mg alloy + 1.5TiH ₂	0.19–0.40	2.3 ± 0.6	540 ± 26.15
F13	Al-Zn-Mg alloy + 2CaCO ₃ + 1Ca	0.20–0.34	1.1 ± 0.5	575 ± 29.48
F14	Al-Zn-Mg alloy + 2CaCO ₃	0.20–0.33	1.2 ± 0.6	531 ± 15.14

¹ ρ and ρ_s correspond the density of foam and bulk solid, respectively.

2.2. Structural Characterization. All samples machined from the studied kinds of Al-foams were characterized by their relative density ρ/ρ_s (where ρ and ρ_s correspond to the density of foam and solid, resp.), cell morphology, and cell wall microstructure. Relative density, ρ/ρ_s , was measured by weighing a sample of known volume. Range of relative density for the samples machined from the studied kinds of Al-foams is listed in Table 1. Cell morphology, including cell size and shape, was studied by using scanned images of cellular structure for each kind of the studied Al-foams. Cell size indicative of the studied kinds of Al-foams is presented in Table 1. Microstructure of cell wall materials for the studied Al-foams was investigated using scanning electron microscopy (SEM) in both secondary and back-scattered modes. Material elementary composition was studied using energy dispersive X-Ray spectroscopy (EDS) and electron probe microanalysis (EPMA).

2.3. Mechanical Testing. Deformation behavior of Al-foams was examined under uniaxial compressive tests performed on prismatic specimens with dimensions either $20 \times 20 \times 30 \text{ mm}^3$ or $30 \times 30 \times 45 \text{ mm}^3$. The minimum dimension of particular specimen in each of three directions was seven times more than the cell size to avoid size effect. The compression tests were performed on a servohydraulic testing machine under displacement control and static strain rate of $1.5 \times 10^{-3} \text{ s}^{-1}$.

3. Results and Discussion

3.1. Material Characterization. All kinds of the studied Al-foams were believed to have closed cells of roughly spherical shape [14]. However, homogeneity of the cellular structure and mean cell size for carbonate foams (F2, F5, F6, F13, and F14) are found to be at least two times smaller than that for

hydride ones (F1, F3, F4, F11, and F12) processed with the same parent alloys, as evidenced from Table 1.

Figure 1 shows microstructure of cell wall materials for several kinds of Al-foam. Cell walls of foams (F1–F10) based on pure Al and Al alloys with compositions Al-7Si, Al-1Mg-0.6Si, and Al-5Mg consist of coarse Al dendrites rounded by a network of eutectic domains (light grey), as was originally shown in [8, 14, 16, 36]. Interdendritic network of redundant phase being emerged in a matrix of Al solid solution with randomly scattered Al₃(ScZr) intermetallic particles is characteristic for the foams (F11–F14) processed with Al-Zn-Mg-alloys [14, 15, 36].

Excluding carbonate kinds of Al-foams (F2, F6, F13, and F14) cell wall materials for all other foams exhibit a lot of foreign particles. In Al-foams (F3 and F5) based on Al-7Si alloy and processed with Ca additive, coarse crystals compositionally corresponded to Al₂CaSi₂ intermetallic compound (1) and are presented in the cell wall material besides E (Al + Si) eutectic domains (2), as can be seen in Figure 1(a). Formation of needle-shaped Al₂CaSi₂ crystals (5) is also detected in the cell wall material of Al-foam based Al-1Mg-0.6Si alloy (F7), as shown in Figure 1(b). Foreign particles of partly converted TiH₂ and/or its reaction products such as particles/layers Al₂Ti/Al₃Ti (12) are randomly distributed in the cell walls of hydride kinds of Al-foams (F1, F3, F4, and F7–F12). In line with [14] the above Ti-rich particles are mainly presented in the cell wall material of hydride kinds of Al foams (F4, F8, F10, and F12) processed without Ca additive, as can be seen in Figure 1(d).

The results of elementary distribution show that composition of eutectic domains formed in the cell wall material of other Al-foams was found to be rather different compared to those of parent alloys and dependent on the processing additives. Generally, dissolved Ca is largely accumulated within the eutectic domains/redundant phase, resulting in their local modification with formation of foreign Ca-bearing

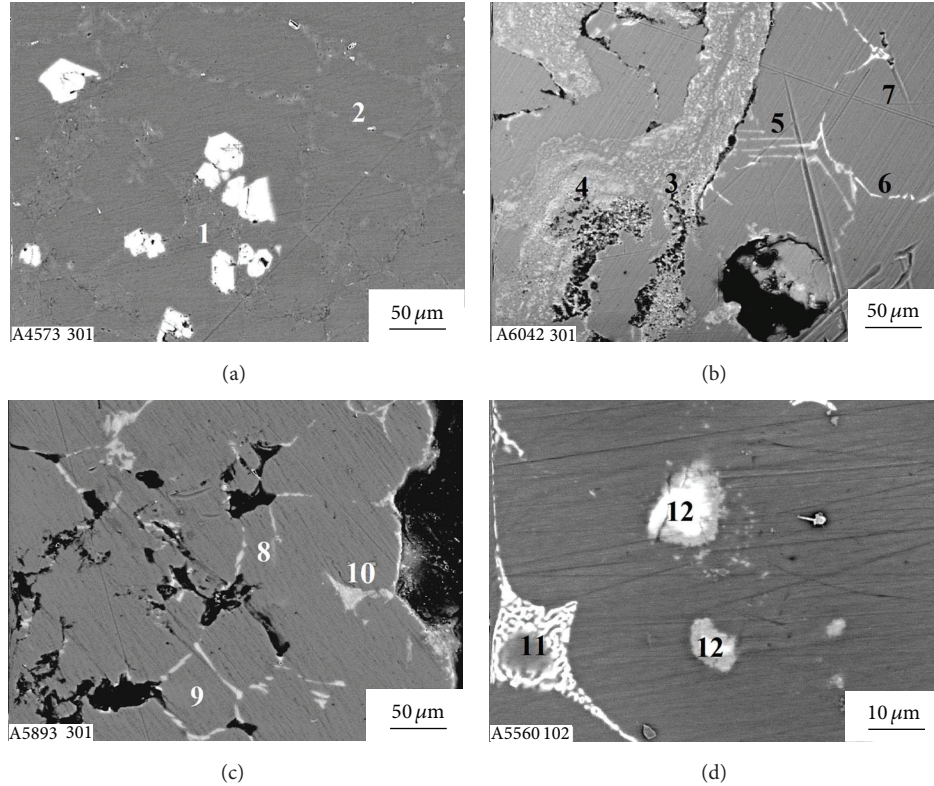


FIGURE 1: SEM micrographs of cell wall materials for Al-foams processed either with (a) CaCO_3 or with (b)–(d) TiH_2 and performed (a)–(c) with and (d) without Ca additive and performed with different parent alloys: (a) Al-7Si (F5), (b) Al-1Mg-0.6Si (F7), (c) Al-5Mg (F9), and (d) Al-Zn-Mg (F12).

eutectic zones. In particular, besides $\text{E}(\alpha\text{-Al} + \text{Mg}_2\text{Si})$ eutectic domains (6) indicative of parent Al-1Mg-0.6Si alloy, foreign eutectic zones such as $\text{E}(\alpha\text{-Al} + \text{Al}_4\text{Ca})$ (3), $\text{E}(\alpha\text{-Al} + \text{Al}_4\text{CaCu})$ (4), and $\text{E}(\alpha\text{-Al} + \text{Al}_2\text{CuMg})$ (7) are formed in Al-foam (F7), as shown in Figure 1(b). The same is true for Al-foam (F9) processed with Al-5Mg alloy. Cell wall material of Al-foam (F9) comprises Ca-bearing eutectic zones such as $\text{E}(\alpha\text{-Al} + \text{Mg}_2\text{Ca})$ (9) and $\text{E}(\alpha\text{-Al} + \text{Al}_4\text{Ca} + \text{Al}_3\text{Ti})$ (10) besides $\text{E}(\alpha\text{-Al} + \text{Mg}_5\text{Al}_8)$ eutectic domain (8) indicative of parent alloy, as shown in Figure 1(c). In addition, small amount (roughly about 0.26 at.%) of Ti solutes in Al matrix of hydride kinds of Al-foams. The latter is also concentrated within the eutectic domains, resulting in formation of Al_3Ti compound. As an example, Ti-bearing eutectic zones such as $\text{E}(\alpha\text{-Al} + \text{Al}_4\text{Ca} + \text{Al}_3\text{Ti})$ (10) and $\text{E}\{\alpha\text{-Al} + \text{T}(\text{AlCuMgZnTi})\}$ (11) are found in the cell walls of Al-foams (F9 and F12) based on Al-5Mg and Al-Zn-Mg alloys, respectively, as shown in Figures 1(c) and 1(d).

The important point concerns the difference in damage behavior of cell wall constituents comprised by cell wall materials of different kinds of Al-foams. In particular, Al + Al_4Ca eutectic domains indicative of carbonate kind of Al-foam (F2) processed with pure Al demonstrate quite high plasticity that is close to $\alpha\text{-Al}$ dendrites, whereas those indicative of all another kinds of Al-foams show low ductility and/or high brittleness [14, 16, 36]. Crumbling out the brittle eutectic domains/redundant phase occurs even after slightly slicing

the specimen, as can be seen in Figures 1(a) and 1(c). The same is true for contaminations including particles/layers of Al_3Ti , as well as residues of partially decomposed TiH_2 and Ca-bearing compounds. The data published in [16, 36] indicate that the solid materials, which compositionally corresponded to the above cell wall contaminations, demonstrate rather low ductility. Moreover, the latter solids show extremely small fracture toughness, K_{Ic} , although their strength is quite high. In particular, fracture toughness ($K_{Ic} = 1.71 \pm 0.18$) of titanium hydride TiH_2 is even less than that for technical glass ($K_{Ic} = 1.17 \pm 0.09$) [16]. This suggests that the presence of low ductile and/or brittle cell constituents can lead to impairing damage resistance of the cell walls, facilitating their premature failure under loading.

3.2. Compressive Response of Al-Foams. All kinds of Al-foams display a macroscopic mechanical response rather similar to elastic/plastic behaviour [1, 2, 11, 19]. However, different kinds of Al-foams exhibit considerable differences in microscopic deformation events at the “plateau” regime, as can be seen in Figures 2(a) and 2(b).

Figure 2(b) shows that carbonate kind of foam (F2) with ductile Al + Al_4Ca eutectic domains in the cell wall material [14, 16, 36] deforms smoothly which is typical for plastic buckling [11, 19]. In contrast to this slight hardening/softening effects superimposed upon an increasing “plateau” stress level

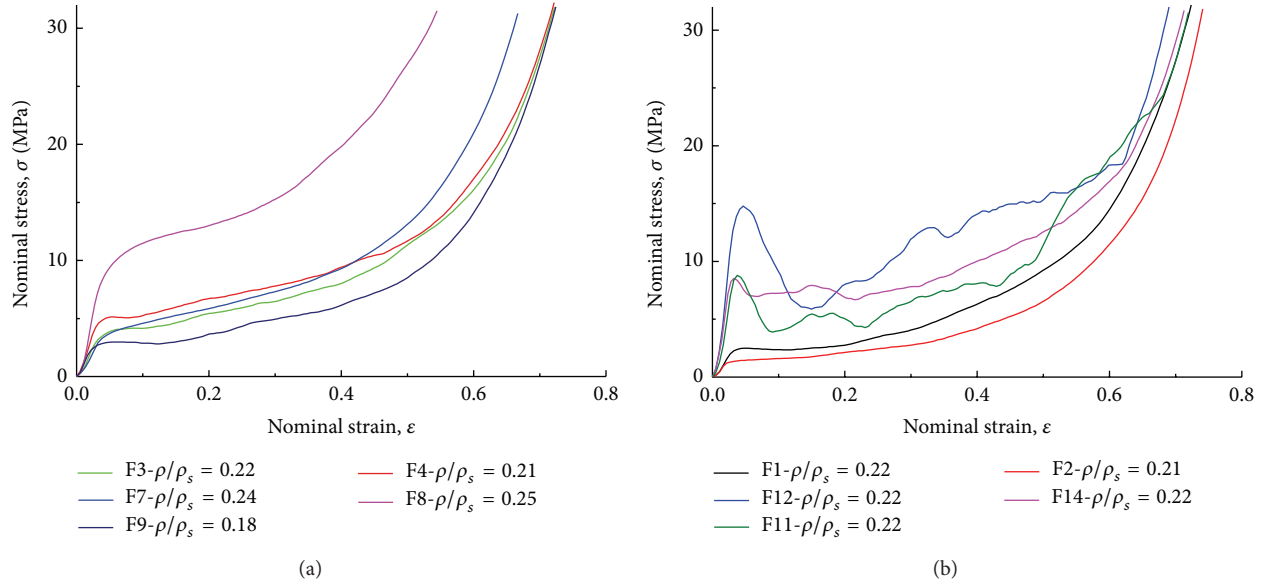


FIGURE 2: Compressive stress-strain curves for hydride (F1, F3, F4, F11, and F12) and carbonate (F2 and F14) kinds of Al/Al-alloy foams processed with (F1–F3, F7, and F11) and without (F4, F8, F12, and F14) Ca additive: (a) Al-foams based on Al-7Si alloy (F3 and F4), Al-1Mg-0.6Si alloy (F7 and F8), Al-5Mg alloy (F9); (b) Al-foams based on pure Al (F1, F2) and Al-Zn-Mg alloy (F11, F12, and F14).

is seen in deformation patterns of hydride kinds of Al-foams (F1, F3, F4 and F9) processed with pure Al and Al alloys such as Al-7Si and Al-5Mg. These deformation events are usually ascribed to the cell walls local failure being stimulated by crushing the low ductile eutectic domains and brittle foreign particles [12, 14, 34]. Hydride kinds of Al-foams (F11, F12) processed with Al-Zn-Mg alloy, whose cell walls comprise a high fraction volume of brittle foreign particles and coarse eutectic domains, show the most strong stress oscillations of “plateau” stress level, as can be seen in Figure 2(b).

The high fraction volume of coarse brittle redundant phase, large brittle particles of partly converted TiH_2 , and particles/layers $\text{Al}_2\text{Ti}/\text{Al}_3\text{Ti}$ impair cell ductility and toughness. In addition, the presence of high fraction volume of foreign strong particles results in relatively high stresses required for hydride kinds of Al-Zn-Mg foams (F11, F12) to commence densification. Because of this undesirable high peak stress at the onset of global collapse followed by strong load drop causes the plateau stress for the above kinds of Al-foams to saddle shape. The presence of foreign Ca-bearing zones within the domains in the cell wall material of Al-foam (F11) causes the compression strength to decrease, although the shape of stress-strain curve remains rather similar to that for hydride kind of Al-foam (F12) fabricated without Ca. The application of CaCO_3 foaming agent provides a remarkable improvement of deformation pattern Al-foam (F14) based on Al-Zn-Mg alloy. Figure 2(b) demonstrates that carbonate Al-foam based on Al-Zn-Mg alloy processed without Ca shows much smoother stress-curve which keeps peak-to-peak amplitude of oscillations to minimum level.

Thus, a comparative analysis of compressive response for different kinds of Al-foams elucidate the fact that microstructure and mechanical damage of cell wall constituents have a dramatic effect on the microscopic mechanism of local

deformation and failure, which in turn is thought to have an influence on the macroscopic mechanical response of Al-foams. Brittle cell wall constituents such as brittle particles of partly converted TiH_2 rounded by an $\text{Al}_2\text{Ti}/\text{Al}_3\text{Ti}$ layer and smaller Al_3Ti particles as well as brittle eutectic domains/redundant phase act as likely sites for the initiation of cracks, propagation of which generates stress concentration in adjacent areas, intervening the Al-matrix, as can be seen in Figure 3. The final failure of cell walls apparently occurs by crushing the brittle cell constituents and their bridging across intact ligaments. Again, the local fracture of deformation bands causes oscillations of “plateau” stress, as shown in Figure 2.

3.3. Comparison of Al-Foam Compressive Strength with Theoretical Models. A comparison of experimental results outlined in this effort with theoretical predictions was fulfilled to estimate the role of cell wall microstructure and mechanical damage of cell wall constituents in mechanical performance of closed-cell Al-foams. Among several models based on idealized representation of a defect-free cellular structure the most famous relations applied for describing mechanical properties are published in [11, 19]. For open-cell foams made of elastic-plastic materials, dimensional arguments give the correlation of plastic collapse stress, σ_{pl} , relative to the yield strength of solid cell edge material, σ_{ys} , versus relative density, ρ/ρ_s , as [19]

$$\frac{\sigma_{\text{pl}}}{\sigma_{\text{ys}}} = C_3 \left(\frac{\rho}{\rho_s} \right)^n, \quad (1)$$

where $n = 3/2$ is power index and the constant C_3 related to cell geometry is roughly about 3 for a wide range of foams.

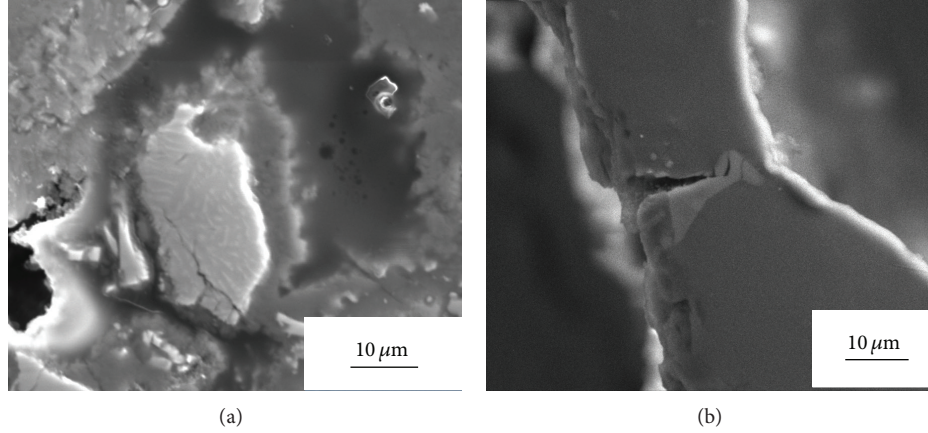


FIGURE 3: SEM images of the cell wall material for (a) hydride and (b) carbonate kinds of Al foams (F12, F13) based on Al-Zn-Mg alloy and performed (b) with (F13) and (a) without (F12) Ca additive: (a) cracks within partly converted TiH_2 , (b) crack lengthways the domain of redundant phase.

For closed-cell foams, yielding of stretched cell faces contribute to their strength. Because of this the additional term on right hand side appears in the relation for the plastic collapse stress:

$$\frac{\sigma_{pl}}{\sigma_{ys}} = C_3 \left(\frac{\rho}{\rho_s} \right)^n + C'_3 \left(\frac{\rho}{\rho_s} \right), \quad (2)$$

where power index $n = 1.5$.

For tetrakaidecahedral unit with flat faces, finite element analysis gives slightly different values in (2). According to [28] power index at the first term on the right hand side was found as $n = 2$ while the values of constants were determined as great as $C_3 = 0.33$ and $C'_3 = 0.44$.

Generally, compressive strength is usually defined either by “plateau” stress relative to the yield strength or by compressive strength at 20% strain [11]. Both yield stresses, σ_y , at the general yielding and plateau stress up to densification, σ_{pl} , [14] are used in the present study. Approximate values of yield strength, σ_{ys} , for solids which compositionally corresponded to the cell wall materials were determined by conventional mechanical tensile tests. The values of parameters σ_{ys} are listed in Table 1.

Following [11] data for the relative compression strength, σ_y/σ_{ys} and σ_{pl}/σ_{ys} , for different kinds of Al-foams are plotted in Figure 4 along the lines representing (1) and (2). Figure 4(a) shows that the data for carbonate kind of Al-foam F2 processed with pure Al lie close to (2), as prescribed by the theory for closed-cell foams. However, a behavior of all the other kinds of Al-foams deviates more or less from theoretical predictions. Data for hydride kind of Al-foam (F1) processed with pure aluminum lie below (2) and shift to (1), as can be seen in Figure 4(a). Deviation of experimental results from theoretical predictions suggests the decreased contribution of plastic bending to failure.

The same is true for carbonate kind of Al-foam (F6) based on Al-7Si alloy and processed without Ca as well as for hydride kinds of Al-foams processed with alloys such as Al-7Si, Al-1Mg-0.6Si, and Al-5Mg and performed either

with (F8) or without (F10) Ca additive. Figure 4(b) shows that the data for yield stress of those Al-foams lie well below (2) and shifted to (1), whereas those for plateau stress lie close to the line representing strength for closed-cell foam. The discrepancy between (2) and the data for hydride kinds of Al-7Si foams (F3, F4) and carbonate kind of Al-7Si foam (F5) with Ca additive is the most pronounced. Figure 4(b) shows that the data for plateau stress of those Al-foams shift essentially below (2) while the data for yield stress lie either well below or at least along the line representing open-cell foam. Compressive behavior of hydride kinds of Al-foams (F7, F9), which were processed with alloys such as Al-1Mg-0.6Si and Al-5Mg and admixture of Ca, is very similar to that of Al-foams (F3, F5) based on Al-7Si alloy, which were processed either with TiH_2 or $CaCO_3$ and performed with Ca additive. The noticeable difference is only that the increased thickness of cell walls causes the compressive strength of Al-foams F7, F9 to shift upwards when relative density increases up to $\rho/\rho_s > 0.20$. Figure 4(a) shows that both kinds of Al-foams (F11–F14) processed with Al-Zn-Mg alloy exhibit the most deflection of the experimental results from theoretical predictions. The data for yield and plateau stresses of Al-foams (F11, F13, F14) shift well below the line representing open-cell foam, whereas those of Al-foam F12 lie close to (1).

Generally, one or another relation between compressive strength and relative density, ρ/ρ_s , could be adjusted to approximate compressive strength of each kind of Al-foams the same as it was shown recently [16]. For instance, the compressive strength of Al-foams (F1, F2) processed with pure Al complies reasonably well with relations prescribed by (2) for closed-cell structure. However, it is noticeable that the value of numerical coefficient C'_3 for Al-foam F1 is somewhat reduced as compared to that for Al-foam F2. This is usually associated with a contribution of fracture mode in the collapse of deformation bands. The same is true for carbonate kinds of Al-foams (F8, F10) processed alloys such as Al-1Mg-0.6Si and Al-5Mg. For other kinds of Al-foams (F3–F7, and F9) processed with alloys such as Al-7Si, Al-1Mg-0.6Si, and Al-5Mg the values of numerical coefficient C'_3

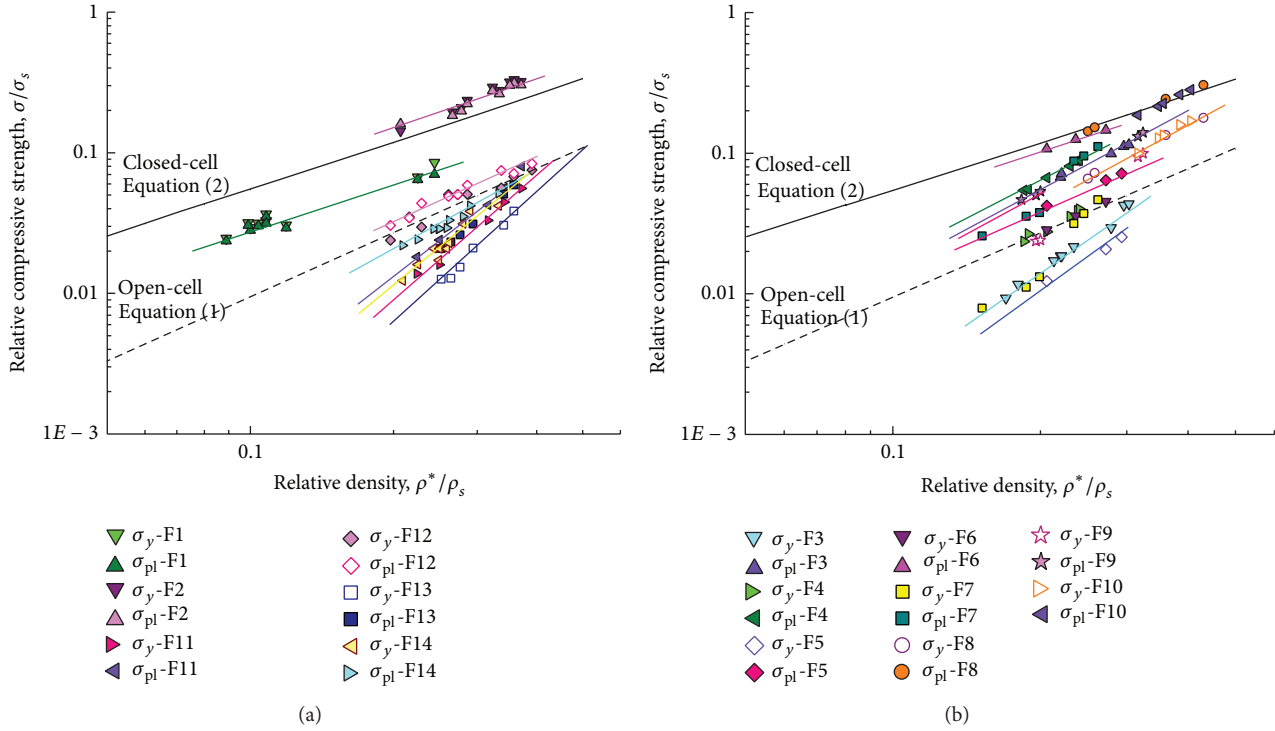


FIGURE 4: Relative compressive strength, σ_y/σ_{ys} and σ_{pl}/σ_{ys} , plotted against relative density, ρ/ρ_s , for different kinds of hydride (F1, F3, F4, and F7–F12) and carbonate (F2, F5, F6, F13, and F14) kinds of Al/Al alloy foams performed with (F1–F3, F5, F7, F9, F11, and F13) and without (F4, F6, F8, F10, F12, and F14) Ca additive: (a) Al-foams processed with Al (F1 and F2) and Al-foams of Al-Zn-Mg alloy (F11–F14); (b) Al-foams of Al alloys such as Al-7Si (F3–F6), Al-1Mg-0.6Si (F7 and F8), and Al-5Mg (F9 and F10).

relating to plateau stress are drastically reduced as compared to that prescribed by (2). Moreover, the numerical coefficient C'_3 relating to yield stress for the above foams is completely degraded up to zero. The results of approximation show that strength degradation for Al-foams (F11–F14) processed with Al-Zn-Mg alloy is rather strong. Besides the values of numerical coefficient C'_3 relating to yield and plateau stresses degraded up to zero, power index at the first term of (2) rises up to $n = 3$.

Thus, discrepancies of actual compressive strength for Al-foams and theoretical predictions reflect the difference in their micromechanism of deformation. By considering the evidence above it is easy to show that damage behavior of the cell wall constituents affects primary micromechanism of deformation, favoring either plastic buckling or brittle failure of the cell walls. Compressive stress, whose Al-foams can undergo up to densification, is proved to be actually very sensitive to small defects induced by crushed brittle constituents in the cell wall microstructure. An attention should be paid to the fact that effect of brittle constituents in the cell wall material on degradation of strength properties is much stronger. As it can be seen in Figure 4, the latter is comparable with that implemented by decreasing a relative density of intact Al-foam that is free of defects.

4. Conclusions

Crucial role of foaming agent and Ca additive in contaminations of the cell wall material by side products and, hence,

in macroscopic mechanical response of closed-cell Al-foams being fabricated via Alporas like route was justified.

Correlations of relative compressive strength, σ/σ_s , versus relative density ρ/ρ_s , were obtained and analyzed. No discrepancy between experimental values of compressive strengths for Al-foams comprising ductile cell wall constituents and those prescribed by theoretical models based on an idealized representation of defect-free cellular structure for closed-cell structure is found while the opposite was believed to be true in the presence of low ductile and/or brittle processing contaminations including particles/layers of Al_3Ti , residues of partially reacted TiH_2 , Ca-bearing compounds, and/or modified eutectic domains. The latter contaminations result in reducing the compressive strength to values close to or even below those of open-cell foams of the same relative density, ρ/ρ_s . Considerable discrepancy of actual compressive strength of Al-foams and theoretical predictions resulted from difference in micromechanism of deformation, which, in turn, is affected by damage behavior of the cell wall constituents, favoring either plastic buckling or brittle failure of the cell walls.

The results of this work bring about a better understanding of the interplay between processing conditions, cell wall microstructure, damage behavior of cell wall constituents, and mechanical response of Al-foams.

Conflict of Interests

The authors declare that there is no conflict of interests regarding the publication of this paper.

Acknowledgments

This research was supported by National Academy of Science of Ukraine under the Project no. III-2-13. Special thanks are due to the researchers of Tohoku University, Japan, for fruitful discussions and cooperation.

References

- [1] M. F. Ashby, A. G. Evans, N. A. Fleck, L. J. Gibson, J. W. Hutchinson, and H. N. G. Wadley, *Metal Foams: A Design Guide*, Butterworth Heinemann, Boston, Mass, USA, 2000.
- [2] A. E. Markaki and T. W. Clyne, "Characterisation of impact response of metallic foam/ceramic laminates," *Materials Science and Technology*, vol. 16, no. 7-8, pp. 785–791, 2000.
- [3] V. Crupi, G. Epasto, and E. Guglielmino, "Impact response of aluminum sandwiches for light-weight ship structures," *Metals*, vol. 1, pp. 98–112, 2011.
- [4] J. Banhart, "Manufacture, characterisation and application of cellular metals and metal foams," *Progress in Materials Science*, vol. 46, no. 6, pp. 559–632, 2001.
- [5] R. Neugebauer, J. Hipke, T. Hohlfeld, and R. Thummler, "Highly damped machine tools with metal foam," in *Proceedings of the International Conference Advanced Metallic Materials*, J. Jerz, Ed., pp. 214–218, Institute of Materials and Machine Mechanics, Smolenice, Slovakia, November 2003.
- [6] T. Nakamura, S. V. Gnyloskurenko, K. Sakamoto, A. V. Byakova, and R. Ishikawa, "Development of new foaming agent for metal foam," *Materials Transactions*, vol. 43, no. 5, pp. 1191–1196, 2002.
- [7] V. Gergely, D. C. Curran, and T. W. Clyne, "The FOAMCARP process: foaming of aluminium MMCs by the chalk-aluminium reaction in precursors," *Composites Science and Technology*, vol. 63, no. 16, pp. 2301–2310, 2003.
- [8] S. Gnyloskurenko, T. Tnakamura, A. Byakova, Y. Podrezov, R. Ishikawa, and M. Maeda, "Development of lightweight al alloy and technique," *Canadian Metallurgical Quarterly*, vol. 44, no. 1, pp. 7–12, 2005.
- [9] A. Byakova, A. Sirko, K. Mykhalenkov, Y. Milman, S. Gnyloskurenko, and T. Nakamura, "Improvements in stabilisation and cellular structure of Al based foams with novel carbonate foaming agent," *High Temperature Materials and Processes*, vol. 26, no. 4, pp. 239–245, 2007.
- [10] J. Banhart, "Light-metal foams history of innovation and technological challenges," *Advanced Engineering Materials*, vol. 15, no. 3, pp. 82–111, 2013.
- [11] L. J. Gibson, "Mechanical behavior of metallic foams," *Annual Review of Materials Science*, vol. 30, pp. 191–227, 2000.
- [12] A. E. Markaki and T. W. Clyne, "The effect of cell wall microstructure on the deformation and fracture of aluminium-based foams," *Acta Materialia*, vol. 49, no. 9, pp. 1677–1686, 2001.
- [13] T. Miyoshi, T. Mukai, and K. Higashi, "Energy absorption in closed-cell Al-Zn-Mg-Ca-Ti foam," *Materials Transactions*, vol. 43, no. 7, pp. 1778–1781, 2002.
- [14] A. V. Byakova, S. V. Gnyloskurenko, A. I. Sirko, Y. V. Milman, and T. Nakamura, "The role of foaming agent in structure and mechanical performance of Al based foams," *Materials Transactions*, vol. 47, no. 9, pp. 2131–2136, 2006.
- [15] Y. Milman, A. Byakova, A. Sirko, S. Gnyloskurenko, and T. Nakamura, "Improvement of structure and deformation behaviour of high strength Al-Zn-Mg foam," *Materials Science Forum*, vol. 519–521, no. 1, pp. 573–578, 2006.
- [16] A. Byakova, S. Gnyloskurenko, and T. Nakamura, "The role of foaming agent and processing route in the mechanical performance of fabricated aluminum foams," *Metals*, vol. 2, no. 2, pp. 95–112, 2012.
- [17] S. Akiyama, H. Ueno, K. Imagawa et al., "Foamed metal and method of producing same," US Patent no. 4713277, 1987.
- [18] A. V. Byakova, A. Vlasov, S. V. Gnyloskurenko, and I. Kartuzov, "Method for making the blocks of foamed aluminum/aluminum alloys," UA Patent no. 104367, 2014.
- [19] L. G. Gibson and M. F. Ashby, *Cellular Solids: Structure and Properties*, Cambridge University Press, Cambridge, UK, 1997.
- [20] W. E. Warren and A. M. Kraynik, "The linear elastic properties of open-cell foams," *Journal of Applied Mechanics*, vol. 55, no. 2, pp. 341–346, 1988.
- [21] H. X. Zhu, J. F. Knott, and N. J. Mills, "Analysis of the elastic properties of open-cell foams with tetrakaidecahedral cells," *Journal of the Mechanics and Physics of Solids*, vol. 45, no. 3, pp. 319–343, 1997.
- [22] W. E. Warren and A. M. Kraynik, "Linear elastic behavior of a low-density Kelvin foam with open cells," *Journal of Applied Mechanics*, vol. 64, no. 4, pp. 787–794, 1997.
- [23] N. J. Mills and H. X. Zhu, "The high strain compression of closed-cell polymer foams," *Journal of the Mechanics and Physics of Solids*, vol. 47, no. 3, pp. 669–695, 1999.
- [24] A. M. Kraynik, "The structure of random foam," in *Proceedings of the 4th International Conference on Porous Metals and Metal Foaming Technology (MetFoam '05)*, H. Nakajima and N. Kanetake, Eds., pp. 397–402, The Japan Institute of Metals, Kyoto, Japan, September 2005.
- [25] J. L. Grenestedt and F. Bassinet, "Influence of cell wall thickness variations on elastic stiffness of closed-cell cellular solids," *International Journal of Mechanical Sciences*, vol. 42, no. 7, pp. 1327–1338, 2000.
- [26] Y. Sugimura, J. Meyer, M. Y. He, H. Bart-Smith, J. Grenstedt, and A. G. Evans, "On the mechanical performance of closed cell al alloy foams," *Acta Materialia*, vol. 45, no. 12, pp. 5245–5259, 1997.
- [27] H. Bart-Smith, A.-F. Bastawros, D. R. Mumm, A. G. Evans, D. J. Sypeck, and H. N. G. Wadley, "Compressive deformation and yielding mechanisms in cellular Al alloys determined using X-ray tomography and surface strain mapping," *Acta Materialia*, vol. 46, no. 10, pp. 3583–3592, 1998.
- [28] A. E. Simone and L. J. Gibson, "The effects of cell face curvature and corrugations on the stiffness and strength of metallic foams," *Acta Materialia*, vol. 46, no. 11, pp. 3929–3935, 1998.
- [29] H. Harders, K. Hupfer, and J. Rösler, "Influence of cell wall shape and density on the mechanical behaviour of 2D foam structures," *Acta Materialia*, vol. 53, no. 5, pp. 1335–1345, 2005.
- [30] I. Jeon and T. Asahina, "The effect of structural defects on the compressive behavior of closed-cell Al foam," *Acta Materialia*, vol. 53, no. 12, pp. 3415–3423, 2005.
- [31] A. Marmottant, J. F. Despois, L. Salvo, E. Maire, M. Bornert, and A. Mortensen, "In-situ X-ray tomography investigation of replicated aluminium foam: quantitative analysis of localization using 3D strain mapping," in *Proceedings of the 4th International Conference on Porous Metals and Metal Foaming Technology (MetFoam '05)*, H. Nakajima and N. Kanetake, Eds., pp. 415–418, The Japan Institute of Metals, Kyoto, Japan, September 2005.
- [32] Y. Yamada, T. Banno, Z. Xie, and C. Wen, "Characterisation of aluminium foams using X-ray tomography," in *Proceedings of the 4th International Conference on Porous Metals and Metal Foaming Technology (MetFoam '05)*, H. Nakajima and

- N. Kanetake, Eds., pp. 419–422, The Japan Institute of Metals, Kyoto, Japan, September 2005.
- [33] H. Toda, N. Kuroda, and T. Ohgaki, “Image-based mechanical analysis of dynamic deformation and damage behaviors in an aluminum foam using synchrotron X-ray microtomography,” in *Proceedings of the 4th International Conference on Porous Metals and Metal Foaming Technology (MetFoam '05)*, H. Nakajima and N. Kanetake, Eds., pp. 409–414, The Japan Institute of Metals, Kyoto, Japan, September 2005.
- [34] B. Kriszt, B. Foroughi, K. Faure, and H. P. Degischer, “Behaviour of aluminium foam under uniaxial compression,” *Materials Science and Technology*, vol. 16, no. 7-8, pp. 792–796, 2000.
- [35] C. Chen, T. J. Lu, and N. A. Fleck, “Effect of imperfections on the yielding of two-dimensional foams,” *Journal of the Mechanics and Physics of Solids*, vol. 47, no. 11, pp. 2235–2272, 1999.
- [36] S. V. Gnyloskurenko, A. V. Byakova, A. I. Sirko, A. O. Dudnyk, and V. Yu. Milman, “Advanced structure and deformation pattern of Al based foamed with calcium carbonate agent,” in *Proceedings of the 5th International Conference on Porous Metals and Metallic Foams (MetFoam '07)*, L. P. Lefebvre, J. Banhart, and D. C. Dunand, Eds., pp. 399–402, DEStech Publication, Montreal, Canada, September 2007.

Research Article

Free-Form Rapid Prototyped Porous PDMS Scaffolds Incorporating Growth Factors Promote Chondrogenesis

Andrés Díaz Lantada,¹ Hernán Alarcón Iniesta,²
Beatriz Pareja Sánchez,¹ and Josefa Predestinación García-Ruiz²

¹ Product Development Laboratory, Mechanical Engineering & Manufacturing Department, Universidad Politécnica de Madrid (UPM), c/José Gutiérrez Abascal 2, 28006 Madrid, Spain

² Departamento de Biología Molecular, Universidad Autónoma de Madrid, 28049 Cantoblanco, Madrid, Spain

Correspondence should be addressed to Andrés Díaz Lantada; adiaz@etsii.upm.es

Received 7 October 2013; Accepted 29 November 2013; Published 2 January 2014

Academic Editor: Alexander Tsouknidas

Copyright © 2014 Andrés Díaz Lantada et al. This is an open access article distributed under the Creative Commons Attribution License, which permits unrestricted use, distribution, and reproduction in any medium, provided the original work is properly cited.

In this study, we present a promising approach for the rapid development of porous polydimethylsiloxane (PDMS) scaffold prototypes, with outer geometry defined from the design stage, according to the form of conventional implants or adapted to patients' biostructures. The manufacture method is based on phase separation processes using materials obtained by casting within additive rapid prototyped molds. We include a comparative study of PDMS sponges obtained by different simple processes. Final *in vitro* assessment is carried out using hMSCs (bone marrow-derived human mesenchymal stem cells), cultured onto porous PDMS scaffolds functionalized with aminopropyltriethoxysilane (APTS) and equilibrated with a trophic factors medium produced by the cells. Results show that porous PDMS scaffold prototypes are excellent 3D platforms for hMSCs adhesion. Furthermore, this PDMS-3D niche, seeded with hMSCs and chondrogenic incubation medium during three weeks, showed a successful chondrogenesis determined by collagen type II expression. Thus, results show a versatile method to produce a 3D niche to address questions about cartilage and endochondral bone formation or skeleton tissues clinical approaches.

1. Introduction

Tissue engineering combines biological, physical, and engineering knowledge to provide artificially developed substitutes for tissues and organs linked to repair and replacement therapies. A key element involved in tissue engineering processes is the extracellular matrix or scaffold which serves as substrate or framework for cell growth, aggregation, and tissue development [1]. These scaffolds must be porous so as to allow cell migration during the colonization process as well as the transport of nutrients and waste to and from cells, and they have to be also resistant enough to withstand possible mechanical demands, especially if final scaffold (or device) implantation is desired. Additionally, as cells are able to feel their microenvironment and substrate texture upon which they lie by changing their morphology, cytoskeleton configuration, and intra- and extracellular signaling, increasing efforts are continuously being focused on advanced

design and manufacturing technologies, so as to generate and modify the structures and surfaces of biomaterials. Aspects such as porosity, pore size, and surface microtexture promote cell adherence, migration, and proliferation within the scaffold, for subsequent differentiation into relevant cell types. Thus, tissue progenitor cells and the scaffold play a fundamental role in most tissue engineering strategies as their properties can deeply influence the global success of new tissue formation and the controlled fabrication of the scaffold structures is becoming increasingly important for novel approaches within regenerative medicine [2–4].

Most processes for manufacturing microporous structures for tissue engineering [5] involve combination of materials in some step of the process and a final phase separation, for obtaining a solid part with distributed small pores. Among most extended processes, gas-assisted injection molding is an industrial method based on injecting a molten resin or thermoplastic into a mold cavity and then applying a quantity

of pressurized gas into the resin, so as to help to fill out the mold cavity and to create hollows and pores in the polymer. The incorporation of foaming agents as additives to polymers also allows the manufacture of polymeric parts with pores. In many strategies including tissue strategies, to obtain 3D porous structures is absolutely required to irrigate the tissue and maintain an adequate liquid dynamics. The use of porogens is also commonplace; normally, the process involves mixing a liquid prepolymer with solid particles (typically wax, sugar, salt, etc.). Once polymerization is produced, normally by UV exposure or by heating, a solid structure, formed by a polymeric network with dispersed particles, is obtained. Final porous structure is obtained by dissolving such disperse particles in water or other solvents or by heating. The use of prepolymer-water emulsions is also typical for obtaining a polymerizable mixture that after thermal or UV-based polymerization provides a polymeric network with pores according to initial water content (i.e., polyHIPES).

Main alternative, for improving the control of scaffolds' pore size and distribution, from the design stage, is the use of micro additive manufacturing technologies (AMT), normally working on layer-by-layer processes, following the geometries obtained with the help of computer-aided designs [6, 7]. Electrospinning can be also adapted to "layer-by-layer" fabrication and used for obtaining 3D porous structures [8], even though the process is not as repetitive as the use of micro AMT. The progressive increase in precision of additive manufacturing technologies, together with their improved versatility, thanks to a continuously increasing set of materials available for layer-by-layer processing, is greatly promoting applications linked to micro- and even nanomanufacturing of complex 3D geometries for very innovative medical solutions in several fields [5].

Several scaffolds with controlled microstructures have been manufactured using different RP technologies, such as selective laser sintering [9], layered hydrospinning [10], laser stereolithography [11], digital light projection [12] or two-photon lithography [13], and different materials including hydrogels [14], gelatin [7], titanium alloys [15, 16], some photopolymers [17], and ceramics [18]. However, *in vitro* validation of such rapid prototyped scaffolds is not so common, as most processes/materials do not provide an adequate combination for promoting biocompatibility and in many cases generate toxic components. Nevertheless, some highly interesting research has already been published, including *in vitro* validation and toxicity assessment [19, 20]. Advances in the field of biomedical polymers [19–21] together with the possibilities of chemical/physical-vapor deposited (CVD-PVD) coatings for biocompatibility enhancement [11] are bringing new possibilities to this area, although access to such materials and technologies is not always easy, as some of them are currently under development.

In any case, it seems clear that a universal methodology for tissue engineering scaffold development is not yet available, first of all due to the complexity of biological materials and systems and also due to all the possible design resources, manufacturing technologies, and related materials available, whose results have not been systematically compared. For

instance, additive manufacturing technologies allow precise control of final geometries from the design stage; however, such designs are normally obtained by combining Euclidean based (simple) geometries and final result does not mimic adequately the complexity of biomaterials. On the other hand, scaffolds obtained by phase separation and more "traditional" processes typically lead to more biomimetic sponges, even though their final outer form and repeatability are more difficult to control than using computer-aided strategies linked to rapid prototyping using additive processes.

Therefore, further research is needed to address the advantages of combining different technologies [22] for manufacturing enhanced, even personalized, scaffolds for tissue engineering studies and extracellular matrices with global (outer) geometries defined as implants for tissue repair. In addition, increasing data show that progenitor cell-niche formation is absolutely needed for tissue development and repair [23]. Indeed, the niche composition and 3D structure play an important role in stem cells state and fate. The niche is created by the specific combination of trophic factors produced by progenitor cells to maintain capability for tissue repair and regeneration and specific extracellular matrix. Recent studies have helped to highlight the extreme relevance of the incorporation of adequate growth factors, within the scaffold, for promoting biological regulation, cell differentiation, angiogenesis, and final tissue viability [24–26].

The term "adequate growth factors" makes reference to a chondrogenic medium that was proposed at the laboratory of Arnold I. Caplan who coined the term mesenchymal stem cell, as described in Materials section. Such inclusion of biochemical effects, derived from the incorporation of the adequate growth factors, adds some additional uncertainties to the already complex to understand interactions between scaffolds' structure, morphology, and mechanical properties. Consequently, studies addressing these interesting synergies between extracellular matrices and growth factors and their impact on final tissue viability are needed, in the quest for the aforementioned universal methodology for versatile and successful tissue engineering scaffold development.

In this study we show an approach for the rapid development of porous polydimethylsiloxane (PDMS-3D) scaffold prototypes, with versatile outer geometry defined from the design stage, according to different tissue strategies, to the form of conventional implants or even adapted to patients' biostructures. The manufacture method is based on phase separation processes using parts obtained by casting within additive rapid prototyped molds. We include a comparative study of PDMS sponges obtained by different simple processes, including sugar leaching after polymerization, water extraction after polymerization of PDMS-water emulsions, and water extraction together with sugar leaching after polymerization of PDMS-sugar-water mixtures. By changing the proportions of these agents, main mechanical properties of the final scaffold can be tuned and adapted to the typical density and stiffness of several soft tissues. Different porous annuloplasty rings are also obtained, by means of example, so as to show the potential of these manufacture processes, towards free-form porous implants and scaffolds for tissue replacement and repair.

Results show that PDMS scaffolds functionalized with trophic factors produced by hMSCs isolated from bone marrow became a PDMS-3D niche for cells adhesion and chondrogenesis. Furthermore, the PDMS functionalized with APTS became an excellent niche for hMSCs for chondrogenesis that was increased if the PDMS-APTS structures were treated with trophic factors before being seeded with hMSCs. Thanks to the described process, scaffolds became buried of collagen type II, even within the porous structure of the material. Thus, we recommend these scaffolds for cartilage and endochondral bone formation/repair strategies.

2. Materials and Methods

2.1. Materials. Microporous PDMS has already been proposed as a functional material for cell culture where high degree of porosity is required to improve cell survival and functions. PDMS sponges have been obtained using precursor microemulsions [27, 28] and other processes based on particle (usually salt or sugar) leaching [29]. Mixtures of PMDS-sugar-water, for promoting multiscale porosities, are less common. In addition, porogen size and content are normally used as main control parameters for adjustment of final mechanical properties, although assessment of such mechanical properties is not so common [30, 31]. In this study we try to provide additional details about these special mixtures, considering also the proportions of the different agents and their impact on density, stiffness, and tensile strength, for additional comparison with soft tissues for potential replacement of repair.

For obtaining the PDMS sponges, we use a commercial Neukasil RTV-20 prepolymer, together with the Neukasil A2 cross-linker, both of them from Altrapol Kunststoff GmbH (Rudolf-Diesel-Strasse, 9-13, D-23617, Stockelsdorf, Germany). Both components are mixed according to manufacturer's data sheets and introduced in a vacuum chamber, at the beginning of polymerization, for adequate degasification. Complete polymerization at room temperature (25°C) lasts around 24 hours, which helps to manipulate the mixture with enough time for adequate molding. As porogen material we use Native Organic sugar (Balbo Group, Brazil), mixed in different proportions with PDMS and with PDMS-water emulsions. The mixtures analyzed in present study include the following weight distributions: 50 : 50 PDMS/water, 33.3 : 33.3 : 33.3 PDMS/water/sugar, 50 : 50 PDMS/sugar, 40 : 60 PDMS/sugar, 33.3 : 66.6 PDMS/sugar, and 28.5 : 71.5 PDMS/sugar, which lead to typical porosities used in tissue engineering and studies linked to scaffold development. A summary of the different compositions and morphologies studied and obtained, after particle leaching and drying (see process description below), is included in Figure 3, as brief summary.

Epoxy resin Accura 60 (3D Systems, 333 Three D Systems Circle, Rock Hill, SC, USA) is used as a base material for the rapid molds, subsequently used for casting the PDMS-sugar-water mixtures and for obtaining outer geometries controlled from the design stage, due to restrictions imposed by the laser

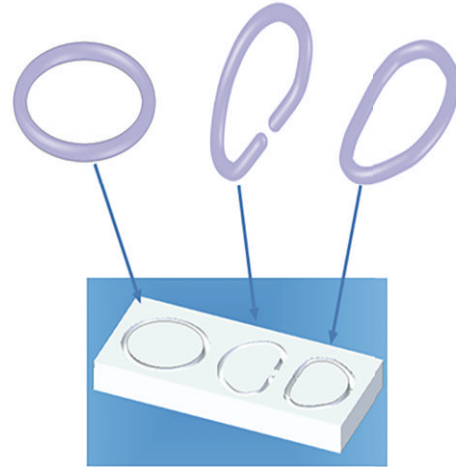


FIGURE 1: Computer-aided designs of different valve ring models and associated mold geometry.

stereolithography prototyping process used for such molds, as detailed below.

2.2. Design and Prototyping Processes. Several state-of-the-art implants aimed at tissue repair have circular or quasicircular ring geometries, from artificial sphincters to annuloplasty rings for heart valve (usually mitral) tissue reinforcement. These implants can greatly benefit from having controlled porosity and mechanical properties, as the pores can help to promote drug-eluting approaches for minimizing postsurgical risks, as well as allow for scaffold-based tissue engineering strategies. For instance, recent research has highlighted the potentials of rapid prototyped porous scaffolds for cardiac tissue engineering [32] and their adaptation to different cardiac prostheses, such as reinforcement valve rings; even using personalized designs [33] is almost direct.

As cases of study for present work, we have selected a circular ring, as possible reinforcement for tissues surrounding different sphincters, and a couple of mitral valve annuloplasty rings (one closed and one open) for potential reinforcement of valve tissue, as repair treatment for mitral valve insufficiency. These designs are aimed at verifying the possibility of obtaining PDMS sponges, with controlled outer geometries, by casting into rapid prototyped molds of different emulsions and mixtures including PDMS, sugar, and water.

The different implantable rings and associated mold geometries, as shown in Figure 1, are designed with the help of the computer-aided design software Solid Edge v.20 (Siemens Product Lifecycle Management Software Inc.) and are saved as stl files for subsequent communication with prototyping machines. The stl files with the 3D virtual CAD geometry of the mold designs are transferred to a laser stereolithography SLA-3500 machine (3D Systems, 333 Three D Systems Circle, Rock Hill, SC, USA) for subsequent rapid mold manufacture and casting of the PDMS mixtures (see also Figure 4). The process is based on an additive layer-by-layer photopolymerization of an epoxy resin that ends

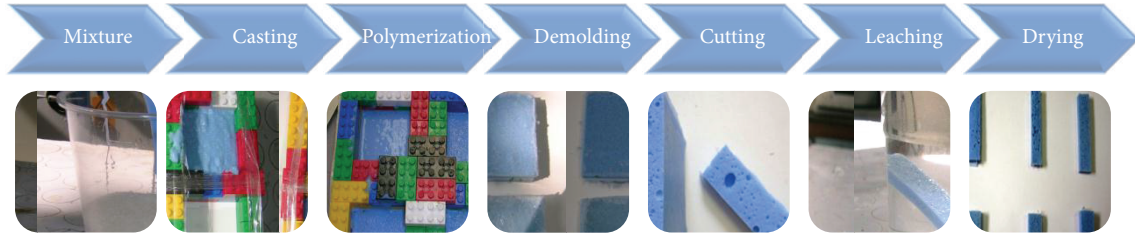


FIGURE 2: Overview of the manufacturing process used for obtaining PDMS sponges.

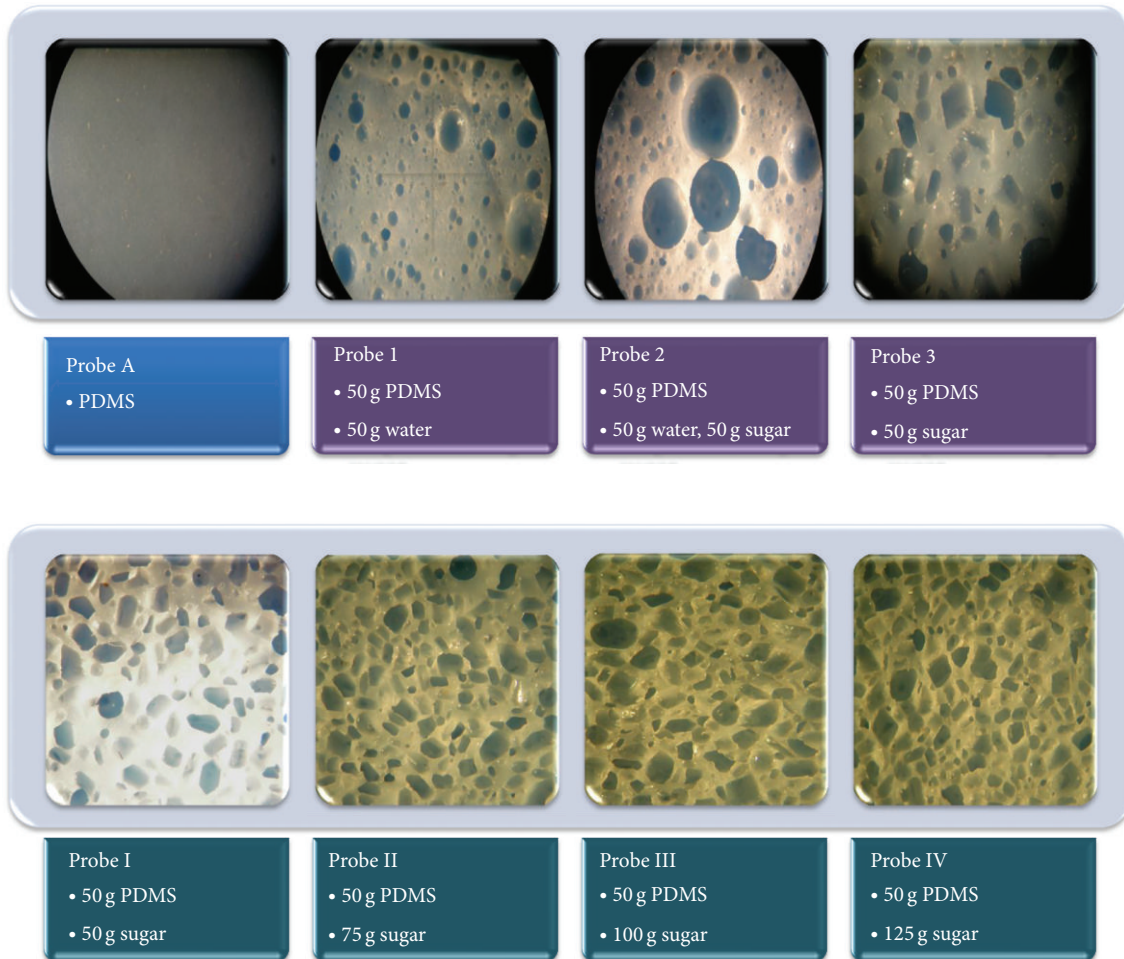


FIGURE 3: Different morphologies, after particle leaching and drying, obtained by systematic modification of the sugar and water content incorporated to the PDMS during the polymerization process.

up with a whole physical three-dimensional part. The SLA-3500 system available at the UPM Product Development Laboratory allows us to manufacture details down to about $150\ \mu\text{m}$, although more recent studies on the development of microstereolithography are gradually increasing its precision to submicrometric scales (NanoScribe GmbH), in spite of greatly limiting final part size to only a few mm^3 .

The prototyping process, either for the manufacture of porous PDMS scaffold probes or for the development of porous PDMS implants, includes several simple steps detailed further on and shown schematically in Figure 2. First of

all, the Neukasil RTV-20 prepolymer and the Neukasil A2 cross-linker are mixed and degasified, following manufacturer's instructions, as previously explained. Subsequently, the PDMS-water emulsion or the PDMS-sugar or PDMS-water-sugar mixtures are obtained with the help of a Taurus vertical mixer-blender spinning at 1200 r.p.m. during one minute just before casting.

Both open and closed molds can be used, as well as atmospheric and vacuum casting, depending on the desired final level of detail (vacuum casting helps to fill the molds and to promote replication quality). In our case, such mixtures



FIGURE 4: Example of the obtained porous PDMS annuloplasty rings aimed at valve tissue repair. Image from the PDMS rings casted into the rapid epoxy mold and details from the final parts.

are casted into rapid LEGO molds and into rapid prototyped epoxy molds for polymerization during 24 hours at room temperature. Once the PDMS mixtures are polymerized, demolding is accomplished for obtaining the desired implants or probes for mechanical testing, after adequate cutting. Particle leaching is achieved by water immersion and systematic squeezing of the material, probes, and prototypes. Final drying leads to the desired probes (see Figure 3) and implants (see Figure 4).

2.3. Mechanical Characterization. Mechanical characterization is addressed by tensile testing using a MTS 835 Damper Test System (MTS, 14000 Technology Drive, Eden Prairie, MN, USA), capable of applying compressive, tensile, and fatigue cycles (the machine and experimental setup are shown in Figure 5). In our case, the different $48 \times 10 \times 5 \text{ mm}^3$ porous PDMS probes obtained are submitted to tensile testing until breakdown (see detailed view from Figure 5) and the different stress-strain curves, resulting from such traction tests, are represented in Figure 6 for further discussion. The initial probe length between clamps is 30 mm and the tensile tests are carried out at a speed of 10 mm/minute.

The influence of material processing and of the different proportions of components, on the final physical properties of the PDMS sponges, are detailed in the following section, together with a comparative analysis of the mechanical properties of common soft tissues.

2.4. Cell Culture Processes and Imaging Techniques. The specific composition of the adequate chondrogenic growth factors, in comparison with other osteogenic or adipogenic ones, is reported by Pittenger et al. [34] and used in some references also aimed at chondrogenic differentiation [35–37]. In our case, two to four milliliters of human bone marrow samples from healthy donors were provided by Dr. Benjamin



FIGURE 5: MTS 835 Damper Test System and result from a traction test carried out with porous PDMS.

Fernández from the Fundación Jiménez-Díaz. The culture expansion of hMSCs was carried out, as previously described [35, 36].

Cells were plated and incubated using DMEM-L plus 10% FBS of selected batches. Cells were collected by treatment with 0.25% trypsin-EDTA. Cell culture media were prepared by the research services of Molecular Biology Center “Severo Ochoa” (CSIC-UAM). For the preparation of hMSCs trophic factors rich medium we used 8–10 p100 culture plates at 80% confluence for each batch. Cells were washed with PBS and starved of FBS during 24 hours. Afterwards, culture medium was collected and cleaned of any floating cell by centrifugation at 1.500 rpm in a bench centrifuge during 5 min. The clean supernatant was cooled down on ice during 30 min, centrifuged in a Sorvall to remove salt precipitations, and kept in 2 mL aliquots at -30°C until use. We avoid any samples with repeated freeze-thaw.

Cubic pieces of porous PDMS scaffolds were UV irradiated, individually placed in 25 mL Falcon tubes, and received the following treatment: (i) thoroughly wash using 0.5 mL PBS and 5 min centrifugation until porous PDMS float stops; (ii) treatment with 2 M acetic acid during 20 min and then a rapid neutralization and PBS wash; (iii) treatment with hMSC trophic factors medium during 24 hours or DMEM-LG as control; and (iv) seed scaffolds with 150.000 hMSCs in 0.5 mL chondrogenic or control medium during three weeks

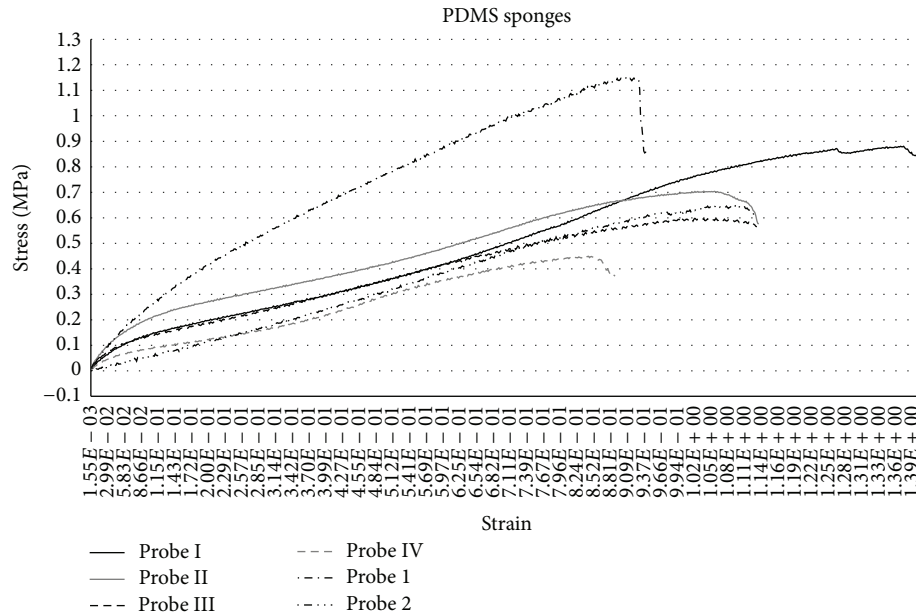


FIGURE 6: Comparative mechanical performance of the PDMS sponges obtained.

at 37°C in 5% CO₂ as early indicated [34–37]. When PDMS sponges were functionalized with APTS it was used at a concentration of 0.025% in ethanol. The chondrogenic medium was DMEM-LG with ITS (6.25 µg/mL insulin, 6.25 µg/mL transferrin, and 6.25 µg/mL selenous acid) (Collaborative Research), 1mM pyruvate (Gibco), 37.5 µg/mL ascorbate (WACO), 0.1 µM dexamethasone (Decadran, Merck), and 0.06 ng TGF-β (R&D System).

Then, samples were processed to analyze by using an immune fluorescence technique, as described previously [37, 38], with some modifications. Briefly, cubic scaffolds were individually placed in M24 tissue dishes, cut in slices, rinsed with ice-cold PBS, fixed in 3.7% formaldehyde in PBS during 30 min at RT, and washed in PBS. Cells were visualized by incubation with 0.5% Triton in CSK buffer containing 10 mM pipes, pH 6.8, 3 mM MgCl₂, 100 mM NaCl, 1 mM EGTA, 0.3 M sucrose, and 1 mM PMSF for 30 min on ice. After the treatment, samples were cleaned and fixed with 3.7% formaldehyde and equilibrated in PBS. For collagen type II immune detection, scaffolds preparations were blocked of unspecific antibodies binding by incubation during an hour with 3% BSA-0.1% Triton X-100 in PBS (PBSA) at RT or overnight at 4°C. As primary antibodies anti-collagen type II at 1:200 were used, secondary antibodies were Alexa594-conjugated from Molecular Probes, Eugene, OR, at 1/500 dilution. Nuclei were stained with DAPI (CALBIOCHEM). Immune stainings of the cell preparations were determined with an inverted IX81 Olympus with a DP72 digital camera.

3. Results and Discussion

Results from Figure 4, showing implant geometries with scaffolding porous structures, have helped to validate the design and rapid manufacturing processes, as relevant tasks

towards a systematic procedure for the development of free-form, porous, and biomimetic scaffolds (as well as other (micro) implants) for tissue engineering and repair. The term “biomimetic” in this case makes not only reference to the appearance, but also reference to the mechanical properties, which are discussed below. The lower image of Figure 5, after probe collapse during tensile testing, helps to show the three-dimensional interconnected microporous network and the efficiency of the leaching process, as all the sugar particles have disappeared. Figure 6 includes the comparative mechanical performance of the PDMS sponges obtained and the most interesting values (tensile strength and Young modulus), together with density, are summarized in Table 1, besides interesting data about different typical soft tissues for additional reflections.

According to initial expectations, an increase of porogen loading (Probes I–IV) leads to lower scaffold densities and to lower values of tensile strength and Young modulus. The PDMS-water emulsion (Probe 1) leads to a density and Young modulus similar to those of Probe IV, while its tensile strength is quite higher. We explain such difference of tensile strength due to the smaller pore sizes and more homogeneous pore distribution of Probe 1, which helps to minimize the effects of stress concentration at the connections between pores.

However, pore sizes obtained by phase separation, after polymerization of the PDMS-water emulsion, are around 30 to 60 microns in diameter, smaller than the 100–200 microns in diameter pores obtained by particle leaching. The smaller pore sizes, in our case, prevent the formation of a three-dimensional network of interconnected pores, which is necessary for adequate scaffolds. Such interconnected pore network is obtained in Probes I–IV, with remarkable results in Probe IV, which we find the most apt for final *in vitro* validation via cell culture. Probe 2, obtained by a combined

TABLE 1: Results' summary from the mechanical characterization tests of the PDMS sponges obtained and comparative data from other porous polymers and natural soft tissues.

Porous PDMS and tissues	Tensile strength (MPa)	Young modulus (MPa)	Density (g/cm^3)
Probe I	0.88	2.77	0.96
Probe II	0.71	3.70	0.82
Probe III	0.59	2.47	0.79
Probe IV	0.45	1.47	0.65
Probe 1	1.15	1.64	0.64
Probe 2	0.65	0.72	0.75
PolyHIPE [39]	0.17	0.88	0.15
Skin [40]	10	40	1.09
Pericardium [41]	25.8	156	1.8
Tendon [40]	80	1000	1.2
Carotid artery [40]	0.8	0.97	1.3
Aorta artery [40]	0.9	6.5	1.39
Esophagus [42]	0.5	6	1.18
Parenchyma [43]	0.6	5	0.87
Cartilage [44]	10–30	0.45–0.9	1.05–1.2

approach using a PDMS-sugar-water mixture, can be used for multiscale approaches, as different pore sizes are obtained, although some pores reaching diameters of 300–400 microns lead to a much lower Young modulus.

In any case, it is interesting to highlight the possibility of adjusting scaffold density, stiffness, and strength, almost ad hoc, by incorporating different quantities and mixtures of water, sugar, and water-sugar, to the PDMS. Previous research has verified the effect of scaffold stiffness on hMSCs differentiation and final fate, showing that softer scaffolds lead to softer tissues and that stiffer scaffolds lead to harder tissues. In our study, the scaffolds developed show a wide range of Young moduli, which can adapt to the requirements of several soft tissues, from cartilage to esophagus, parenchyma, and arteries, as shown in Table 1.

Regarding *in vitro* assessment via cell culture, results after three weeks (summarized in Figure 7) show that cells are well attached to the scaffold, even having penetrated into the porous structure, forming a three-dimensional network within the interconnected pores. For the cell culture process we have used Probe IV, as usually scaffold manufacturing processes for soft tissue repair pursue low densities and high porosities. The figure shows details of the cells attached to the scaffold surrounding and filling different pores. It is also relevant to note that, during cell culture, cells developed collagen, helping to show the potential for tissue repair of the proposed approach.

Scaffold's porosity, through capillary action, helps the growth factors to fill the three-dimensional interconnected porous structure, which proves to be positive for promoting cells to reach the inner cavities of the scaffold. The

incorporation of trophic factors produced by hMSCs isolated from bone marrow is essential for cell adhesion and for final success of the PDMS-3D niche. In addition, the stiffness of Probe IV, used as scaffolding material, is very similar to cartilage stiffness and cartilage stands out for its large amount of extracellular matrix, mainly composed of collagen fibers.

In fact, the PDMS-3D niche, seeded with hMSCs and incubated in a chondrogenic medium during three weeks, realized chondrogenesis process expressing collagen type II validating a new method to obtain an excellent scaffold, at least, for cartilage and endochondral bone formation/repair strategies. Therefore, we believe that our scaffold's stiffness may have had a relevant impact on hMSCs growth and collagen generation, thus being potentially adequate for the promotion of chondrogenesis and for cartilage repair.

It is important to highlight that MSCs are adherent cells and rapidly die in suspension. Hence, mimicking the extracellular matrix is absolutely needed for prosthesis development and tissue repair biomaterials. However, cells do not usually get into a biomaterial unless using a pair antigen-antibody as hormone-receptor recognition system. To this end specific laser treatment is normally used to get reaction inside a biomaterial. Our novel approach shows a biomaterial where the communication factors promote MSC adhesion, even inside the pores. In addition, upon incubation in a regular chondrogenic medium, cells expressed collagen type II and most cells (whose nuclei are shown as bright red points in Figure 7) remained buried in collagen (shown in red in the images of Figure 7).

The design and manufacture process presented combines rapid prototyping, for controlling scaffold's outer geometry, with phase separation processes, for promoting porous biomimetic structures, towards final scaffolds and implants for tissue repair with desired physical properties and pre-defined geometries. Such process constitutes an alternative or a complementary approach to other recent solutions for the development of tissue engineering scaffolds, based exclusively on additive processes, which stand out due to the possibility of controlling final geometries from the design stage, although the CAD-based geometries are usually simple (typical wood-pile structures), soft, and not especially biomimetic. The detailed procedure can also complement or be combined with highly interesting noninvasive 3D reconstructions based on medical imaging [45]. Future comparisons between niches directly obtained by additive manufacture from medical images and those obtained by casting with porogens in rapid molds will also provide additional information towards future applications.

Due to the results obtained, we recommend these scaffolds for cartilage and endochondral bone formation/repair strategies. We foresee relevant applications in several fields, such as biomedical and tissue engineering, that is, for the development of different (micro)implants and scaffolding structures, mainly for soft tissue replacement and repair. Personalized approaches are also possible, thanks to the combination of medical imaging and medical software resources with the capabilities of computer-aided design and additive rapid prototyping, what constitutes a relevant advantage in areas including aesthetic and reconstructive surgeries.

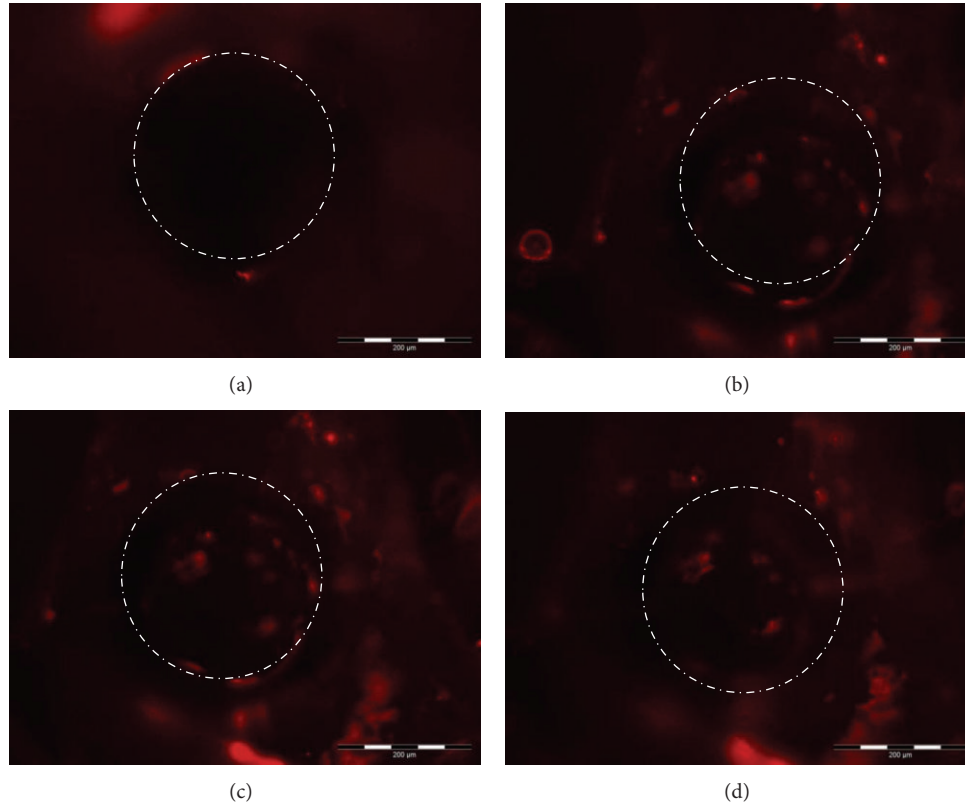


FIGURE 7: Results from hMSCs culture upon the PDMS sponges incorporating growth factors. Images taken at different depths to show cell penetration into pore (marked with dotted line). After a three-week culture process, cells (appreciated as prominent points in red) are well attached to the scaffold, have penetrated into the porous structure, and developed collagen (shown in red), helping to show the potential for tissue repair and cartilage generation of the proposed approach. Scale bar: 200 μm .

4. Conclusions

In this study we have presented a very promising approach for the rapid development of porous polydimethylsiloxane (PDMS) scaffold prototypes, with outer geometry defined from the design stage, according to the form of conventional implants or adapted to patients' biostructures. The manufacture method is based on phase separation processes using parts obtained by casting within additive rapid prototyped molds. We have included a comparative study of PDMS sponges obtained by different simple processes involving PDMS-sugar-water mixtures. By changing the proportions of these agents, main mechanical properties of the final scaffold can be tuned and adapted to the typical density and stiffness of several soft tissues, as has been previously detailed.

Different porous annuloplasty rings have been also obtained, by means of example, in order to highlight the potential of the manufacture process towards free-form porous implants and scaffolds for tissue replacement and repair. Final *in vitro* assessment was carried out using hMSCs (bone marrow-derived human mesenchymal stem cells), cultured onto porous PDMS scaffolds functionalized with APTS and equilibrated with trophic factors medium produced by the cells. Results show that porous PDMS scaffold prototypes are excellent 3D platforms for hMSCs adhesion. Furthermore, this PDMS-3D niche, seeded with

hMSCs and chondrogenic incubation medium during three weeks, showed a successful chondrogenesis determined by collagen type II expression. Thus, results show a versatile method to produce a 3D niche to further study questions about cartilage and endochondral bone formation or skeleton tissues clinical approaches.

Conflict of Interests

The authors declare that there is no conflict of interests regarding the publication of this paper.

Acknowledgments

This work was carried out with the support of the technologies available at the UPM Product Development Laboratory and counting with the help of Mr. Pedro Ortego for rapid prototyping tasks. The authors acknowledge reviewers for their positive opinions and proposals for improvement, which have helped to enhance paper quality and final result.

References

- [1] R. Langer and J. P. Vacanti, "Tissue engineering," *Science*, vol. 260, no. 5110, pp. 920–926, 1993.

- [2] W. E. Thomas, D. E. Discher, and V. Prasad Shastri, "Mechanical regulation of cells by materials and tissues," *MRS Bulletin*, vol. 35, no. 8, pp. 578–583, 2010.
- [3] W. L. K. Chen, M. Likhitanichkul, A. Ho, and C. A. Simmons, "Integration of statistical modeling and high-content microscopy to systematically investigate cell-substrate interactions," *Biomaterials*, vol. 31, no. 9, pp. 2489–2497, 2010.
- [4] A. Buxboim and D. E. Discher, "Stem cells feel the difference," *Nature Methods*, vol. 7, no. 9, pp. 695–697, 2010.
- [5] A. Díaz Lantada, *Handbook of Advanced Design and Manufacturing Technologies for Biodevices*, Springer, 2013.
- [6] P. J. S. Bartolo, H. Almeida, and T. Laoui, "Rapid prototyping and manufacturing for tissue engineering scaffolds," *International Journal of Computer Applications in Technology*, vol. 36, no. 1, pp. 1–9, 2009.
- [7] J. Y. Tan, C. K. Chua, and K. F. Leong, "Indirect fabrication of gelatin scaffolds using rapid prototyping technology," *Virtual and Physical Prototyping*, vol. 5, no. 1, pp. 45–53, 2010.
- [8] A. K. Ekaputra, Y. Zhou, S. M. Cool, and D. W. Huttmacher, "Composite electrospun scaffolds for engineering tubular bone grafts," *Tissue Engineering A*, vol. 15, no. 12, pp. 3779–3788, 2009.
- [9] S. Lohfeld, M. A. Tyndyk, S. Cahill, N. Flaherty, V. Barron, and P. E. McHugh, "A method to fabricate small features on scaffolds for tissue engineering via selective laser sintering," *Journal of Biomedical Science and Engineering*, vol. 3, p. 138, 2010.
- [10] R. Tzezana, E. Zussman, and S. Levenberg, "A layered ultra-porous scaffold for tissue engineering, created via a hydrospinning method," *Tissue Engineering C*, vol. 14, no. 4, pp. 281–288, 2008.
- [11] A. Díaz-Lantada, A. Mosquera, J. L. Endrino, and P. Lafont, "Design and rapid prototyping of DLC coated fractal surfaces for tissue engineering applications," *Journal of Physics*, vol. 252, no. 1, Article ID 012003, 2010.
- [12] J. Stampfl, H. Fouad, S. Seidler et al., "Fabrication and moulding of cellular materials by rapid prototyping," *International Journal of Materials and Product Technology*, vol. 21, no. 4, pp. 285–296, 2004.
- [13] R. Infuehr, N. Pucher, C. Heller et al., "Functional polymers by two-photon 3D lithography," *Applied Surface Science*, vol. 254, no. 4, pp. 836–840, 2007.
- [14] P. S. Maher, R. P. Keatch, K. Donnelly, and J. Z. Paxton, "Formed 3D bio-scaffolds via rapid prototyping technology," in *Proceedings of the 4th European Conference of the International Federation for Medical and Biological Engineering (ECIFMBE '08)*, vol. 22, pp. 2200–2204, November 2008.
- [15] G. E. Ryan, A. S. Pandit, and D. P. Apatsidis, "Porous titanium scaffolds fabricated using a rapid prototyping and powder metallurgy technique," *Biomaterials*, vol. 29, no. 27, pp. 3625–3635, 2008.
- [16] P. H. Warnke, T. Douglas, P. Wollny et al., "Rapid prototyping: porous titanium alloy scaffolds produced by selective laser melting for bone tissue engineering," *Tissue Engineering C*, vol. 15, no. 2, pp. 115–124, 2009.
- [17] J. Stampfl, S. Baudis, C. Heller et al., "Photopolymers with tunable mechanical properties processed by laser-based high-resolution stereolithography," *Journal of Micromechanics and Microengineering*, vol. 18, no. 12, Article ID 125014, 2008.
- [18] I. Manjubala, A. Woesz, C. Pilz et al., "Biomimetic mineral-organic composite scaffolds with controlled internal architecture," *Journal of Materials Science*, vol. 16, no. 12, pp. 1111–1119, 2005.
- [19] M. Schuster, C. Turecek, B. Kaiser, J. Stampfl, R. Liska, and F. Varga, "Evaluation of biocompatible photopolymers—I: photoreactivity and mechanical properties of reactive diluents," *Journal of Macromolecular Science A*, vol. 44, no. 5, pp. 547–557, 2007.
- [20] M. Schuster, C. Turecek, A. Mateos, J. Stampfl, R. Liska, and F. Varga, "Evaluation of biocompatible photopolymers—II: further reactive diluents," *Monatshefte fur Chemie*, vol. 138, no. 4, pp. 261–268, 2007.
- [21] F. Jung, C. Wischke, and A. Lendlein, "Degradable, multifunctional cardiovascular implants: challenges and hurdles," *MRS Bulletin*, vol. 35, no. 8, pp. 607–613, 2010.
- [22] J. Y. Tan, C. K. Chua, and K. F. Leong, "Fabrication of channeled scaffolds with ordered array of micro-pores through micro-sphere leaching and indirect rapid prototyping technique," *Biomedical Microdevices*, vol. 15, p. 83, 2013.
- [23] C. K. F. Chan, C.-C. Chen, C. A. Luppen et al., "Endochondral ossification is required for haematopoietic stem-cell niche formation," *Nature*, vol. 457, no. 7228, pp. 490–494, 2009.
- [24] T. P. Richardson, M. C. Peters, A. B. Ennett, and D. J. Mooney, "Polymeric system for dual growth factor delivery," *Nature Biotechnology*, vol. 19, no. 11, pp. 1029–1034, 2001.
- [25] A. Perets, Y. Baruch, F. Weisbuch, G. Shoshany, G. Neufeld, and S. Cohen, "Enhancing the vascularization of three-dimensional porous alginate scaffolds by incorporating controlled release basic fibroblast growth factor microspheres," *Journal of Biomedical Materials Research A*, vol. 65, no. 4, pp. 489–497, 2003.
- [26] M. W. Laschke, M. Rücker, G. Jensen et al., "Incorporation of growth factor containing Matrigel promotes vascularization of porous PLGA scaffolds," *Journal of Biomedical Materials Research A*, vol. 85, no. 2, pp. 397–407, 2008.
- [27] J. Chen, R. Zjang, and W. Wang, *Fabricating Microporous PDMS Using Water-in-PDMS Emulsion*, RSC Publishing Blogs Home. Chips and Tips, 2012.
- [28] S. Peng, P.G. Hartley, T.C. Hughes, and Q. Guo, "Controlling morphology and porosity of porous siloxane membranes through water content of precursor microemulsion," *Soft Maters*, vol. 8, no. 40, p. 10493, 2012.
- [29] P. K. Yuen, H. Su, V. N. Goral, and K. A. Fink, "Three-dimensional interconnected microporous poly(dimethylsiloxane) microfluidic devices," *Lab on a Chip*, vol. 11, no. 8, pp. 1541–1544, 2011.
- [30] Q. Tan, S. Li, J. Ren, and C. Chen, "Fabrication of porous scaffolds with a controllable microstructure and mechanical properties by porogen fusion technique," *International Journal of Molecular Sciences*, vol. 12, no. 2, pp. 890–904, 2011.
- [31] F. Ciaramella, V. Jousseau, S. Maitrejean, B. Rémiat, M. Verdier, and G. Passemard, "Mechanical properties of porous MSQ films: impact of the porogen loading and matrix crosslinking," in *Proceedings of the Materials Research Society Spring Meeting*, pp. 17–22, April 2005.
- [32] W. Y. Yeong, N. Sudarmadji, H. Y. Yu et al., "Porous polycaprolactone scaffold for cardiac tissue engineering fabricated by selective laser sintering," *Acta Biomaterialia*, vol. 6, no. 6, pp. 2028–2034, 2010.
- [33] A. Díaz Lantada, R. D. Valle-Fernández, P. L. Morgado et al., "Development of personalized annuloplasty rings: combination of CT images and CAD-CAM tools," *Annals of Biomedical Engineering*, vol. 38, no. 2, pp. 280–290, 2010.
- [34] M. F. Pittenger, A. M. Mackay, S. C. Beck et al., "Multilineage potential of adult human mesenchymal stem cells," *Science*, vol. 284, no. 5411, pp. 143–147, 1999.

- [35] D. P. Lennon, S. E. Haynesworth, S. P. Bruder, N. Jaiswal, and A. I. Caplan, "Human and animal mesenchymal progenitor cells from bone marrow: identification of serum for optimal selection and proliferation," *In Vitro Cellular and Developmental Biology*, vol. 32, no. 10, pp. 602–611, 1996.
- [36] S. Ogueta, J. Muñoz, E. Obregon, E. Delgado-Baeza, and J. P. García-Ruiz, "Prolactin is a component of the human synovial liquid and modulates the growth and chondrogenic differentiation of bone marrow-derived mesenchymal stem cells," *Molecular and Cellular Endocrinology*, vol. 190, no. 1-2, pp. 51–63, 2002.
- [37] M. Romero-Prado, C. Blázquez, C. Rodríguez-Navas et al., "Functional characterization of human mesenchymal stem cells that maintain osteochondral fates," *Journal of Cellular Biochemistry*, vol. 98, no. 6, pp. 1457–1470, 2006.
- [38] A. Javed, B. Guo, S. Hiebert et al., "Groucho/TLE/R-esp proteins associate with the nuclear matrix and repress RUNX (CBF α /AML/PEBP2 α) dependent activation of tissue-specific gene transcription," *Journal of Cell Science*, vol. 113, no. 12, pp. 2221–2231, 2000.
- [39] J. Normatov and M. S. Silverstein, "Porous interpenetrating network hybrids synthesized within high internal phase emulsions," *Polymer*, vol. 48, no. 22, pp. 6648–6655, 2007.
- [40] J. Y. Wong and J.D. Bronzino, *Biomaterials*, CRC-Press, 2007.
- [41] F. J. Rojo, J.M. Atienza, E. Jorge-Herrero, J.M. García-Páez, and G.V. Guinea, "Resistencia a tracción de membranas de pericardio para válvulas cardíacas biológicas," *Anales de Mecánica de la Fractura*, vol. 26, no. 1, 2009.
- [42] R. K. Goyal, P. Biancani, A. Phillips, and H.M. Spiro, *Mechanical Properties of the Esophageal Wall*, Yale University, 1971.
- [43] I. Levental, P. C. Georges, and P. A. Janmey, "Soft biological materials and their impact on cell function," *Soft Matter*, vol. 3, no. 3, pp. 299–306, 2007.
- [44] J. M. Mansour, "Biomechanics of cartilage," in *Kinesiology: The Mechanics and Pathomechanics of Human Movement*, C. A. Oatis, Ed., Lippincott Williams and Wilkins, 2003.
- [45] A. Tsouknidas, A. Lontos, S. Savvakis, and N. Michailidis, "Nonintrusive 3D reconstruction of human bone models to simulate the biomechanical response," *3D Research Express*, vol. 3, no. 2, p. 5, 2012.

Research Article

Antibacterial Characteristics of Lotus-Type Porous Copper

Jin-Soo Lee,¹ Yun-Soo Lee,^{1,2} Mok-Soon Kim,¹ Soong-Keun Hyun,¹
Chang-Ho Kang,³ Jae-Seong So,³ and Eui-Han Yoon⁴

¹ Department of Metallurgical Engineering, Inha University, Incheon 402-751, Republic of Korea

² Light Metal Division, Korea Institute of Materials Science, Changwon 642-831, Republic of Korea

³ Department of Biological Engineering, Inha University, Incheon 402-751, Republic of Korea

⁴ Institute of Research & Technology, Daechang Co., Ltd., Siheung 429-794, Republic of Korea

Correspondence should be addressed to Soong-Keun Hyun; skhyun@inha.ac.kr

Received 11 October 2013; Accepted 26 November 2013

Academic Editor: Nikolaos Michailidis

Copyright © 2013 Jin-Soo Lee et al. This is an open access article distributed under the Creative Commons Attribution License, which permits unrestricted use, distribution, and reproduction in any medium, provided the original work is properly cited.

Lotus-type porous copper with long cylindrical pores aligned parallel to the solidification direction was studied for use as an antibacterial material. The antibacterial performance of lotus-type porous copper samples with different specific surface areas against *Escherichia coli* was investigated. The results confirmed that the antibacterial effect gradually increased with specific surface area. The correlation between the pore structure of lotus-type porous metals and their antibacterial effect was also analyzed in detail. Our research proposes a new application of these metals in the water purifying system.

1. Introduction

In addition to offering convenience and many lifestyle options, industrial development has caused serious environmental contamination, especially water pollution, which increases the growth of various bacteria, viruses, and protozoa that cause water-borne diseases. Removal of disease-causing organisms from drinking water is, therefore, extremely important for human health. There are several conventional chemical disinfectants such as chlorine and its derivatives and ozone [1]. However, many of these agents are carcinogens with potential harmful side effects [2].

In this regard, several researchers have recently investigated the use of inorganic antibacterial materials such as silver and copper to inhibit microbial growth. In particular, research studies on porous antibacterial materials are well under way because the antibacterial effect is proportionate to the increase in surface area [3–5]. Shen et al. [3] evaluated the antibacterial characteristics of porous ceramic composites that were decorated with ultrafine silver (II) oxide particles and fabricated by chemical oxidation. Chen et al. [4] examined Cu-TiO₂ nanocomposites that could be created

by photocatalytic reduction and studied their antibacterial performance in the absence of light.

Lotus-type (or Gasar) porous metals [6, 7], which have long cylindrical pores aligned parallel to the solidification direction, have many advantages over other materials for antibacterial applications. For example, the specific surface area of these metals can be easily controlled by manipulating the porosity and pore diameter [6, 8–10]. These metals also exhibit high fluid permeability because of their low pressure drop [6, 11]. In addition, they are easy to manufacture and are suited for mass production because their fabrication is based on the casting process [6, 8, 10]. However, the antibacterial performance of lotus-type porous metals has not been evaluated.

Here, we show the antibacterial performance of lotus-type porous metals with various specific surface areas that were controlled by hydrogen gas pressure and solidification velocity [6, 8, 10]. Lotus-type porous copper was selected for the antibacterial test because copper has much higher antimicrobial activity than other metals such as silver, aluminum, silicon, and tin [12]. The correlation between pore structure and antibacterial effect will also be discussed in detail.

2. Materials and Methods

2.1. Preparation of Lotus-Type Porous Copper. Lotus-type porous copper ingots with various porosities and pore diameters were fabricated by mold casting [8] and continuous casting [10] according to a previously described procedure. In brief, the fabrication of lotus-type porous copper is a continuous process comprising a series of hydrogen gas pressurization, induction melting, and directional solidification stages. Each ingot was cut into rectangular parallelepipeds ($25 \times 25 \times 2.5 \text{ mm}^3$) by using a spark-erosion wire-cutting machine (A325; Sodick Co., Japan). Nonporous and lotus-type porous copper samples were polished with a series of emery papers, washed in ultrasonic cleaner, and finally dried in hot air. The porosity of each sample was obtained from the following equation:

$$\text{Porosity (\%)} = \left(1 - \frac{\rho}{\rho_0}\right) \times 100, \quad (1)$$

where ρ and ρ_0 are the apparent density of the porous copper and the density of nonporous copper, respectively. The pore diameter was measured in the cross-section perpendicular to the solidification direction by using an image analyzer (Image-Pro Plus; Media Cybernetics Co., USA). The specific surface area was also calculated on the basis of the assumption that the pores were perfectly cylindrical.

2.2. Antibacterial Activity. *Escherichia coli* (*E. coli*; KCTC 2223) used in this study was a strain from the Korean Collection for Type Culture (KCTC, Daejeon, Korea). The nonporous and lotus-type porous copper samples were immersed in 100 mL of phosphate-buffered saline (PBS) solution containing approximately 10^2 cfu/mL *E. coli*, for specific time intervals of 15, 30, 45, 60, 90, and 120 min at room temperature. To obtain the bacterial concentration, the 3 M Petrifilm *E. coli* count plate method was used: 1 mL of the bacterial suspension was dispensed on Petrifilms by using a micropipette; the films were then placed in an incubator at $37 \pm 1^\circ\text{C}$ for 24 h. The antibacterial rate was determined using the following formula [13]:

$$\text{Antibacterial rate (\%)} = \frac{N_1 - N_2}{N_1} \times 100, \quad (2)$$

where N_1 and N_2 are the bacterial count, when using the control material (304 stainless steel) and the nonporous or lotus-type porous copper, respectively. The concentration of copper ions in distilled water was also verified with an inductively coupled plasma mass spectrometer (ICP-MS; ELAN 6100, Perkin-Elmer SCIEX, Canada).

3. Results and Discussion

Figure 1 shows the cross-sectional views perpendicular to the solidification direction of the lotus-type porous copper samples. In addition, the measured porosity, average pore diameter, and specific surface area of the samples are summarized in Table 1. The specific surface area of the lotus-type porous copper samples was much higher than that of

TABLE 1: Porosity, average pore diameter, and specific surface area of nonporous and lotus-type porous copper samples.

	Nonporous copper	Lotus-type porous copper		
		A	B	C
Porosity (%)	—	72.2	71.4	47.8
Average pore diameter (μm)	—	1128.3	670.6	222.1
Specific surface area (cm^2/g)	1.1	6.5	9.0	14.1

nonporous copper, and it depended on the average pore diameter and pore distribution. In particular, the specific surface area of sample C was almost 14 times the value for nonporous copper.

Figure 2(a) shows the antibacterial effect of nonporous and lotus-type porous copper with various specific surface areas as a function of the immersion time. The term “reference” refers to data obtained without involving copper samples. The antibacterial performance of copper gradually increased with increasing specific surface area. Figure 2(b) shows the antibacterial rate calculated using (2). It can be seen that after 30 min of coculturing with *E. coli*, the antibacterial rates of sample C reached $>99.999\%$, showing strong antibacterial functions.

Figure 3 shows the number of dissolved copper ions in distilled water after immersing samples of nonporous and lotus-type porous copper (sample C) for various time intervals. These values were verified by ICP-MS analysis. The number of copper ions from the porous copper sample was much higher than that from the nonporous copper sample; the numbers increased with increasing immersion time.

There are several reasons why lotus-type porous copper showed better antibacterial performance when compared to nonporous or conventional porous copper. First, specific surface area affects antibacterial performance. The antibacterial mechanism of metallic antibacterial materials can be classified by the action of metallic ions and active oxygen generated on the surface [14]. This characterization was expected in our experiment since more *E. coli* were exposed to copper as the samples' specific surface area increased. The morphology of lotus-type porous metals comprised cylindrical pores aligned parallel to the solidification direction. Thus, this configuration yielded large surface areas when the ingots were cut perpendicular to the solidification direction because almost all the pores were open.

Another accelerating factor for the antibacterial performance may be crevice corrosion. Crevice corrosion is a rather aggressive form of corrosion that arises in the narrow gaps between a metal and another material, and it accelerates the elution of metal ions. In general, the corrosion behavior of porous metals is a very serious disadvantage when compared to bulk metals, particularly in case of crevice corrosion. Corrosion is also influenced by the morphology of pores and the specific surface area [15]. However, corrosion may offer a rather significant benefit from a different perspective, especially regarding the antibacterial effect. Although this experiment was conducted in the PBS solution, which has low

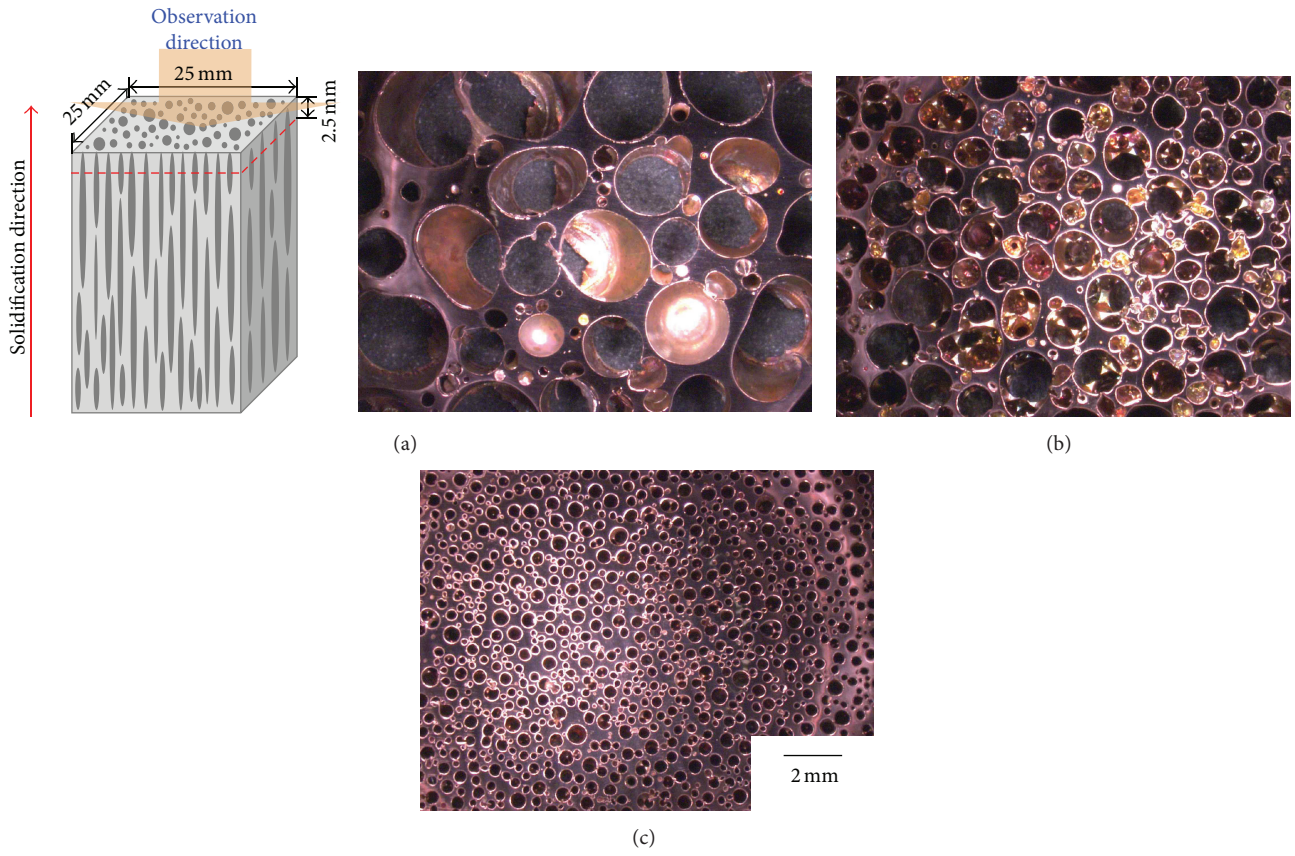


FIGURE 1: Cross-sectional views perpendicular to the solidification direction of lotus-type porous copper with various specific surface areas: (a) 6.5 cm²/g; (b) 9.0 cm²/g; (c) 14.1 cm²/g.

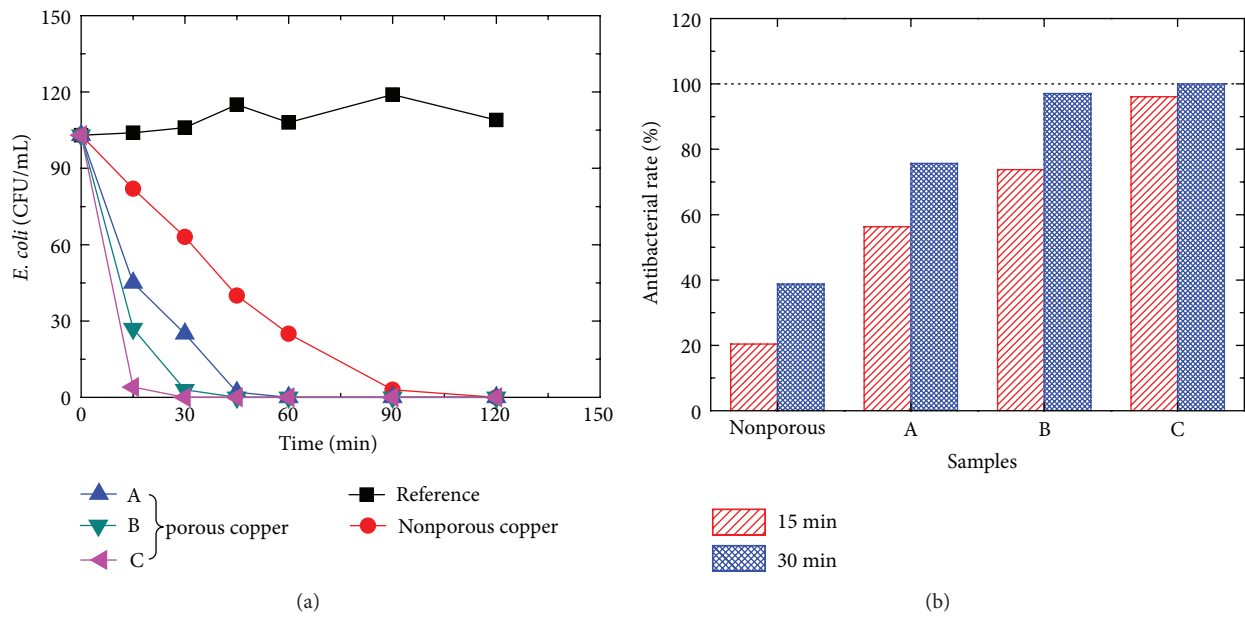


FIGURE 2: Time-course study of the (a) population and (b) antibacterial rates of nonporous and lotus-type porous copper against *E. coli*. The term “reference” in (a) refers to data obtained without involving copper samples.

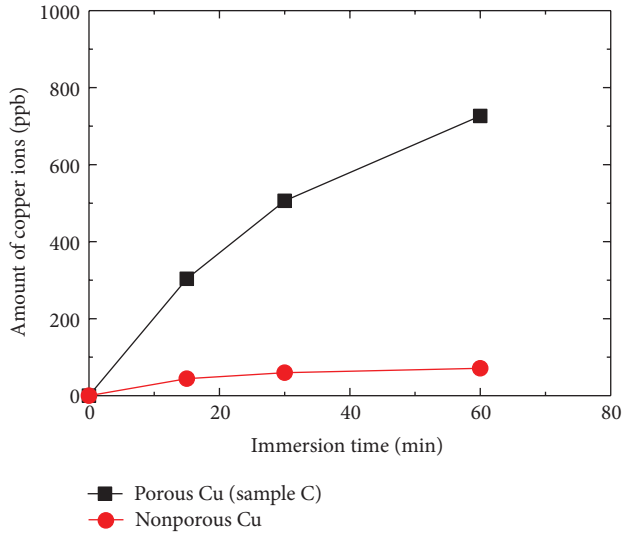


FIGURE 3: Number of dissolved copper ions in distilled water after immersing the nonporous and lotus-type porous copper samples for various time intervals.

chloride ion concentration and buffering capability, lotus-type porous metals have many narrow pores as noted above, and the crevice corrosion effect cannot be overlooked.

4. Conclusions

In this study, the antibacterial performance of lotus-type porous copper was evaluated and the correlation between pore structure and the antibacterial effect was analyzed. The antibacterial performance of lotus-type porous copper gradually increased with increasing specific surface area. This was because the specific surface area and crevice corrosion behavior were influenced by the pore morphology of lotus-type porous metals. Based on our research, we believe lotus-type porous metals have potential applications in the healthcare industry, especially water purifying system.

Acknowledgments

This research was supported by Daechang Grant, the Regional Innovation Center for Environmental Technology of Thermal Plasma (ETTP) at Inha University designated by MOCIE, and the Basic Science Research Program through the National Research Foundation of Korea (NRF) funded by the Ministry of Education, Science and Technology (2012007739).

References

- [1] R. L. Droste, *Theory and Practice of Water and Waste Water Treatment*, John Wiley & Sons, New York, NY, USA, 1997.
- [2] S. D. Richardson, M. J. Plewa, E. D. Wagner, R. Schoeny, and D. M. DeMarini, "Occurrence, genotoxicity, and carcinogenicity of regulated and emerging disinfection by-products in drinking water: a review and roadmap for research," *Mutation Research*, vol. 636, no. 1–3, pp. 178–242, 2007.

- [3] W. Shen, L. Feng, H. Feng, Z. Kong, and M. Guo, "Ultrafine silver(II) oxide particles decorated porous ceramic composites for water treatment," *Chemical Engineering Journal*, vol. 175, no. 1, pp. 592–599, 2011.
- [4] S. Chen, Y. Guo, S. Chen, Z. Ge, H. Yang, and J. Tang, "Fabrication of Cu/TiO₂ nanocomposite: toward and enhanced antibacterial performance in the absence of light," *Materials Letters*, vol. 83, pp. 154–157, 2012.
- [5] H. Jing, Z. Yu, and L. Li, "Antibacterial properties and corrosion resistance of Cu and Ag/Cu porous materials," *Journal of Biomedical Materials Research A*, vol. 87, no. 1, pp. 33–37, 2008.
- [6] H. Nakajima, "Fabrication, properties and application of porous metals with directional pores," *Progress in Materials Science*, vol. 52, no. 7, pp. 1091–1173, 2007.
- [7] V. Shapovalov and L. Boyko, "Gasar—a new class of porous materials," *Advanced Engineering Materials*, vol. 6, no. 6, pp. 407–410, 2004.
- [8] S. K. Hyun and H. Nakajima, "Effect of solidification velocity on pore morphology of lotus-type porous copper fabricated by unidirectional solidification," *Materials Letters*, vol. 57, no. 21, pp. 3149–3154, 2003.
- [9] M. Kashihara, S. K. Hyun, H. Yonetani, T. Kobi, and H. Nakajima, "Fabrication of lotus-type porous carbon steel by unidirectional solidification in nitrogen atmosphere," *Scripta Materialia*, vol. 54, no. 4, pp. 509–512, 2006.
- [10] J. S. Park, S. K. Hyun, S. Suzuki, and H. Nakajima, "Effect of transference velocity and hydrogen pressure on porosity and pore morphology of lotus-type porous copper fabricated by a continuous casting technique," *Acta Materialia*, vol. 55, no. 16, pp. 5646–5654, 2007.
- [11] H. Chiba, T. Ogushi, H. Nakajima, and T. Ikeda, "Heat transfer capacity of lotus-type porous copper heat sink," *JSME International Journal B*, vol. 47, no. 3, pp. 516–521, 2004.
- [12] A. J. Varkey, "Antibacterial properties of some metals and alloys in combating coliforms in contaminated water," *Scientific Research and Essays*, vol. 5, no. 24, pp. 3834–3839, 2010.
- [13] K. Liao, K. Ou, H. Cheng, C. Lin, and P. Peng, "Effect of silver on antibacterial properties of stainless steel," *Applied Surface Science*, vol. 256, no. 11, pp. 3642–3646, 2010.
- [14] T. Yokota, M. Tochiwara, and M. Ohta, "Silver dispersed stainless steel with antibacterial property," *Kawasaki Steel Technical Report*, no. 46, pp. 37–41, 2002.
- [15] K. H. W. Seah, R. Thampuran, and S. H. Teoh, "The influence of pore morphology on corrosion," *Corrosion Science*, vol. 40, no. 4–5, pp. 547–556, 1998.